

## **Copyright Warning & Restrictions**

The copyright law of the United States (Title 17, United States Code) governs the making of photocopies or other reproductions of copyrighted material.

Under certain conditions specified in the law, libraries and archives are authorized to furnish a photocopy or other reproduction. One of these specified conditions is that the photocopy or reproduction is not to be “used for any purpose other than private study, scholarship, or research.” If a user makes a request for, or later uses, a photocopy or reproduction for purposes in excess of “fair use” that user may be liable for copyright infringement,

This institution reserves the right to refuse to accept a copying order if, in its judgment, fulfillment of the order would involve violation of copyright law.

**Please Note: The author retains the copyright while the New Jersey Institute of Technology reserves the right to distribute this thesis or dissertation**

Printing note: If you do not wish to print this page, then select “Pages from: first page # to: last page #” on the print dialog screen

The Van Houten library has removed some of the personal information and all signatures from the approval page and biographical sketches of theses and dissertations in order to protect the identity of NJIT graduates and faculty.

## ABSTRACT

### UNDERSTANDING THE INTERFACIAL PROCESSES OF REACTIVE NANOBUBBLES TOWARD AGRICULTURAL APPLICATIONS

by  
**Xiaonan Shi**

There is a growing interest in nanobubble (NB) technology because of its diverse applications (e.g., detergent-free cleaning, water aeration, ultra-sound imaging and intracellular drug delivery, and mineral processing). NBs have a higher efficiency of mass transfer compared to bulk scale bubbles due to the high specific surface areas. The high specific surface also facilitates physical adsorption and chemical reactions in the gas liquid interface. Furthermore, the collapse of NBs creates shock waves and the formation of hydroxyl radicals ( $\bullet\text{OH}$ ).

However, it remains elusive why or how NBs are stabilized in water and particularly, the states of internal pressures of NBs are difficult to measure. This thesis employs the injection of high-pressure gases through a hydrophobized ceramic membrane to produce different gaseous NBs in water. The results indicate that increasing the injection gas pressure (60–80 psi) and solution temperatures (6–40 °C) both reduce bubble sizes, which are validated by two independent models developed from the Young-Laplace equation and contact mechanics. Both models yield consistent prediction of the internal pressures of various NBs (120 psi-240 psi). The developed methods and model framework are useful to unravel properties of NBs and support engineering applications of NBs.

In addition, Atomic Force Microscopy-Scanning Electrochemical Microscopy (AFM-SECM) has evolved to be a powerful tool for simultaneous topographical-electrochemical measurements at local material surfaces with high spatial resolution. Such

measurements are crucial for understanding structure-activity relationships relevant to a wide range of applications in material science, life science and chemical processes. The electrochemical behavior of surface NBs on gold substrate is measured by AFM-SECM, to better understand the chemical properties of NBs.

Moreover, this study investigates the effects of four types of NBs (air, oxygen, nitrogen, and carbon dioxide) on seed germination and plant growth. Nitrogen NBs exhibit considerable effects in the seed germination, whereas air and carbon dioxide NBs do not significantly promote germination. The growth of stem length and diameter, leave numbers, and leave width are promoted by NBs (except air). Furthermore, the promotion effect is primarily ascribed to the generation of exogenous reactive oxygen species (ROS) by NBs and higher efficiency of nutrient fixation or utilization.

**UNDERSTANDING THE INTERFACIAL PROCESSES OF REACTIVE  
NANOBUBBLES TOWARD AGRICULTURAL APPLICATIONS**

**by  
Xiaonan Shi**

**A Dissertation  
Submitted to the Faculty of  
New Jersey Institute of Technology  
in Partial Fulfilment of the Requirements for the Degree of  
Doctor of Philosophy in Environmental Engineering**

**John A. Reif, Jr. Department of Civil and Environmental Engineering**

**May 2022**

Copyright © 2022 by Xiaonan Shi

ALL RIGHTS RESERVED

**APPROVAL PAGE**

**UNDERSTANDING THE INTERFACIAL PROCESSES OF REACTIVE  
NANOBUBBLES TOWARD AGRICULTURAL APPLICATIONS**

**Xiaonan Shi**

---

Dr. Taha F. Marhaba, Dissertation Co-Advisor Date  
Professor and Chair of Civil and Environmental Engineering, NJIT

---

Dr. Wen Zhang, Dissertation Co-Advisor Date  
Associate Professor of Civil and Environmental Engineering, NJIT

---

Dr. Lucia Rodriguez-Freire, Committee Member Date  
Assistant Professor of Civil and Environmental Engineering, NJIT

---

Dr. Boris Khusid, Committee Member Date  
Professor of Chemical and Materials Engineering, NJIT

---

Dr. Huixin He, Committee Member Date  
Professor of Chemistry, Rutgers University-Newark

## BIOGRAPHICAL SKETCH

**Author:** Xiaonan Shi  
**Degree:** Doctor of Philosophy  
**Date:** May 2022

### **Undergraduate and Graduate Education:**

- Doctor of Philosophy in Environmental Engineering, New Jersey Institute of Technology, Newark, NJ, 2022
- Bachelor of Science in Environmental Engineering, Shandong University, Jinan, Shandong, P. R. China, 2012

**Major:** Environmental Engineering

### **Presentations and Publications:**

#### **Journal Publications:**

Xiaonan Shi, Shan Xue, Taha Marhaba, and Wen Zhang\*. "Probing Internal Pressures and Long-Term Stability of Nanobubbles in Water." *Langmuir* (2021).

Xiaonan Shi, Qingquan Ma, Taha Marhaba, and Wen Zhang\*. "Probing Surface Electrochemical Activity of Nanomaterials using Hybrid Atomic Force Microscope-Scanning Electrochemical Microscope (AFM-SECM)." *Journal of Visualized Experiments* (2020).

Xiaonan Shi, Weihua Qing, Taha Marhaba, and Wen Zhang\*. "Atomic Force Microscopy-Scanning Electrochemical Microscopy (AFM-SECM) for Nanoscale Topographical and Electrochemical Characterization: Principles, Applications and Perspectives." *Electrochimica Acta* (2019).

Ahmed Khaled Abdella Ahmed, Xiaonan Shi (Co-first author), Likun Hua, Leidy Manzueta, Weihua Qing, Taha Marhaba, and Wen Zhang\*. "Influences of Air, Oxygen, Nitrogen, and Carbon dioxide Nanobubbles on Seeds Germination and Plants Growth" *Journal of Agricultural and Food Chemistry* (2018).

Chunzhao Chen, Ling Chen, Yang Li, Wanyi Fu, Xiaonan Shi, Jiajun Duan, and Wen Zhang\*. "Impacts of Microplastics on Organotins' Photodegradation in Aquatic Environments" *Environmental Pollution* (2020).



- Weihua Qing, Yifan Wu, Xianhui Li, Xiaonan Shi, Senlin Shao, Ying Mei, Wen Zhang, and Chuyang Y. Tang\*. "Omniphobic PVDF Nanofibrous Membrane for Superior Anti-Wetting Performance in Direct Contact Membrane Distillation." *Journal of Membrane Science* (2020).
- Likun Hua, Han Cao, Qingquan Ma, Xiaonan Shi, Xuezhi Zhang, and Wen Zhang\*. "Microalgae Filtration using Electrochemically Reactive Ceramic Membrane: Filtration Performances, Fouling Kinetics and Foulant Layer Characteristics." *Environmental Science and Technology* (2020).
- Xinjie Wang, Yang Li, Jian Zhao, Xinghui Xia, Xiaonan Shi, Jiajun Duan, and Wen Zhang\*. "UV-induced Aggregation of Polystyrene Nanoplastics: Effects of Radicals, Surface Functional Groups and Electrolyte." *Environmental Science: Nano* (2020).
- Weihua Qing, Jianqiang Wang, Xiaohua Ma, Zhikan Yao, Yong Feng, Xiaonan Shi, Fu Liu, Peng Wang, and Chuyang Y. Tang\*. "One-Step Tailoring Surface Roughness and Surface Chemistry to Prepare Superhydrophobic Polyvinylidene Fluoride (PVDF) Membranes for Enhanced Membrane Distillation Performances." *Journal of Colloid and Interface Science* (2019).
- Weihua Qing, Xianhui Li, Senlin Shao, Xiaonan Shi, Jianqiang Wang, Yong Feng, Wen Zhang, and Weidong Zhang\*. "Polymeric Catalytically Active Membranes for Reaction-separation Coupling: A Review." *Journal of Membrane Science* (2019).
- Wang, Jianqiang, Hao Guo, Xiaonan Shi, Zhikan Yao, Weihua Qing, Fu Liu, and Chuyang Y. Tang\*. "Fast Polydopamine Coating on Reverse Osmosis Membrane: Process Investigation and Membrane Performance Study." *Journal of Colloid and Interface Science* (2019).
- Weihua Qing, Xiaonan Shi, Weidong Zhang, Jianqiang Wang, Peng Wang, Chuyang Y. Tang\*. "Solvent-Thermal Induced Roughening: A Novel and Versatile Method to Prepare Superhydrophobic Membranes." *Journal of Membrane Science* (2018).
- Weihua Qing, Xiaonan Shi, Weidong Zhang, Yajun Deng, and Chuyang Y. Tang\*. "Robust Polytetrafluoroethylene Superhydrophobic Nanofibrous Membrane for Oil/Water Separation." *Journal of Membrane Science* (2017).
- Weihua Qing, Jiangrong Chen, Xiaonan Shi, Jiaqian Wu, Jiayu Hu, Weidong Zhang\*, "Conversion Enhancement for Acetalization using A Catalytically Active Membrane in A Pervaporation Membrane Reactor." *Chemical Engineering Journal* (2017).

### **Patent Publications:**

Jianqiang Wang, Xiaonan Shi, Zhe Yang, and Chuyang Tang. "Preparation of Hand-Carry Gravity-driven Water Filter with High Throughput and Water Disinfection Performance." US Patent 11241660 (2022).

Biao Jiang, Changquan Qiu, Jixiang Li, Xiaonan Shi, Wenhao Pan, Wanjun Wang, Jing Yuan, and Liping Du. "Preparation and Application of a Magnetic Uranium Adsorbent." China Patent 104801262A (2015).

### **Oral Presentations:**

Xiaonan Shi, Taha Marhaba, and Wen Zhang. "Characterization of Colloidal, Mechanical and Electrochemical Properties of Nanobubbles in Water." (Abstract accepted) American Chemistry Society Spring National Meeting and Exposition, Online. (March 2020)

Xiaonan Shi, A.K.A Ahmed, Taha Marhaba, and Wen Zhang. "Influences of Air, Oxygen, Nitrogen, and Carbon dioxide Nanobubbles on Seeds Germination and Plants Growth", American Chemistry Society Fall National Meeting and Exposition, Boston, MA. (August 2018)

### **Poster Presentations:**

Xiaonan Shi, Taha Marhaba, and Wen Zhang, "Characterization of Nanobubbles and their Environmental and Agricultural Applications." NJIT Graduate Research Day, Newark, NJ. (November 2019)

Xiaonan Shi, Taha Marhaba, and Wen Zhang, "Characterization of Colloidal, Mechanical and Electrochemical Properties of Nanobubbles in Water." Eastern Analytical Symposium and Exposition, Plainsboro, NJ. (November 2019)

Xiaonan Shi, Taha Marhaba, and Wen Zhang. "Application of Nanobubbles in Biofilm Prevention and Removal." Stevens Conference on Bacteria-Material Interactions, Hoboken, NJ. (June 2019)

Xiaonan Shi, Taha Marhaba, and Wen Zhang, "Generation of Nanobubbles and their Agricultural and Environmental Applications." Student Research Poster Competition, New Jersey Water Environment Association John J. Lagrosa Conference, Atlantic City, NJ. (May 2019)

Xiaonan Shi, Taha Marhaba, and Wen Zhang. "Characterization of Nanobubbles and their Environmental and Agricultural Applications." NJIT Dana Knox Student Research Showcase, Newark, NJ. (April 2019)

Xiaonan Shi, A.K.A Ahmed, Taha Marhaba, and Wen Zhang. "Influences of Air, Oxygen, Nitrogen, and Carbon dioxide Nanobubbles on Seeds Germination and Plants Growth." Student Research Poster Competition, American Water Works Association New Jersey Section Annual Conference, Atlantic City, NJ. (03/2018)

*To my beloved husband,  
Weihua Qing,  
To my son,  
Ryan Qing*

## ACKNOWLEDGEMENTS

First, I would like to express my greatest thankfulness to my two fantastic dissertation co-advisors, Prof. Wen Zhang and Prof. Taha Marhaba, who gave me full support on my research and life. Prof. Zhang provides me with his continuous guidance and insightful suggestions on my research project and teaches me how to work in a highly efficient way. More importantly, under his supervision, I developed my method for solving problems and creating ideas in my research field. Prof. Zhang is so motivated and so cares about his students. He spends most of his time training his students. When I need to discuss my research with him or have some problems in my study, he always finds time to meet me, even though he is so busy. Because of Prof. Zhang's support, I got great opportunities to participate in multiple research projects, attend numerous international and regional conferences, get involved in proposal writing, and mentor students. I hope that I can be as lively, enthusiastic, and energetic as Prof. Zhang and someday be able to command an audience as well as he can.

My co-advisor, Prof. Marhaba, gives me his full support on my research project. Prof. Marhaba always takes time from his busy schedule as a department chair to meet me and discuss my situation and progress. He constantly shows his patience and understanding when I discuss questions on my research project and my pressure. I learned from him a new perspective for my research challenge and how to analyze a situation as a whole picture. Prof. Marhaba cares my research progress and my mental and physical health. He cares about every student in the Department of Civil and Environmental Engineering and does his best to give us a great study environment. I'm very proud of our CEE community.

It is especially my fortune to get admission from Prof. Marhaba as a new Ph.D. student in NJIT with the provost doctoral assistantship.

Special thanks go to my thesis committee members, Prof. Lucia Rodriguez-Freire, Prof. Boris Khusid, and Prof. Huixin He. I want to especially thank them for finding time in their busy schedules to review this thesis and provide constructive and critical comments.

I also want to show my great gratitude to my previous advisor, Prof. Chuyang Tang, at The University of Hong Kong, who has outstanding inspiration on scientific research and gave me lots of suggestions when I decided to pursue a Ph.D. degree in the US. Thanks to Dr. Jixiang Li and Dr. Changquan Qiu in Shanghai Advanced Research Institute, who gave me the best support in my application process. Additionally, I'd like to thank Prof. Ravi Jain, former Dean of the School of Engineering and Computer Science at the University of Pacific. He showed his support and encouragement in my career plan and decision to study in the U.S.

The financial support from the Department of Civil and Environmental Engineering, New Jersey Institute of Technology, U.S. Environmental Protection Agency, United States Department of Agriculture, New Jersey Water Resources Research Institute are gratefully acknowledged. Thanks to Center for Functional Nanomaterials in Brookhaven National Laboratory for the instrument support.

I want to thank all professors who gave great lectures and advice on my registered courses and are always glad to answer my questions for the classes. They are Prof. Wen Zhang, instructor of Environmental Microbiology (ENE661); Prof. Lucia Rodriguez Freire, instructor of Water Chemistry (ENE 663); Prof. Janet Bodner, instructor of

Advanced Spoken English (ENG505); Prof. Michael Hornsby, instructor of Site Remediation (ENE662); Prof. Eon Soo Lee, instructor of Introduction of Fuel Cell Energy Systems (ME618); Prof. Somenath Mitra, instructor of Advanced Analytical Chemistry (CHEM 764); Prof. Matthew Adams, Prof. Matthew Bandelt, Prof. Bruno Goncalves Da Silva, Prof. William Pennock, and Prof. Rayan Hassane Assaad, instructors of Graduate Seminar (CE791); Prof. Mirko Schoenitz, instructor of Kinetics of Reactions and Reactor Design (CHE612); Prof. Zafar Iqbal, instructor of Nanomaterials (CHEM 748); Prof. Michael Bonchonsky, instructor of Energy and Sustainability (EVSC 715); Prof. Pradyot Patnaik, instructor of Toxicology (EVSC 616); and Prof. Michel Boufadel, instructor of Physical Processes of Environmental Systems (ENE 630).

In addition, I received lots of help from professors and students at NJIT. I want to thank Prof. Boris Khusid and his student Mr. Qian Lei for sharing ideas of AC electrochemistry experiments. Thanks to Prof. Sagnik Basuray and his students, Mr. Zhenglong Li, Mr. Yu Hsuan Cheng, and Mr. Lixin Feng for their advice and permission on using instruments in their lab. Thanks to Prof. Kevin Belfield and Prof. Yanwei Zhang for letting me use the potentiostat in their lab and their students Jie Dou, Sweetie, May. Thanks to Prof. Michael Boufadel and his students Wen Ji and Ruixue Hu for letting and helping me use their oven. Thanks to Prof. Jay Meegoda and his students Shaini and Di Zhang for helping me with the set-up for the ozone nanobubble system. Thanks to Prof. Mengyan Li and his students, Fei Li and Dung Ngoc Pham for the help and suggestions on GC-MS tests. Thanks to Dr. Xueyan Zhang for her advice and training on AFM, SEM, TEM measurement and operation; Dr. Jeong Seop Shim for his advice and training on FTIR-microscopy; Dr. Larisa G. Krishtopa for her advice and training on GC-MS and LC-

QQQ. I want to thank Ms. Heidi Young and Ms. Sylvana Brito, our previous and current chair assistant, for providing a comfortable place for me to work and study. Also, I genuinely appreciate the kind help from Mr. Stephen George and Mr. Nasser Channaoui on my research.

Thanks to Prof. Thomas Olenik, Prof. Ashish Borgaonkar, and Prof. Author Crossan for their instruction and suggestions of teaching and communicating with students when I served as teaching assistants for their courses.

Moreover, the collaborators and professors from other universities and institutes helped me during my doctoral study. Thanks to Prof. Huxin He from Rutgers University for her advice on my electrochemical experiments; Thanks to Prof. Dmytro Nykypanchuk (Brookhaven National Laboratory, BNL) for the help and training on NBs characterization by NTA. Thanks to Dr. Mircea Cotlet (Brookhaven National Laboratory, BNL) and his student Dr. Jia Shiang Chen for the help and training on using Darkfield hyperspectral imaging. Thanks to Dr. Chunzeng Li (Bruker Cooperation) for the support and training on using Atomic Force Microscopy-Scanning Electrochemical Microscopy (AFM-SECM).

Thanks for all the help and guidance for my thesis review from Office of Graduate Studies in NJIT. Thanks to Ms. Clarisa Gonzalez-Lenahan, Dr. Sotirios Ziavras, Mr. David M. Tres, and Ms. Angela Retino.

Many thanks to my former and current group members Dr. Wanyi Fu, Dr. Likun Hua, Ahmed K, Ahmed, Qingquan Ma, Shan Xue, and Fangzhou Liu. I knew little about the project, instruments, and experiment methods when I began my research project. Ahmed, Wanyi, and Likun all gave me valuable suggestions and help. Dr. Fu drove me to the supermarket for an essential purchase on the first day I came to this city and the



weekends after. Dr. Hua had given me a ride to campus every weekday before buying a car. I would have much more difficulties in daily life without their help. After spending all these years together, we are true and lifetime friends learning, performing experiments, and figuring out questions. Thanks to all the students who visited or worked in the lab for the valuable help and support during my research. They are Chunzhao Chen, Leqi Lin, Xinyuan Wang, Ran Yan, Xiaoyu Wang, Zhifeng Hu, Anuj Verma, Evan Greff, Leidy Manzueta, Asha Mahmood for providing a stimulating and fun-filled environment. I also thank my classmates and friends, Keyuan Li and Bo Deng, who helped me on my core courses and gave me advice on my theoretical learning. It's my fortune to acknowledge the support of some remarkable individuals gratefully.

My husband, Weihua Qing, is my example of a qualified Ph.D. I would not succeed or even have begun my research journey as a Ph.D. without his's love, support, advice, and encouragement. I love him with all my heart and respect. Thanks to my son, Ryan Qing, born during my Ph.D. journey and the pandemic. He is such a sweet kid who eats well and sleeps well so that I could have time to work on the dissertation.

Finally, thanks to my mother Weiju Xiao and stepfather, Xianjun Sun, who gave me full support when I decided to pursue my Ph.D. degree. They are always there, support me with whatever I need, and whenever I need it. Thanks to my stepsister Qi Sun and brother Ping Sun, who take care of my mom and give me great love and support. Thanks to my parents-in-law, Sujuan Zhou and Shangfeng Qing, my sister-in-law Cuihua Qing, who gave me complete understanding and support on my decision to study abroad after getting married.

## TABLE OF CONTENTS

Chapter	Page
1 INTRODUCTION.....	1
1.1 Objective.....	1
1.2 Background and Challenges.....	1
1.3 Use of Novel Nanobubble Watering Processes for Enhanced Plant Growth and Pathogen Control.....	5
1.3.1 Need for Smart and Precision Agriculture for Water Source Protection, Soil Protection, and Pollution Prevention.....	5
1.3.2 Nanobubble Water as a Novel Irrigation Method: Opportunities and Challenges.....	7
1.4 Atomic Force Microscopy - Scanning Electrochemical Microscopy (AFM-SECM) for Nanoscale Topographical and Electrochemical Characterization: Principles, Applications and Perspectives.....	10
1.4.1 Introduction.....	10
1.4.2 AFM-SECM Principle, Probe Design, and Operation Mode.....	16
1.4.3 AFM-SECM Applications.....	36
1.4.4 Summary and Outlook on AFM-SECM Technique.....	55
2 COLLOIDAL CHEMISTRY AND CONTACT MECHANICS ANALYSIS OF REACTIVE NANOBUBBLES.....	58
2.1 Background and Challenges.....	58
2.1.1 Properties and Applications of NBs.....	58
2.1.2 Colloidal Stability and its Contributions from Mechanical Properties of NBs.....	60
2.1.3 Characterization of NBs.....	62
2.2 Materials and Methods.....	64

**TABLE OF CONTENTS**  
**(Continued)**

<b>Chapter</b>	<b>Page</b>
2.2.1 Production and Characterization of NBs in Water Under Different Injection Gas Pressures and Different Storage Temperatures.....	64
2.2.2 Modeling Analysis of Colloidal Stability of NBs in Water.....	66
2.2.3 Visualization and Mechanical Properties Assessment of NBs in Water.....	68
2.3 Results and Discussion.....	72
2.3.1 Effect of the Injection Gas Pressure on Bubble Size Distribution of NBs in Water.....	72
2.3.2 Visualization and Assessment of Mechanical Properties of Surface NBs in Water.....	75
2.3.3 Effect of Water Temperatures on Bubble Sizes and NB Concentrations.....	80
2.3.4 The Concentration Changes of NBs Under Different Water Temperatures and Storage Times.....	82
3 EC CHARACTERIZATION METHOD DEVELOPMENT FOR REACTIVE NANOBUBBLES.....	84
3.1 Background and Challenges.....	84
3.2 Materials and Methods.....	87
3.2.1 Nanobubbles Generation.....	87
3.2.2 Traditional Electrochemical Measurement in Bulk Solution.....	88
3.2.3 Topographical and Electrochemical Imaging by AFM-SECM.....	89
3.3 Results and Discussion.....	92
3.3.1 Traditional Electrochemical Measurements.....	92
3.3.2 Topography and Current Imaging of Oxygen NBs by AFM-SECM.....	94

**TABLE OF CONTENTS**  
**(Continued)**

<b>Chapter</b>	<b>Page</b>
4 INFLUENCES OF AIR, OXYGEN, NITROGEN, AND CARBON DIOXIDE NANOBUBBLES ON SEEDS GERMINATION AND PLANTS GROWTH.....	96
4.1 Background and Challenges.....	96
4.2 Materials and Methods.....	99
4.2.1 Production and Storage of NBs Suspensions Containing Air, O <sub>2</sub> , CO <sub>2</sub> , and N <sub>2</sub> .....	99
4.2.2 Examination of ROS Production in Water Suspension of NBs.....	101
4.2.3 Germination Tests.....	102
4.2.4 Plant Growth Tests.....	103
4.2.5 Statistical Analysis.....	104
4.3 Results.....	106
4.3.1 Effect of Different Types of NBs on the Germination Rates of Vegetable Seeds.....	106
4.3.2 Effect of NB Type on the Hypocotyl Length of Vegetable Seeds..	108
4.3.3 Effect of NBs Type on the Vegetable Growth.....	110
4.3.4 ROS Generation by NBs and Dissolved Oxygen Measurement....	116
4.4 Discussion.....	118
4.4.1 ROS Effects on Germination and Plant Growth.....	118
4.4.2 Effects of the Growth Elements Delivered by NBs.....	120
5 CONCLUSION AND OUTLOOK.....	122
REFERENCES.....	125

## LIST OF TABLES

Table	Page
1.1 Comparison of Several Hybrid AFM System Which Provide Simultaneous Topographical and Electrochemical Measurements.....	14
1.2 Summary of SECM Operation Modes.....	18
1.3 Summary of AFM Operation Modes.....	23
1.4 Summary of AFM-SECM Probe with Protruding Electrode.....	32
1.5 Summary of AFM-SECM Probes with Recessed Electrode.....	34
1.6 Summary of Simulation Method for AFM-SECM Probe Response.....	35
1.7 Summary of AFM-SECM Application.....	37
2.1 Parameter Values Utilized in the Colloidal Model Calculation in Equation (2.6) .....	73
2.2 Parameters Used in the Calculation of Bubble Size at Different Water Temperatures Using Equation (2.6) .....	82
2.3 Hydrodynamic Diameter, Zeta Potential and Dissolved Oxygen Level Of N <sub>2</sub> And O <sub>2</sub> NBs with Different Storage Time Under Room Temperature (20°C).....	83
3.1 Examples of Redox Mediators Used in Literatures.....	91
4.1 <i>P</i> Values For The T-Tests Between Control Groups (Irrigated By Tap Water Only) And The Test Groups That Underwent The Treatments With Different NB Waters On Seeds Germination And Plant Growth Data. Shaded Cells Indicate That $P > 0.05$ And Thus There Is No Statistical Difference Between The Test Group And Control Group.....	105

## LIST OF FIGURES

Figure	Page
1.1 (a) Schematic of a classic SECM instrument. (b) Working principle of AFM. (c) Schematic illustration of an AFM-SECM system.....	17
1.2 (a) Topography and current images of a gold surface bearing a high-density random array of ~20 nm Fc-PEGylated gold nanoparticles by AFM-SECM. (b) Simultaneously recorded topography and tip current images of a gold nanodot array. A vertical white dotted line is shown to indicate cross sections of the images taken along the column of nanodots.....	43
1.3 AFM-SECM imaging of Pt nanoparticles electrolessly deposited onto p <sup>+</sup> -Si substrate: (a) Surface topography. (b) Tip-contact current captured during the main scan. (c) Electrochemical current captured during the following lift scan...	44
1.4 AFM-SECM imaging of a gold electrode patterned onto a polydimethylsiloxane substrate. (a) 3D topography of the structure overlaid with Young's modulus; (b) Tip-current image; and (c) tip-sample adhesion image.....	45
1.5 (a) Simultaneously acquired height (first column), amplitude (middle column) and current images (last column) of the enzyme-containing periodic polymer. (b) Topography and current images of peroxidase activity.....	48
1.6 Illustration of AFM-SECM as a bio-lithography technique to electrochemically draw micro patterns for protein adsorption.....	49
1.7 Local AFM-SECM imaging results of coat proteins marked lettuce mosaic virus immobilized on a gold substrate. (a) topography and (b) tip current images. (c) 3D format of the tip current image which better show the string of current spots "borne" by the viruses. (d) Cross information of the topography and tip current images obtained along lines on the viruses from (a) and (b). (e) 3D titled views of the topography and tip current images.....	51
1.8 (a) Schematic illustration of reactions for glucose detection with a glucose oxidase-based biosensor. (b) Glucose calibration of an AFM-tip-integrated biosensor. (c) Topography and (d) current images of glucose transporting through a porous polycarbonate membrane.....	52
1.9 (a,b,d) Topography and (c) current images recorded by AFM-SECM at different scanning dimensions, (e) Current response of AFM-SECM probe (red line, right axis) and copper substrate (black line, left axis).....	55

**LIST OF FIGURES  
(Continued)**

<b>Figure</b>	<b>Page</b>
2.1 O <sub>2</sub> NBs and N <sub>2</sub> NBs kept in sealed sample tubes.....	65
2.2 Bubble size distribution in hydrodynamic diameter of (a) O <sub>2</sub> , (b) N <sub>2</sub> , (c) H <sub>2</sub> , and (d) CO <sub>2</sub> NBs under different injection gas pressures.....	74
2.3 The hydrodynamic diameters of four kinds of NBs in deionized (DI) water under different injection gas pressures. The solid and dotted lines indicate model predictions with different internal pressures used in Equation (2.6). <sup>1</sup> The difference in the NB hydrodynamic diameters produced under 80 psi and the data under 60 or 70 psi was analyzed by a one-way ANOVA ( <i>t</i> -test, two sided, a significance level of 0.05). The normality of replicate data was examined using the Shapiro Wilks <i>W</i> Test. *indicates a significant difference ( <i>p</i> < 0.05) between the two groups of data for the same NB types.....	75
2.4 Typical AFM morphological image (left), modulus mapping (middle) and stiffness mapping (right) of O <sub>2</sub> NBs (a) and N <sub>2</sub> NBs (b) on silicon wafer surface generated under different injection gas pressures: (a) 60 psi, (b) 70 psi, and (c) 80 psi.....	78
2.5 (a) and (b) are the Young's moduli of O <sub>2</sub> and N <sub>2</sub> NBs as measured by AFM (AFM-generated) and calculated by the JKR and DMT models; (c) O <sub>2</sub> and N <sub>2</sub> NB stiffness as measured by AFM under different injection pressures; and (d) comparison of the calculated internal pressure of O <sub>2</sub> and N <sub>2</sub> NBs and the injection gas pressure levels. Error bars are produced from the indentation uncertainties ( $\delta$ ) and adhesion force ( $F_{adh}$ ) read from force curves measured by AFM. The significance of difference for the comparison between the Young's moduli of NBs produced under 80 psi and the data under 60 or 70 psi was analyzed by a one-way ANOVA ( <i>t</i> -test, two sided, a significance level of 0.05). *indicates a significant difference ( <i>p</i> < 0.05) between the data groups with under-80 psi data. **indicates a significant difference ( <i>p</i> < 0.05) between the data group with the other two sets of data using the same specific injection pressure.....	79
2.6 (a) The force-distance curve showing the indentation ( $\delta$ ) of the AFM probe in contact with a bubble surface. (b) An illustration of the AFM tip geometry on the NB deformed surface.....	80

**LIST OF FIGURES  
(Continued)**

<b>Figure</b>	<b>Page</b>
2.7 (a) and (b) are the O <sub>2</sub> and N <sub>2</sub> NBs' size distribution produced under 60 psi; (c) the zeta potential of NBs in DI water; (d) a comparison of the observed and model-predicted NB diameters in DI water under different water temperatures. The significance of difference for comparison between the NBs' hydrodynamic diameter produced under 40 °C and the data under 6 or 20 °C was analyzed by a one-way ANOVA ( <i>t</i> -test, two sided, a significance level $\alpha = 0.05$ ).....	81
2.8 (a) O <sub>2</sub> and N <sub>2</sub> NB concentrations in DI water that were prepared at different temperatures and stored no more than 24 hours. (b) O <sub>2</sub> and N <sub>2</sub> NBs concentrations in DI water after storage in the dark at room temperature (20°C)..	83
3.1 (a) Set up of electrochemical measurements system. (b) Photo and schematic representation of the electrochemical cell.....	89
3.2 Schematic of AFM-SECM system.....	91
3.3 (a) Cyclic voltammetry of NBs water containing different types of gas. (b) Zoom view of the grey-squared part of (a).....	92
3.4 Nyquist plot of NBs water containing different types of gas. (b) Zoom view of the grey-squared part of (a).....	93
3.5 Simultaneously acquired topography (a) and tip current (b) images of oxygen NBs in electrolyte containing 10 mM [Ru(NH <sub>3</sub> ) <sub>6</sub> ] <sup>3+</sup> and 0.1 M KCl. The tip with a tip radius of 25 nm was biased at -0.4V (c) Schematic illustration of AFM-SECM measurement of NBs.....	95
4.1 Hydrodynamic diameter of ANBs, ONBs, NNBs, and CNBs.....	101
4.2 Image of the seeds. (a) Carrot; (b) Tomato; (c) Lettuce; (d) Fava bean.....	102
4.3 The setup of seeds germination tests.....	103
4.4 Real photo of the setup of the plants growth tests.....	104
4.5 Effect of different types of NBs on the germination rates of (a) lettuce, (b) carrot, and (c) bean.....	107
4.6 Effect of different types of NBs on the hypocotyl length during germination of (a) lettuce, (b) carrot, and (c) bean.....	109



**LIST OF FIGURES**  
**(Continued)**

<b>Figure</b>	<b>Page</b>
4.7 Photos of hypocotyl growth process of lettuce seeds at different submersion days.....	110
4.8 Influence of water type on number of leaves of tomato, carrot, and bean after 37 days. * denotes significant differences ( $p<0.05$ ) between the values of NB treatment groups and control group of the same kind of plants.....	111
4.9 Growth of beans taken after the first week of the test.....	112
4.10 Effect of different types of NBs on stem length of bean (a), carrot (b), and tomato (c) and stem diameter of bean (d), carrot (e), and tomato (f).....	113
4.11 Effect of different types of NBs on leaves length of bean (a), carrot (b), and tomato (c); and leaves width of bean (d), carrot (e), and tomato (f).....	115
4.12 Photos of tomato leaves after the same amount and freequency of watering by NBs water and tap water.....	116
4.13 Fluorescence intensity of different NBs water under sonication (100 W). * denotes significant differences ( $p<0.05$ ) between the values of NB groups and control group under same sonication time.....	117
4.14 The changes of dissolved oxygen levels in water suspension of different NBs....	118

# CHAPTER 1

## INTRODUCTION

### 1.1 Objective

There are four main objectives of this dissertation:

1. Unravel the internal pressure of nanobubbles (NBs) in water and provide new insights into the colloidal stability mechanisms of NBs. The developed methods and model framework will be useful to explain properties of NBs and support engineering applications of NBs.

2. Review the current state of knowledge on atomic force microscopy-scanning electrochemical microscopy (AFM-SECM) as well as its reported applications in three major research fields (materials science, life science, and chemical processes).

3. The electrochemical behavior of surface NBs on gold substrate was examined by AFM-SECM, to better understand the unique properties of NBs.

4. Explore a green irrigation technology using NBs in agriculture. Diverse NBs were used in plant growth experiments. The impacts of NBs on water quality, nutrient release and absorption were further investigated.

### 1.2 Background and Challenges

Microbubbles (MBs) are generally defined as gaseous bubbles with diameter less than 100  $\mu\text{m}$  and larger than 10  $\mu\text{m}$ .<sup>2</sup> Nanobubbles (NBs) are bubbles with a diameter of  $< 1 \mu\text{m}$  (also known as ultrafine bubbles).<sup>3</sup> The ultrasmall sizes of the micro- and nanobubbles (MNBs) elicit many intriguing properties.<sup>4,5</sup> For example, NBs have long residence times in the solutions because their buoyancy are outweighed by electrical forces<sup>6</sup> and increased

internal pressure.<sup>7</sup> Furthermore, the increased specific surface area of NBs increases the contact area between liquid and gas,<sup>8</sup> which facilitate mass transfer, sorption, and chemical reactions at the gas/liquid interface. Therefore, MNBs has been utilized as innovative technologies and versatile applications in agriculture, aquaculture, food engineering, sterilization, waste water treatment, and medical applications (e.g. drug delivery for chemotherapy<sup>9</sup>).<sup>10, 11</sup> The application of oxygen NBs on enhanced the oxygen concentration from 7.7 mg/L in normal distilled water to 31.7 mg/L after 30 minutes.<sup>12</sup> Thus, NBs are also used in aquaculture to improve the water quality and replenish dissolved oxygen, which increases the productivity of fish in limited space.<sup>13</sup> Preliminary market research conducted by the Fine Bubble Industries Association shows the size of the fine bubble business increasing from USD 20 million in 2010 to USD 4.3 billion in 2020.

The collapse of NBs creates shock waves, which in turn, promotes the formation of hydroxyl radicals ( $\bullet\text{OH}$ ), a highly reactive oxygen species (ROS) that nonspecifically reacts with and decomposes organic matters.<sup>14-16</sup> MBs have also been demonstrated to remove residual pesticides of vegetables and improve the quality of produce.<sup>17</sup> For example, Fenitrothion is an agricultural pesticide that is harmful to fish, animals, and humans. Ozone MBs were shown to remove and degrade fenitrothion in lettuce, cherry tomatoes, and strawberries.<sup>18</sup> The collapse of NBs creates the shock waves and promotes the formation of hydroxyl radicals which is highly reactive for pollutant degradation.<sup>14</sup> Applying NB in

water treatment could efficiently remove water contaminants<sup>2</sup> (e.g., rhodamine B,<sup>19</sup> p-nitrophenol,<sup>20</sup> and alachlor.<sup>21</sup>).

Water pollution in natural waters such as rivers and groundwater aquifers is a widespread problem that prevents these potentially potable sources from being used as drinking water. In the United States, approximately two-thirds of the over 1,200 most serious hazardous waste sites in the nation are contaminated with trichloroethylene (TCE), a potentially carcinogenic compound. TCE and 2,4,6-trichlorophenol (TCP), a carcinogenic and persistent pollutant, represent the large class of chlorinated organics responsible for the contamination of many potential drinking water sources around the world. Other emerging and environmentally persistent organic water pollutants For example, the occurrence of harmful algal blooms (HABs) is increasingly common in inland freshwater (lakes, ponds, reservoirs and rivers) across all 50 states in the U.S. and globally.<sup>22</sup> The accumulation of the microalgae associated with HABs could affect the color, taste, odor, turbidity of the surface water as well as additional negative impacts on the environment, human and animal health, and economy.<sup>23, 24</sup>

Many current treatments of contaminated water sources are chemical-intensive, energy-intensive, and/or require post-treatment of unwanted by-product formation. For example, to control, reduce or prevent the growth of HABs, commonly used techniques include ozonation, ultrasonic treatment, chlorination, and the dispersion of algae-killing chemicals (e.g., CuSO<sub>4</sub>). Other methods used to eliminate cyanotoxins produced from

HABs include flocculation, membrane filtration, adsorption on activated carbon, and oxidation by permanganate.<sup>25</sup> Each of these methods has inherent limitations in effectiveness or economic viability.<sup>26</sup>

Previous studies on nanobubbles indicated that NBs would generally exist in our natural world. They can exist in pure water at normal conditions, and a certain short time of decompressing would induce the formation of more NBs in bulk water.<sup>27</sup> The phenomenon indicated a balance between the nucleation and diffusion of gas molecules inside bulk water. Some NBs generation methods are based on creating a locally oversaturated state of gas to induce nucleation of gas molecules.

Micro/Nano bubble technologies<sup>2</sup> are expected to be less chemical consuming and have a considerable tendency of reducing size of the treatment facility. Hence, they have significant potential for design and operational cost reduction on top of their contribution as an environment friendly technique. With this regard, its application has a significant importance and future in water treatment because of the ability of the bubbles high mass transfer efficiency, relatively lower rising velocity, easily tailored surface charge, free radical generation ability and improved collision efficiency. Wide applications of MB and NB for particle separation, disinfection and organic-matter reduction have been anticipated via the high floatability of the bubble-particle aggregate, improvement of mass transfer and contact time, upgrading of aeration efficiency in biological wastewater treatment using bacteria, as well as enhancement of OH radical formation for advanced oxidation.

Moreover, free radical generation in the absence of chemicals makes the future applicability of oxygen and/or ozone MB and NB for the use of contaminant oxidation in water systems more attractive. The bursting energy of MB and improved aeration potential of NB have also a future in membrane de-fouling by improving surface scouring and reduction of sludge formation in membrane bioreactors. Finally, it can be stated that the use of both the MBs and NBs as an efficient and low-cost technology in different water treatment processes is yet the coming challenge considering the scaling up of the systems to industrial scale.

### **1.3 Use of Novel Nanobubble Watering Processes for Enhanced Plant Growth and Pathogen Control**

#### **1.3.1 Need for Smart and Precision Agriculture for Water Source Protection, Soil Protection, and Pollution Prevention**

Irrigated agriculture provides 40% of the world's food from less than 20% of the cultivated area highlighting the importance of irrigation in global food security.<sup>28</sup> However, agriculture is one of the main contributors to pollution of coastal and marine surface water.<sup>29, 30</sup> This leads to increasing nutrients and chemical pollution with a resulting decrease in water and sediment quality as reported worldwide.<sup>31-34</sup> Moreover, many farms must import resources that may be non-renewable (e.g. rock phosphate, fossil fuels), of limited or fluctuating availability (e.g. irrigation from groundwater and rivers), or subject to high and volatile prices (e.g. fuel, synthetic nitrogen fertilisers). The limit of natural

resources (production land, water, soil, and fertilizers) and the growth of population in the world requires agricultural systems to be more efficient and smarter than before.

Globally, 70% of the water use is applied in irrigation of crops, making irrigation the largest consumptive user of fresh water.<sup>35</sup> Over 80% of freshwater withdrawals in developing countries is applied in irrigation.<sup>36</sup> Agriculture therefore has the greatest contribution to water scarcity.<sup>37</sup> Global climate change may further increase irrigation water demand due to a greater variation in annual precipitation amounts.<sup>38</sup> It has been estimated that, by 2050, without improvement to current agricultural practice, the volume of water evaporated during crop production will almost double from today's levels.<sup>39</sup> Agricultural water management practice is therefore an important environmental corporate social responsibility issue and encouraging the adoption of more effective irrigation methods is of paramount importance. A global shortage in freshwater sources is predicted unless action is taken to improve water management and increase water use efficiency. This has necessitated greater regulatory demands for environmental protection of freshwater.<sup>40</sup>

Irrigation methods have considerable impacts on land erosion, pollution and water resource depletion. Conventional irrigation practice involves applying water uniformly over every part of the field without taking into account the spatial variability in soil and crop water needs; this consequently leads to over-irrigation in some parts of the field while other parts of the field are underirrigated.<sup>41</sup> The risks associated with over-irrigation include surface runoff, deep percolation and leaching of nitrates and nutrients. Those

associated with under-irrigation are more subjective and result in lower crop yields and quality, as well as inefficient use of fertilizer and other supplemental inputs for crop production. It is reported that only half of the total freshwater volume abstracted for irrigation globally reaches the targeted crops.<sup>36</sup> These have brought about the need to devise procedures to use the limited water more efficiently while maximizing crop yield and quality. By 1990, poor agricultural practices such as poor water management and fertilizer application, had contributed to the degradation of 38% of the crop land worldwide.<sup>42</sup> The increasing prices of fertilizer and concern over environmental impacts have created the need for precision agriculture (PA),<sup>43</sup> which utilizes latest technologies in an agricultural setting to increase efficiency and reduce detrimental environmental impacts of a farm.<sup>43</sup> Environmental legislation and concern around the application of potentially harmful agricultural chemicals, such as nitrate fertilizers, has also driven the development of PA.<sup>44</sup>

### **1.3.2 Nanobubble Water as a Novel Irrigation Method: Opportunities and Challenges**

MNBs and NBs have rapidly transformed into innovative technologies and versatile applications in agriculture, aquaculture, food engineering, and sterilization.<sup>10, 45, 46</sup> The application of oxygen NBs enhanced the oxygen concentration from 7.7 mg/L in normal distilled water to 31.7 mg/L after 30 minutes.<sup>12</sup> Thus, NBs are often used in aquaculture to improve water quality and replenish dissolved oxygen, increasing fish productivity in limited space.<sup>13</sup> Applying NBs in water could efficiently remove water contaminants as



well. For example, Fenitrothion is an agricultural pesticide that is harmful to fish, animals, and humans. Ozone MBs were shown to remove and degrade fenitrothion in lettuce, cherry tomatoes, and strawberries.<sup>18</sup>

NBs have been introduced into agricultural applications (e.g., promoting plant growth and germination).<sup>12, 47-49</sup> For example, Seiichi Oshita et al. showed accelerated seed germination rates in mixed nitrogen and air NBs water compared to that in distilled water, and indicated that NBs promoted physiological activity of plants because of the generation of exogenous ROS and increased the mobility of the water molecules in bulk.<sup>48, 49</sup> Germination rates of barley seeds submerged in water containing NBs (bubbles formed from gas mixtures of nitrogen and pure air) were 15–25% greater than seeds submerged in distilled water with the same concentration of dissolved oxygen.<sup>50</sup> In addition, MNBs have proven to facilitate the growth of plants such as lettuce in the nutrient solutions.<sup>51</sup> Water containing air MNBs led to 2.1 times greater fresh lettuce leaf weight and 1.7 greater dry leaf weight than macro-bubble treated plants.<sup>52</sup> Moreover, rice growth did not differ between plants irrigated with NB water (water-saturated by oxygen nanobubbles) and those irrigated with control water (without nanobubbles). Still, MNB water significantly reduced cumulative CH<sub>4</sub> emission during the rice-growing season by 21%.<sup>53</sup> The amounts of iron, manganese, and arsenic that leached into the drainage water before the MNB water also reduced whole rice heading. Most of these previous studies used MNBs for plant growth promotion and only a few of them employed NBs (or at least without the control of bubble

size or size informality).

An increasing body of evidence also signifies the importance of the root microbiome, which consists of the complex of rhizosphere-associated microbes, their genetic elements and their interactions, in determining plant health and growth. The rhizosphere, which is the narrow zone of soil influenced by root secretions, can contain up to  $10^{11}$  microbial cells per gram root<sup>8</sup> and more than 30,000 prokaryotic species.<sup>54</sup> In humans, the effects of intestinal microbial communities on health are becoming increasingly apparent.<sup>55</sup> The diversity of microbes associated with plant roots (or Rhizobacteria) is enormous (tens of thousands of species). This complex plant-associated microbial community, also referred to as the second genome of the plant, is crucial for plant health and growth. Recent advances in plant–microbe interactions research revealed that plants can shape their specific rhizosphere microbiome when grown on the same soil. Upon exposure to environmental stimuli such as pathogen or insect attack or exposure to organics, plants enhance microbial activity to suppress pathogens in the rhizosphere or elevate nutrient uptake.<sup>56</sup> Thus, a comprehensive understanding of the mechanisms that govern selection and activity of the rhizosphere microbial communities by plant roots after exposure to NBs will provide new opportunities to increase crop production using NB irrigation, which has not been reported previously.

## **1.4. Atomic Force Microscopy - Scanning Electrochemical Microscopy (AFM-SECM) for Nanoscale Topographical and Electrochemical Characterization: Principles, Applications and Perspectives**

### **1.4.1 Introduction**

Electrochemistry deals with the interplay between electricity and identifiable chemical change. Characterization of electrochemical (EC) behavior of liquid/liquid, liquid/gas and liquid/solid interfaces can provide critical insights into the kinetics and mechanisms of interfacial reactions across the interface, and thus plays a significant role for the fundamental understanding of many biological and chemical processes. Up to date, based either on potentiometric or voltametric measurements, various electrochemical characterization techniques have been developed, including cyclic voltammetry <sup>57</sup>, polarography <sup>58</sup>, electrochemical impedance spectroscopy <sup>59</sup>, and electrochemical noise measurement <sup>60</sup>. However, these traditional EC measurements are usually performed at macroscopic scale and can only provide an average of the heterogeneous reactivity over an electrode surface. Such information is becoming insufficient to reveal local scale surface properties, especially in modern world where nanomaterials are widely integrated. Therefore, localized techniques capable of simultaneously capturing both nanoscale multidimensional information and electrochemistry are highly desirable.

Scanning electrochemical microscopy (SECM) emerges as a popular and well-established approach for local electrochemical studies at micro- and nanoscales <sup>61-65</sup>. In a classic SECM characterization process, an ultra-small microelectrode, often termed as

“ultramicroelectrode” in SECM literature, is defined as an electrode with dimension smaller than  $25\ \mu\text{m}$ <sup>66</sup> that is placed in close proximity to the sample surface and then scans across the immersed surface. Spatially resolved electrochemical signals can be acquired at the ultramicroelectrode tip (or at the substrate in response to the tip) as a function of precise tip position over a substrate region of interest<sup>67</sup>. SECM has evolved significantly after its first inception in 1989<sup>68, 69</sup> owing to the rapid development of functional probe types and operation modes for widespread applications. Several review articles have been available now in which the principles, experimental design and applications were comprehensively discussed<sup>61, 70</sup>. However, EC signals are typically sensitive to tip-substrate interaction characteristics such as working distance. Most of the classic SECM often applies a constant height approach, instead of a more favorable fixed tip-substrate distance, which easily results in the convolution of collected topographical and electrochemical information<sup>71</sup>. Additionally, it remains a challenge for the classic SECM to obtain sub- $\mu\text{m}$  image resolution because its electrodes often have characteristic dimensions of a micrometer-scale that limits the spatial resolution<sup>72</sup>.

The ongoing limitations of classic SECM has spurred the development of a variety of advanced SECM techniques in which various positional feedback methods are integrated to enable a fixed tip-substrate working distance such that signals of EC properties of the surface are collected at the probe, including shear force positioning<sup>73</sup>, ion conductance positioning<sup>74</sup>, atomic force microscopy (AFM) positioning, and alternating current SECM

<sup>75</sup>. Among the several techniques, SECM integrating AFM positioning (AFM-SECM) is believed to be more superior because AFM is well-recognized for its high-spatial-resolution imaging capability and precisely controllable AFM tip positioning. The integration enables simultaneous acquisition of high-spatial-resolution surface topology and nanoscale electrochemical images. The first successful demonstration of AFM-SECM was reported by MacPherson and Unwin in 2000, who simultaneously acquired the topographical and electrochemical images of track-etched polycarbonate ultrafiltration membranes and potassium ferrocyanide trihydrate crystal surfaces <sup>76</sup>. Afterwards, significant advancements have been achieved in the fields of combined AFM-SECM probe design and fabrication, as well as diverse applications in chemical, biological and material characterization. Although remarkable progress of AFM-SECM, almost all the previous review papers only examined either SECM <sup>61, 70</sup> or AFM <sup>77</sup>. Only one article reviewed multifunctional AFM and covered limited information on AFM-SECM <sup>72</sup>. Clearly, a critical review specifically focusing on the integrated AFM-SECM is highly needed.

The present review aims to summarize the current state of knowledge on AFM-SECM as well as its reported applications. Fundamental working principles and innovative operations pertaining to SECM, AFM and the combined AFM-SECM mode is briefly presented first. Then, we introduce the basics of the AFM-SECM probe designs, followed by a critical overview and discussions on the applications of AFM-SECM in three major research fields (materials science, life science, and chemical processes). The current

limitations and drawbacks of the AFM-SECM are also elaborated with extensive example case studies. Finally, conclusions and outlook are given to provide insights into the future development of AFM-SECM. It should be noted here that a number of studies also reported simultaneous topographical and electrochemical measurements, which were achieved by other techniques such as conductive AFM <sup>78-81</sup>, electrochemical AFM (EC-AFM) <sup>82-85</sup>, scanning ion conductance microscopy-scanning electrochemical microscopy (SICM-SECM) <sup>74, 86</sup>, and scanning electrochemical cell microscopy (SECCM) <sup>87, 88</sup>. **Table 1.1** present a comparison between these techniques, which fall outside the scope of the present review on AFM-SECM.

**Table 1.1** Comparison of Several Hybrid AFM System Which Provide Simultaneous Topographical and Electrochemical Measurements

Techniques	Principles	Substrates	Main advantages	Main drawbacks	Ref.
AFM-SECM	The probe measures tip-substrate interactive forces to image topography, and simultaneously record faradaic current (or potential) response to map electrochemical activity of the sample surface.	Conductive, nonconductive, soft, fragile, and hard samples.	1. Precisely controllable probe tip positioning; 2. Nanoscale resolution for topographical and electrochemical imaging;	1. High probe cost; 2. Limited probe reliability and durability; 3. Requires the entire sample to be immersed in electrolyte solution, which may compromise tip and sample stability by fouling or contamination	72
CAFM <sup>a</sup>	The probe measures tip-substrate interactive forces to image topography, and record current flow at the tip-substrate contact point to measure local electrical properties such as conductivity.	Mostly used on conductive or dielectric materials	1. No electrolyte solution needed and can be operated in air or vacuum; 2. Well-developed technique; 3. Wide probe availability with competitive probe price	1. Possible degeneration of the conductive coating of the tip and sample surface due to undesirable electrochemical reasons; 3. Mostly used on conductive, 2. Difficult for biological sample measurement.	78-81, 89
EC-AFM <sup>a</sup>	EC-AFM integrates classic AFM with a three electrode electrochemical cell to enable <i>in situ</i> AFM measurement of sample surface morphology while conducting electrochemical experiments.	Conductive samples, such as electrode.	1. Real-time and <i>in situ</i> conductive surface evolution measurement; 2. Wide probe availability with competitive probe prices	1. Requires the entire sample to be immersed in electrolyte solution, which may compromise tip and sample stability by fouling or contamination; 2. Possible corrosion to AFM cantilever when in acid electrolyte; 3. Frequent photodiode repositioning due to change of the laser spot position (resulted from change of solution refractive index with respect to air).	82-85, 90

**Table 1.1** Comparison of Several Hybrid AFM System Which Provide Simultaneous Topographical and Electrochemical Measurements

Techniques	Principles	Substrates	Main advantages	Main drawbacks	Ref.
SICM-SECM <sup>a</sup>	Ion-migration current between two quasi-reference counter electrodes is measured to determine the height profile (topography), and faradaic current (or potential) response of the probe is simultaneously recorded to determine electrochemical activity.	Hard or soft, non-conducting samples	<ol style="list-style-type: none"> <li>1. Accurate probe tip positioning;</li> <li>2. High-resolution topographical/electrochemical imaging;</li> <li>3. Generally non-contact with the samples, and thus non-destructive and can be advantages for observation of living tissues and cells, and biological samples.</li> </ol>	<ol style="list-style-type: none"> <li>1. Lacking of commercial probe suppliers;</li> <li>2. Positioning instrumentation for combined SICM-SECM is relatively specialized;</li> <li>3. Though producing high image resolution, it is still not competitive when compared to AFM-SECM</li> <li>4. Theory is mostly based purely on SICM, and theory for combined SICM-SECM is currently inadequate.</li> </ol>	65, 74, 86
SECCM <sup>a</sup>	SECCM measures the changes of ion conductance current between the quasi-reference counter electrodes to generate height profile, and measures the current flow caused by redox of any active species in the electrolyte at the sample surface to image electrochemical activity	(Semi)conducting substrates, such as polycrystalline platinum, carbon materials, etc.	<ol style="list-style-type: none"> <li>1. A defined portion of the surface is targeted and isolated for investigation, free from the influence of neighboring areas;</li> <li>2. Only the probed part of the surface comes into contact with solution for a very brief time, which is particularly useful for systems where surface passivation, fouling, corrosion are otherwise problematic;</li> <li>3. The interfacial reaction or property is probed directly, with minimal convolution from tip and topographical effects.</li> </ol>	<ol style="list-style-type: none"> <li>1. Recently introduced in 2010, and relatively underdeveloped when compared to other topographical / electrochemical measurement techniques;</li> <li>2. Double-barrel pipette needs to be further reduced to open up more possibilities.</li> </ol>	87, 88

<sup>a</sup>. CAFM (Conductive Atomic Force Microscopy); EC-AFM (Electrochemical Atomic Force Microscopy); SCIM-SECM (Scanning Ion Conductance Microscopy - Scanning Electrochemical Microscopy); SECCM (Scanning Electrochemical Cell Microscopy)

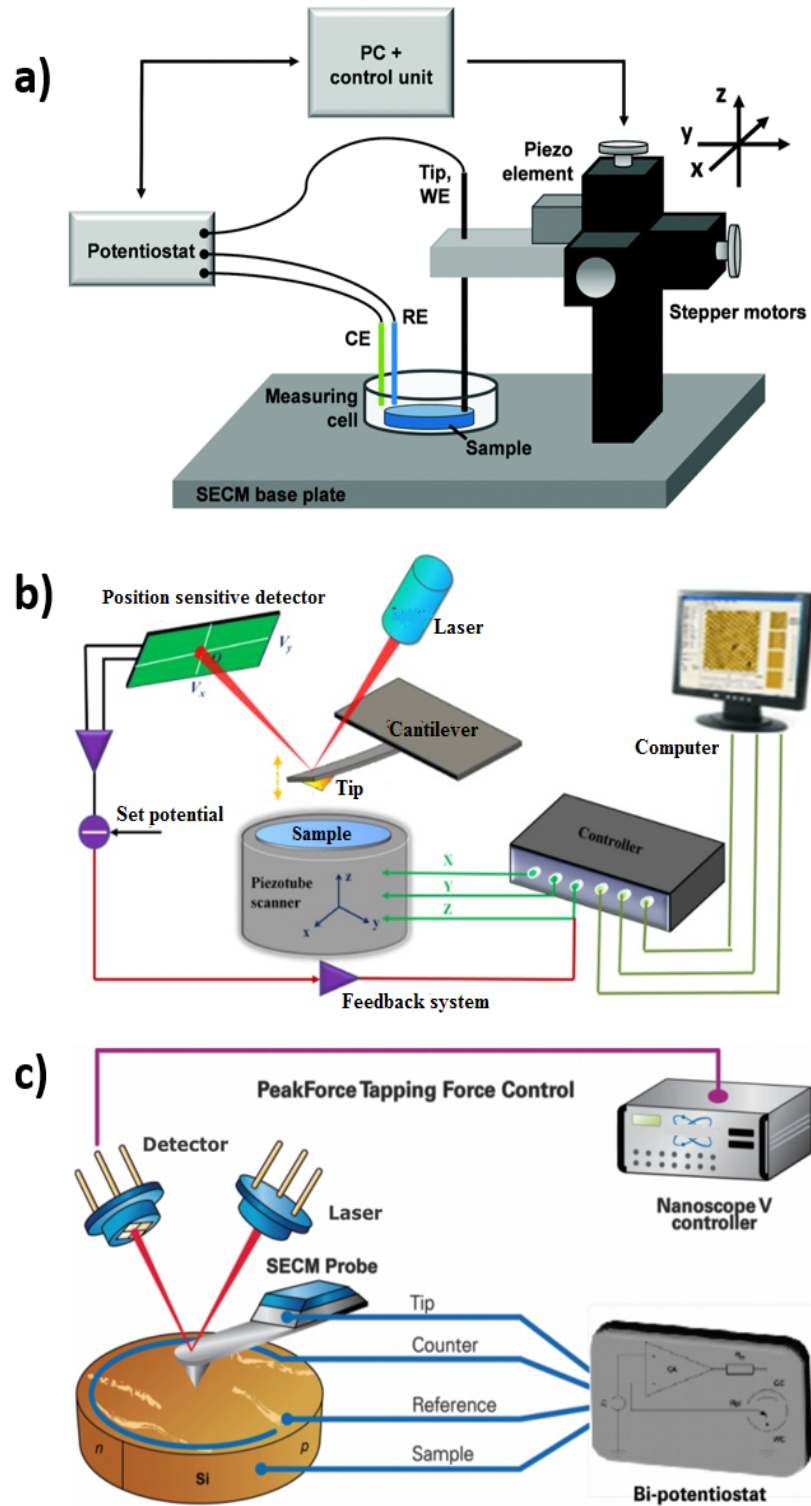


## 1.4.2 AFM-SECM Principle, Probe Design, and Operation Mode

**1.4.2.1 AFM-SECM Principles.** Detailed introductions of single SECM and AFM techniques are certainly beyond the scope of the present work, a brief description of their principles and operations is presented in Subsections 1.4.2.1.1 and 1.4.2.1.2 to facilitate the understandings of the combined AFM-SECM technique in Subsection 2.1.3.

### *1.4.2.1.1 SECM*

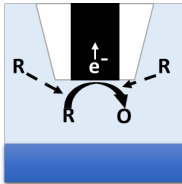
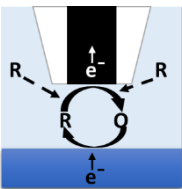
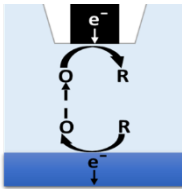
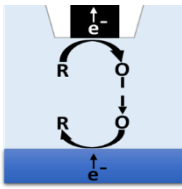
SECM technique was first developed by Bard, et al.<sup>68</sup> and Engstrom, et al.<sup>69</sup> concurrently in 1989. It uses an ultramicroelectrode to closely scan across an immersed substrate surface of interest. Spatially resolved electrochemical signals can be acquired at the ultramicroelectrode tip (or at the substrate in response to the tip) to provide quantitative information about the interfacial region<sup>61</sup>. A classic SECM instrument consists of three key components (**Figure 1.1a**)<sup>70</sup>: (1) A potentiostat precisely measures and controls the potential and current at both a ultramicroelectrode and a substrate; (2) A positioning system with high resolution enables the accurate movement of a substrate and a probe and; (3) A SECM tip with dimensions of micrometer to nanometer range scans across an immersed substrate.



**Figure 1.1** (a) Schematic of a classic SECM instrument. (b) Working principle of AFM. (c) Schematic illustration of an AFM-SECM system.

Source: The figure is reproduced from Ref<sup>91</sup> published by the PCCP Owner Societies, Ref<sup>92</sup> and Ref<sup>93</sup> with copyright.

**Table 1.2** Summary of SECM Operation Modes

Type	SECM mode	Reaction	Schematic illustration	Principle	Typical applications
a	Feedback mode	$R - ne^- \rightarrow O$ (tip reaction)		Probe tip approaches an inert surface. Hindered diffusion of <i>R</i> to the tip by the substrate. The current decreased, compared to steady-state conditions.	Most common mode Corrosion Enzymatic measurements Reaction kinetics Substrate modification Surface catalytic activity
				A probe approaches a conducting substrate. Species <i>O</i> is reduced back to <i>R</i> due to the conducting substrate. The current increased, compared to steady-state conditions.	
b	Generation/collection mode	$R - ne^- \rightarrow O$ (substrate reaction) $O + ne^- \rightarrow R$ (tip reaction)		Generate the redox species at substrate and collect the species at the tip.	Corrosion Enzymatic measurements
		$O + ne^- \rightarrow R$ (substrate reaction) $R - ne^- \rightarrow O$ (tip reaction)		Generate the redox species at tip and collect the species at the substrate	Reaction kinetics Substrate modification

**Table 1.2** Summary of SECM Operation Modes

Type	SECM mode	Reaction	Schematic illustration	Principle	Typical applications
c	Redox competition (RC) mode	$R - ne^- \rightarrow O$ (substrate and tip reaction)		The substrate and the probe compete for the same electro-active species in solution. A drop in tip current indicates the surface electro-activity.	Surface catalytic activity Corrosion
19	Direct mode	$R - ne^- \rightarrow O$ (tip reaction)		The probe acts as a counter electrode. A substrate acts as a working electrode. There is a localized electric field between the substrate and tip.	Surface modification
	e	Potentiometric mode	No faradaic reaction		The local potential is measured at probe (not the current). An ion-selective electrode (ISE) is needed. No faradaic reaction and the tip-to-substrate is less important in this mode.

Over the years, different operation modes of SECM have been developed to accommodate expanding applications, including feedback mode, generation/collection mode, redox competition mode, direct mode, and potentiometric mode (as summarized in

**Table 1.2):**

(1). Feedback mode is the most common used SECM mode due to its great versatility (**Table 1.2a**). In this mode, a tip reaction occurs with a redox species  $R$  introduced into an electrolyte solution and oxidized at the biased tip. A negative feedback response would be generated if approaching the probe towards an inert substrate, because the diffusion of redox species  $R$  to the tip will be suppressed by the substrate, and thus leads to a reduction in current compared to steady state conditions. Alternatively, a positive feedback response can be observed when the probe approaches towards a conducting surface because the conducting surface enables species  $O$  to be reduced back to  $R$ , which promotes the local flux of  $R$  and thus increases the current.

(2). Generation/collection mode (GC) operates when the tip selectively detects species formed at the substrate or the probe tip (**Table 1.2b**). In the case of redox reaction originated from the substrate, i.e., substrate generation/tip collection (SG/TC) mode, a mediator species is formed at the substrate and then collected at the biased tip (reaction details shown in **Table 1.2b**). Despite of the successful applications in corrosion<sup>94,95</sup> and enzymatic studies<sup>96,97</sup>, this GC mode suffers from some inherent drawbacks such as lack of steady state at large substrate, low collection efficiency, and interference between tip and substrate reaction<sup>70</sup>. Conversely, redox reaction may also be originated from the tip (tip generation/substrate collection, TG/SC mode), in which the mediator species is formed at the tip and then collected at the substrate. This mode has been predominantly applied for reaction kinetics<sup>98,99</sup> or substrate modification measurements<sup>100</sup>.

(3). Redox competition (RC) mode (**Table 1.2c**), as introduced by Schumann et al.<sup>101</sup>, is a mode where the substrate and the probe compete for the same redox species in solution during the tip-substrate scanning. In this mode, potentials are applied to both the tip and the substrate by a bipotentiostat, but current is only measured at the tip. The tip current remains constant when scanning across inactive region of the substrate, whereas it decreases when scanning over active region due to the consumption of redox species consumption at both the tip and the substrate. The current drop can be further correlated to substrate surface activity. Although RC mode is less popular when compared to feedback mode or GC mode, it still finds a niche in studies of corrosion<sup>102</sup>, cell respiration activity<sup>103</sup>, and surface catalytic activity<sup>104, 105</sup>.

(4). Direct mode can be regarded as a specific SECM subset, because this mode reverses the electrochemical cell configuration and utilizes the substrate as the working electrode and the probe tip as the counter electrode (as illustrated in **Table 1.2d**). When a potential is applied, the localized electric field is formed between the substrate and the tip, and the close tip-to-substrate distance enables higher patterning resolutions. In contrast to feedback mode, the reactions at the substrate and SECM probe in direct mode do not necessarily need to be reductions and oxidations of the same redox couple<sup>106</sup>. This mode is particularly popular for surface modification<sup>107</sup>, especially for enzyme deposition<sup>108</sup>, semiconductor etching<sup>109</sup> and micro-patterning measurements<sup>110</sup>.

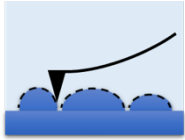


(5). In contrast to the above described modes which all involve an amperometric measurement, potentiometric mode, however, measures a local potential (instead of current) between an external reference electrode and an ion-selective electrode (**Table 1.2e**)<sup>111, 112</sup>. Notable advantages of this mode include high selectivity, high sensitivity, and ability to detect electroactive and non-electroactive species<sup>113</sup>. Another unique feature of the mode is that the oxidation state and concentration of the analyte species remain stable during the entire measurement because no faradaic reaction is involved. Moreover, since the measured local potential is often linearly related to the analyte activity, the tip-substrate distance barely affects the corresponding signals, and therefore the distance is less important when compared to other operational modes (especially feedback mode which is heavily affected by the tip-substrate distance).

#### *1.4.2.1.2 AFM*

AFM was first introduced in 1986<sup>114</sup>, and now has evolved to be a powerful and indispensable tool for surface characterization especially at the nanoscale. Extensive

review papers have reported different applications in different research areas such as catalysis, material science, medicine, molecular biology, polymer chemistry and physics<sup>77, 115-117</sup>. In principle, AFM uses a cantilever with a sharp tip (probe) to scan the sample surface and measures the interaction between the sample surface and the tip for imaging or quantification of tip-sample forces (as depicted in **Figure 1.1b**)<sup>118-120</sup>. Specifically, when the tip is brought to proximity of the sample surface, the tip-surface interaction leads a deflection of the cantilever and changes the deflection signal of the incident laser beam at the backside of the cantilever. When the tip scans across the sample surface, its vertical and horizontal motion will be recorded by measuring the laser deflection signal by a photodetector. The laser signal is then processed into a three-dimensional topography of the sample surface<sup>121</sup>.

**Table 1.3** Summary of AFM Operation Modes

AFM modes	Schematic illustration	Principle	Typical Applications
Contact mode		<p>The probe tip is not oscillated, but constant contacted with a sample surface, and is operated in a repulsive regime. The cantilever tip moves up and down to accommodate the surface topography which can be measured by either the cantilever deflection or using a feedback loop to keep the cantilever at a constant position.</p>	<p>Non-fragile sample such as mineral particles, graphene film</p>
Non-contact mode		<p>The cantilever tip is kept away from the substrate surface and oscillate the tip with small amplitude near or at its resonance frequency. Tip-surface interaction induces oscillation changes but is maintained by a feedback loop system by adjusting the average tip-to-sample distance which can be further used for topography imaging.</p>	<p>Metals, semi-conductors, polymers, biological materials</p>
Intermittent mode		<p>The cantilever tip oscillating with a large amplitude is kept away from the substrate surface, and intermittently contact with the sample surface. Tip-surface interaction induces oscillation changes, but a feedback system is used to adjust the cantilever height to maintain a preset oscillation amplitude.</p>	<p>Most popular mode. Soft samples such as hydrophilic polymers or biological specimens</p>



Similarly, several imaging modes of AFM have been developed for a variety of applications <sup>119</sup>. For practical guidance purposes, the most primary AFM modes including contact mode, non-contact mode, and intermittent mode are introduced (summarized in **Table 1.3**). Depending on the oscillation state of the cantilever, these imaging modes can also be divided into static mode (non-oscillating cantilever) and dynamic mode (oscillating cantilever). Since the three imaging modes have been well-documented elsewhere <sup>118-120</sup>, only a brief introduction is presented here.

Contact mode, also known as non-oscillating mode or repulsive mode <sup>116</sup>, is the first mode developed for AFM. In this mode, the cantilever is not oscillated, and the probe tip is held in close contact with the sample surface during the scanning process, and therefore the mode usually operates at the repulsive regime of the force-distance curve. The surface topography is imagined by either the cantilever deflection directly, or the feedback signal required to maintain constant cantilever position. Due to the direct contact, unfavorable surface and/or tip damage may occur by a lateral shear force exerted by the probe tip. Therefore, low stiffness cantilevers with low spring constant are more favorable for this mode to scan non-fragile or solid surfaces <sup>122, 123</sup>.

By contrast, the non-contact mode (also named as close-contact mode) is performed by lifting the probe tip slightly away (50~150 Å) from the substrate surface with oscillation of the probe tip typically near or at its resonance frequency. In principle, as the oscillating tip approaches a sample surface, tip-surface interaction would induce damping of the

cantilever oscillation. This leads to a reduction of the oscillation in frequency, amplitude or phase, which are recorded by a force transducer. Together with a feedback loop system, a constant oscillation amplitude or frequency is maintained by adjusting the average tip-to-sample distance. Measuring the tip-to-sample distance at each data point allows for the construction of a topographic image of the sample surface. In the case of the non-contact mode, usually a small oscillation amplitude (often the order of 10 nm<sup>118</sup>) is applied so that the cantilever is maintained only in the attractive regime of the force-distance curve. This mode usually uses frequency modulation for detection, which is why the non-contact mode is also called a frequency modulation mode. Without direct contact between the tip and the sample surface, this mode shows higher versatility for a wide range of samples, especially for soft surface (e.g., polymers<sup>124</sup>, biological specimen<sup>117</sup>) and contamination-sensitive surface characterization. The non-contact mode is usually applied in high vacuum condition<sup>125-127</sup> and also in solutions<sup>128</sup>, whereas for imaging in air, a contamination layer is often presented on most sample surface due to water or moisture adsorption, which may induce capillary forces between the probe and the contamination layer and negatively interfere the tip-surface interaction<sup>118</sup>.

Intermittent-contact mode, also commonly known as tapping mode, uses a larger oscillation amplitude (typically in the range of several to 200 nm<sup>129</sup>), during which the tip-sample interactions moves from locations far from the sample surface (no tip-sample interaction) to close contact, covering the attractive and repulsive regimes in the force-

distance curve. The feedback system is usually based on amplitude modulation, so the intermittent-contact mode is also widely referred to as amplitude modulation mode. Intermittent-contact mode can be operated in liquid and air for imaging soft as well as fragile samples. The versatility of this intermittent-contact mode are mostly attributed the facts that: 1) the lateral forces which cause huge problems in contact mode are avoided, so sample or tip damage during scanning is minimum; 2) the probe tip in intermittent-contact mode can pass through the contamination layer during the imaging in air to detect the actual surface of interest <sup>118</sup>.

#### *1.4.2.1.3 AFM-SECM*

Instrumentally speaking, combining SECM with AFM is straightforward: an external (bi)potentiostat is integrated into an AFM instrument to enable the additional function of electrochemical measurement (as shown in **Figure 1.1c**). The electrochemical data can then be fed in via an analog-to-digital conversion channel provided by the AFM controller. The probe of the AFM-SECM here acts as not only a force sensor for topography imaging, but also an electrode for electrochemical imaging. Though different operation modes of AFM-SECM may be applied (see the following Subsection 1.4.2.2) for specific applications, the working principles are identical to those introduced above.

However, the SECM and AFM combination is not simply a pathway for simultaneous measurements of topography and electrochemical activity of the sample

surface, but more of an elegant solution to the above-mentioned SECM challenges. For instance, the constant tip-substrate distance undesirably leads to the convolution of topography with the measured electrochemical information, and conventional micrometer-scale SECM electrode limits the spatial resolution of the measured images. By contrast, AFM has excellent tip positioning ability to enable fixed tip-substrate working distances that decouples the topographic and electrochemical information. Moreover, the sharp AFM tips permit nanoscale spatial resolution imaging.

**1.4.2.2 AFM-SECM Operation Mode.** Contact mode in AFM-SECM is explored in the first demonstration of combined AFM-SECM by Macpherson and co-workers<sup>76</sup>. Like the AFM's contact mode (see Subsection 1.4.2.1.2), the probe in this AFM-SECM mode is also in direct contact with the sample surface during the entire measurement process. The cantilever tip moves up and down to accommodate the sample surface topography while a feedback loop keeps a constant predetermined cantilever deflection. Both the imaging of surface topography and electrochemical activity (e.g., through tip-sample reactions in Table 1.1) can be achieved in single scanning pass. This mode is not recommended for fragile and soft sample surface measurement due to high imaging and shear force but can be applied to robust and nonconductive substrates using a probe with electrode at the apex. To apply this mode for conductive surfaces, probes with recessed

electrode (see Table 1.4) must be used to avoid short circuit between the electrode and conductive sample surface.

As mentioned above, the actual tip-substrate distance changes with the local topography for a substrate displaying corrugations, and thus, the variation of the tip position is a convoluted function of the substrate topography and local reactivity. In this case, a lift mode AFM-SECM was developed to enable constant tip-to-substrate distance imaging<sup>130, 131</sup>. In this imaging mode, twice scanning across each line of the image are conducted: surface topography is measured and stored in the first scanning, followed by a second pass during which the probe tip is first slightly lifted away from the sample surface and then scanned again along the same lines as in the first scanning for the electrochemical activity measurement. Lift mode AFM-SECM is particularly useful to interrogate conductive surfaces, because the tip-substrate short circuit is avoided during the electrochemical measurements<sup>72</sup>.

Alternatively, constant-distance AFM-SECM imaging can also be realized by a tapping mode AFM-SECM<sup>132-134</sup>. This mode imposes a surface-induced damping of a small oscillation to the cantilever to control the tip-to-substrate distance, and then a constant tip-substrate distance can be enabled by a feedback loop which coordinates the vertical position of the probe tip to keep damping at a preset value. In contrast to the lift mode, tapping mode offers the benefit of acquiring both topography and current information simultaneously in one single scanning. Tapping mode AFM-SECM is most

useful for imaging soft samples such as hydrophilic polymers or biological specimens (e.g., microbial cells)<sup>72</sup>. However, this mode relies on mechanical resonance and therefore is sensitive to working environment of the probe. In some recent examples, the evolved tapping mode, Peakforce tapping, has also been explored in many AFM-SECM platforms for physical and structural properties studies<sup>135</sup>. During the Peakforce tapping imaging, the AFM probe is sinusoidally modulated at a low frequency (normally 0.25-2.0 kHz) which is off resonance from the cantilever oscillation. The recorded force curves can provide various information, including energy, tip-sample adhesion force, deformation, and Young's modulus.

**1.4.2.3 AFM-SECM Probes Design.** The major challenge for high quality AFM-SECM characterization experiments are predominantly determined by availability, reproducibility, and integrity of the dedicated dual functional probes<sup>72</sup>. First, a nanoscale electrode with well-defined electroactive area must be fabricated. More importantly, since the AFM-SECM experiments are performed in a solution containing redox mediators, perfect insulation of the electrical conducting part from the sub-micro sized or nanosized electroactive area must be established to avoid unfavorable current leakage.

The commercial AFM-SECM probes have not been available until recently, therefore the majority of the AFM-SECM probes reported so far were self-designed and fabricated. The AFM-SECM probes in these reports have different geometries, such as needles<sup>136</sup>, cones<sup>137</sup>,

nanowires<sup>138</sup>, pyramidal<sup>139</sup>, and recessed frame (first by Kranz et al.<sup>140</sup>), and the probe design strategies can be classified into two groups: (a) electrodes located directly at the apex of the AFM tip<sup>141, 142</sup> (see **Table 1.4**), or (b) located at a certain distance (dependent on the active electrode size) from the nonconductive tip apex<sup>140, 143, 144</sup> (see **Table 1.5**). The design of locating the electrode recessed from the tip apex enables constant-distance SECM imaging when operated at AFM contact mode, thereby avoiding short-circuits between the electrode and conducting sample surface as well as less surface fouling of the electrode. Alternatively, the design of locating electrode at the probe apex is more straightforward and creates real nanoscale electrode-surface distances for effective acquisition of both the electrochemical and topographical information at the exact same location of the sample surface. One should note that the probes of this configuration are not applicable for characterizing conducting samples in AFM contact mode, in which case direct tip-substrate short-circuits may occur.

The AFM-SECM probes can also be classified by fabrication methods, including (a) the ones fabricated by etching and insulating a conductive wire<sup>145</sup>, or (b) the ones by state-of-the-art microfabrication techniques (e.g., focused ion beam milling<sup>146, 147</sup>, electron beam lithography<sup>131</sup>, standard deposition<sup>72</sup>) for defined geometry under high reproducibility<sup>148</sup>. More details about the fabrication methods have been summarized elsewhere<sup>72</sup>.

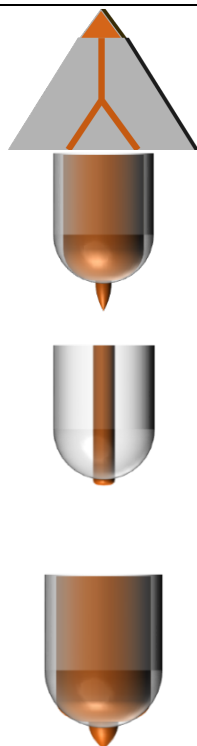
To assist the AFM-SECM probe design and fabrication, theoretical simulation of the mass transportations near the probe surface were established to analyze the resulting current responses (as shown in **Table 1.6**). Two numerical methods, namely, the finite element and the

boundary element methods, have commonly been used based on different probe geometries. The finite element method is particularly useful for electrochemistry models which involve complex geometries and boundary conditions. For example, Macpherson et al.<sup>149</sup> reported the batch microfabrication of a triangular-shaped electrode at the apex of AFM-SECM by direct write electron beam lithography. They used finite element model to simulate diffusional mass transport to the triangular electrode in bulk solution. The simulated limiting currents correlated well with the experimental results observed in steady-state voltametric measurements of the  $\text{Ru}(\text{NH}_3)_6^{3+}$  reduction in aqueous solution. Similarly, Denuault et al.<sup>150</sup> used the finite element method to predict the amperometric response of conical AFM-SECM electrodes, and calculated the steady state limiting current as a function of cone aspect ratio and insulation sheath thickness. Alternatively, the boundary element method offers the benefits of simpler implementation, reduced simulation time<sup>151</sup>, and is more favorable for 3D simulation of asymmetric AFM-SECM probes. For example, Kranz et al.<sup>152</sup> used the boundary element method to build a model for a frame-shaped AFM-SECM probe, and the simulated feedback current image well matched the experimentally measured current at the combined probe.



**Table 1.4** Summary of AFM-SECM Probe with Protruding Electrode





Fabrication method	Example scheme *	Tip/Electrode material	Electrode shape	Insulation material	Examples
Micro fabricated	Electron beam	Gold	Triangular	Silicon nitride	131, 153
	Photolithography	Platinum	Conical	Silicon dioxide	137
	Focused ion beam	Platinum/Platinum carbon composite	Disc/Conical	Silicon dioxide/ Parylene C	146, 154, 155
Bench-top fabricated	Chemically etched	Platinum/Gold	Conical	Electrophoretic paint	76

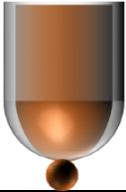


**Table 1.4** Summary of AFM-SECM Probe with Protruding Electrode

Fabrication method	Example scheme *	Tip/Electrode material	Electrode shape	Insulation material	Examples
Spark etched		Gold	Spherical/ Conical	Electrophoretic paint	132, 145

**Table 1.5** Summary of AFM-SECM Probes with Recessed Electrode

Fabrication method	Scheme *	Electrode material	Electrode shape	Insulation material	Examples
Focused ion beam		Gold/ Boron-doped diamond	Frame	Silicon nitride /Parylene C	140, 148, 156, 157
		Platinum/Gold	Recessed disc	Epoxy/Silicon nitride/Silicon dioxide	158, 159
		Gold	Nano-disc	Parylene C	160
Batch microfabricated		Boron-doped diamond	Ring	Parylene-C/Silicon nitride/ Intrinsic diamond	143, 161
		Platinum	Ring	Silicon dioxide	162, 163

**Table 1.6** Summary of Simulation Method for AFM-SECM Probe Response

<b>Simulation method</b>	<b>Electrode shape</b>	<b>Example</b>
Finite element method	Triangular	149
	Conical	150
	Conical	164
Boundary element method	Frame-shaped recessed electrode	152
	A variety of shapes	139

### **1.4.3. AFM-SECM Applications**

Nearly two decades after the first demonstration of AFM-SECM, the technique has shown remarkable successes for a variety of applications. **Table 1.7** summarizes the diverse applications which were categorized into material science, life science, as well as chemical science. Each category of applications is briefly elaborated with representative examples or case studies in the following subsections.

**Table 1.7** Summary of AFM-SECM Application

Year	AFM-SECM Mode	Application	Tip	Substrate	Electrolyte	Ref
<b>In Material Science</b>						
2002	Generation/collection -Contact	Characterizing Pt deposition on Ti/TiO <sub>2</sub> surface (surface activity of electrodes)	Fabricated: Silicon nitride probe with Pt wire-mounted tip	Ti/TiO <sub>2</sub> anode	10mM IrCl <sub>6</sub> <sup>3-</sup> and 0.5 M KNO <sub>3</sub>	165
2004	Self-named	Probing individual (gold) nanoparticles/nanoarrays/mo	Fabricated: Silicon nitride probe with Au wire-glued tip	Gold surface assembled with 11-amino-1-undecanethiol/ Silicon/	0.1 M citrate buffer/1 M NaClO <sub>4</sub>	166- 171
2017	feedback-Tapping )	nolayer labeled with redox ferrocene-polyethylene glycol (Fc-PEG) coating.				
2009	N.A.-Non-contact	Electrografting of vinylic monomers on gold surface	Fabricated: AFM probe with Pt-wire mounted tip	Glass plates coated with Cr/Au	0.7M acrylic acid and 0.25M H <sub>2</sub> SO <sub>4</sub>	172
2009	Self-named Tarm (N.A.-Tapping)	Imaging nano-patterned/structured surface	Fabricated: Gold tip tethered with ferrocene-polyethylene glycol (Fc-PEG) chains	Highly oriented pyrolytic graphite (HOPG)/Gold band electrodes on SiO <sub>2</sub>	1 M NaClO <sub>4</sub>	173, 174
2016	Feedback-Peakforce Tapping (PFT)	Characterizing gold electrode sealed/patterned in glass/ soft polymer	Fabricated silicon nitride probes with Ti/Au coated tip	Glass/polydimethyls iloxane	2.5~5 mM Fc(MeOH) <sub>2</sub> and 0.1 M KCl	147
2017	Unknown- PFT&lift	Imaging for Pt/p <sup>+</sup> -Si and Pt/p-Si electrodes	Commercial probes	Silicon substrate	0.1m KCl and 10 mM [Ru(NH <sub>3</sub> ) <sub>6</sub> ] <sup>3+</sup>	175
2018	Generation/collection - and Direct-Non-	Catalytic current mapping of oxygen reduction on Fe or Pt particles	AFM SiO <sub>2</sub> tip embedded with Pt wire	Fe-N-HOPG	O <sub>2</sub> saturated 0.1 M HClO <sub>4</sub>	176- 178
2019	contact					

**Table 1.7** Summary of AFM-SECM Application

Year	AFM-SECM Mode	Application	Tip	Substrate	Electrolyte	Ref
<b>In Chemical Process</b>						
2000	Feedback-Contact	Probing diffusional transport of electroactive species across polycarbonate ultrafiltration membranes	Fabricated: Silicon nitride probe with Pt wire-mounted tip	Membrane on glass disc	10mM $\text{IrCl}_6^{3-}$ and 0.5 M KCl	76
2002	Not mentioned-Contact	Imaging of diffusion through single nanoscale pores	Fabricated: Silicon nitride probe with Pt-coated tip	Polycarbonate membrane	10mM $\text{IrCl}_6^{3-}$ and 0.5 M $\text{KNO}_3$	179
2003	Generation/collection-Contact	Observing of dissolution from calcite crystal in aqueous solution	Fabricated: Silicon nitride probe with Pt-coated tip	Calcite crystal	5 mM $[\text{Fe}(\text{CN})_6]^{4-}$ in 0.5 M KCl	180
2005	Generation/collection-Contact (lift)	Investigating localized corrosion of Al alloys	Commercial probe: AFM tip besides a core Pt-wire electrode	Al alloy	KI and 10mM NaCl	158
2008	Generation/collection-Contact	Analyzing localized corrosion of EN AW-3003 alloy	Commercial probe: AFM tip besides a core Pt-wire electrode	Alloy sample	5 mM KI or 2 mM $[\text{Fe}(\text{CN})_6]^{4-}$ in 10 mM NaCl	181
2015	Generation/collection-Contact	Visualizing pit corrosion on iron surface	Fabricated silicon nitride probes with Au coated tip	Iron	0.1 M $\text{NaNO}_2$ and 0.5 M NaCl	182, 183
2016	Generation/collection-Contact	Imaging of copper corrosion in acidic chloride solution	Fabricated silicon nitride probes with Au coated tip	Copper nanoparticles on gold/bulk copper	10 mM $\text{CuSO}_4/50$ mM $\text{H}_2\text{SO}_4$ and 0.5 M NaCl	184, 185
2017						

**Table 1.7** Summary of AFM-SECM Application

Year	AFM-SECM Mode	Application	Tip	Substrate	Electrolyte	Ref
<b>In Life Science</b>						
2003	Generation/collection -tapping	Imaging of enzyme activity (glucose oxidase)	Fabricated: Silicon nitride probe with Au-coated tip	Gold coated silicone wafer	Phosphate buffer (pH 7.4)	133
2004	Generation/collection -contact	Imaging of enzyme activity (peroxidase)	Fabricated: Silicon nitride probe with Au-coated tip	gold/silicon nitride substrate coated by cystaminium dichloride HOPG	Phosphate buffer (pH 7.0) with 2.5% glutaraldehyde 5 mM $[\text{Fe}(\text{CN})_6]^{4-}$ $^{3-}$ in 50 mM KCl	186
2004	Generation/collection -Dynamic(similar with tapping)	Measuring glucose oxidase biosensor surface	Fabricated: Silicon nitride probe with Au- coating, back glued with a magnetic microbead			187
2005	Generation/collection -contact	Imaging of molecular (glucose) membrane transport	Fabricated: Silicon nitride probe with Au- coated tip	Polycarbonate membrane	Phosphate buffer (pH 7.4)	188
2007 - 2019	Mt	Imaging DNA chains, proteins (antigens) and viral particles marked with Fc- PEG coating	Fabricated: Silicon nitride probe with Au wire-glued tip	HOPG, mica and gold surface	Phosphate buffer (pH 8)	189- 193
2008	Feedback-Contact	Imaging of reconstituted or native biological membrane	Fabricated: Silicon nitride probe with Pt embedded tip	HOPG, MoS <sub>2</sub> , template stripped Au, and template stripped Pt	$[\text{Ru}(\text{NH}_3)_6]^{3+/2+}$	194
2008	N.A.-Contact	Triggering proteins patterning on glass slides	Fabricated: commercial PtIr- coated AFM probe with a lead wire soldered and Ti coated	Quartz glass coated with PEI and heparin	25 mM Kbr and 0.1M phosphate buffer (pH 7.4)	195



**Table 1.7** Summary of AFM-SECM Application

<b>Year</b>	<b>AFM-SECM Mode</b>	<b>Application</b>	<b>Tip</b>	<b>Substrate</b>	<b>Electrolyte</b>	<b>Ref</b>
<b>In Life Science</b>						
2009	N.A.-Contact	Directing cell growth along fibronectin patterning	Fabricated: commercial PtIr-coated AFM probe with a lead wire soldered and Ti coated	Quartz glass coated with PEI and heparin (or albumin)	25 mM Kbr and 0.1M phosphate buffer (pH 7.4)	<sup>196</sup>
2016	Not mentioned	Probing interface between living cell and polymer	Fabricated: Silicon nitride probe with Au-coated colloid glued tip.	Polymer coated gold substrate	10 mM [Ru(NH <sub>3</sub> ) <sub>6</sub> ] <sup>3+</sup> and 0.1m KCl	<sup>197</sup>

**1.4.3.1 Applications in Material Science.** AFM-SECM has been demonstrated as a powerful tool in material science for imaging composite material surfaces exhibiting electrochemically active sites, such as dimensionally stable anodes <sup>167</sup>, noble metal nanoparticles <sup>166</sup>, functionalized electrodes <sup>175</sup>, and soft electronic devices <sup>147</sup>. AFM-SECM enables the identification of these active sites individually from the morphology image whilst measuring their electroactivity from the current image.

#### *1.4.3.1.1 Noble Metal Nanoparticles*

Noble metal nanoparticles (either in the form of nanostructures on surfaces or isolated objects) have attracted increasing research interests because their ease of functionalization by self-assembling of bio or organic functional layers onto their surfaces. Characterization of the chemical and physical properties of these materials is essential to understand their fundamental mechanisms in targeted applications. Conventionally, such a characterization was performed using approaches such as cyclic voltammetry <sup>57, 198</sup>, electrochemical impedance spectroscopy <sup>59</sup>, electrochemical noise methods <sup>60</sup>, and that only provide average properties of the samples, but failed to unravel the disparity of the properties which may exhibit unique individual characteristics. Demaille et al. successfully utilized AFM-SECM to simultaneously measure the electrochemical and topographic properties of a serial of gold nanoparticle/nanodots based substrate surfaces <sup>166-172</sup>. For example, individual gold nanoparticles (~20 nm) functionalized with redox-labelled polyethylene glycol (PEG) chains (a molecular layer of nanometer-sized PEG chains end-labelled by a redox ferrocene group) were imaged by AFM-SECM <sup>166</sup>. The individual nanoparticles position and their sizes were resolved, while the electrochemical activity of the grafted redox-PEG chains were simultaneously imaged (as shown in **Figure 1.2a**). Moreover, the

dual measurements of the current response and the size of individual nanoparticles enabled determination and correlation of the statistical distribution of the PEG grafting density on the gold nanoparticles to the nanoparticle diameters. In a recent example, the same group designed an electrochemically readable molecular nanoarray platform by combining the AFM-SECM with dense nanodot arrays <sup>167</sup>. Molecular assays have evolved to be a universal tool for a wide range of applications, especially in genomics and proteomics. They first prepared a molecular nanoarray by grafting ferrocene (Fc) labelled PEG disulfide chains onto a high density nanoarray of single grained gold nanodots (created by a high-speed electron beam lithography-based process). Then, they evidenced that the AFM-SECM can electrochemically interrogate several hundreds of individual nanodots in a single image acquisition (**Figure 1.2b**).

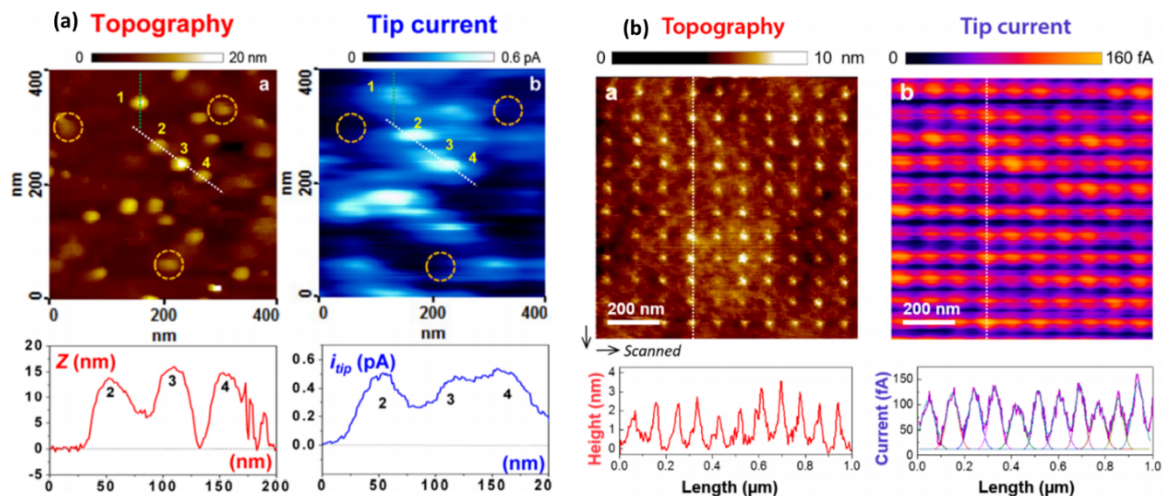


**Figure 1.2** (a) Topography and current images of a gold surface bearing a high-density random array of  $\sim 20$  nm Fc-PEGylated gold nanoparticles by AFM-SECM. (b) Simultaneously recorded topography and tip current images of a gold nanodot array. A vertical white dotted line is shown to indicate cross sections of the images taken along the column of nanodots.

Source: The figures are adapted from Ref. <sup>166</sup> Copyright (2013) American Chemical Society and Ref. <sup>167</sup> Copyright (2017) American Chemical Society

#### 1.4.3.1.2 Electrode Interface

AFM-SECM may play an important role in energy-related studies, such as investigations of electrode/electrolyte interfaces <sup>199-201</sup>, degradation, anodes and cathodes passivation <sup>202, 203</sup>. For example, photoelectrochemical water-splitting (PEC) is a promising technology to reduce greenhouse gas emission in which hydrogen is generated from water using sunlight and specialized semiconducting photoelectrodes. In a typical PEC system, catalysts for water splitting half-reactions are placed in electrical contact with the photoelectrodes, and the contacting interface is required to provide sufficient mechanical catalyst attachment to the surface and efficient pathway for charge flows. Brunshwig et al. investigated the mechanical and electrical properties of individual electrolessly deposited Pt-NPs on Si(111) surfaces via AFM-SECM <sup>175</sup>. As shown in **Figure 1.3**, both Peakforce tapping and

lift modes were run in the measurement, and topography (**Figure 1.3a**), tip-contact current (**Figure 1.3b**) and electrochemical current (**Figure 1.3c**) were correlated simultaneously to allow comparison between different Pt NPs.

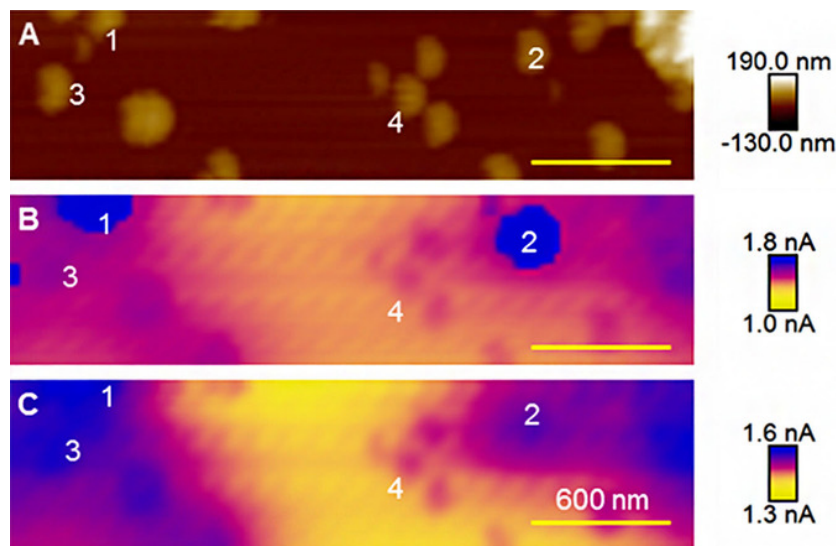


**Figure 1.3** AFM-SECM imaging of Pt nanoparticles electrolessly deposited onto  $p^+$ -Si substrate: (a) Surface topography. (b) Tip-contact current captured during the main scan. (c) Electrochemical current captured during the following lift scan.

*Source: The figure is reprinted from Ref. <sup>175</sup> with copyright permission.*

Elasticity mismatch is a critical factor for the durability of the soft electronic devices for biosensor transducer, selective drug-delivery, or neural implants. Therefore, the nanomechanical properties characterization is crucial for high performance soft electronic device design. Kranz et al. <sup>147</sup> combined the AFM with SECM in a Peakforce tapping mode to simultaneously mapping electrochemical, nanomechanical as well as topographical informations of gold microelectrodes and gold electrodes patterned polydimethylsiloxane. The AFM-SECM probes were self-fabricated from silicon nitride probes, which were further modified with a Ti/Au coating before insulated with mixed

silicon dioxide/silicon nitride layers. As evidenced in **Figure 1.4**, 3D topography, faradaic current and tip-sample adhesion images of a soft gold ultramicroelectrode were successfully acquired in a single AFM-SECM measurement.

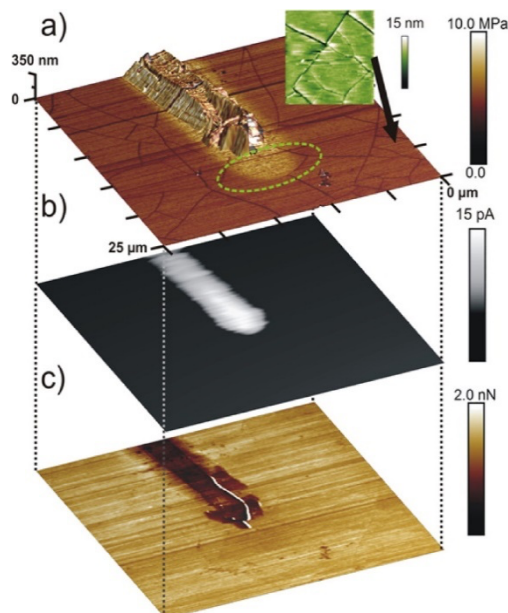


**Figure 1.4** AFM-SECM imaging of a gold electrode patterned onto a polydimethylsiloxane substrate. (a) 3D topography of the structure overlaid with Young's modulus; (b) Tip-current image; and (c) tip-sample adhesion image.

*Source: The figure is reprinted with from Ref. <sup>147</sup> Copyright (2016) American Chemical Society.*

### 1.4.3.2 Applications in Life Science.

Processes in life sciences are often associated with diffusional processes and redox chemistry. Conventional SECM has been a popular characterization tool for complex samples (e.g., cells, tissues and bacteria) <sup>204, 205</sup>. Therefore, undoubtedly, AFM-SECM also offers unparalleled capabilities for nanoscale imaging in life science research. For instance, AFM-SECM could not only release the

structural and mechanical properties, but also investigate the real-time protein-protein interactions.

#### *1.4.3.2.1 Catalytic Activity of Enzymes*

Early applications of AFM-SECM in the life science field were usually investigations of enzyme activity on surfaces, which is conventionally measured by SECM. Compared to SECM, AFM-SECM substantially increases the imaging resolution from a micrometer scale to a nanometer scale and even single molecule resolution. Simultaneous contact and tapping mode imaging of immobilized enzyme samples was first demonstrated a decade ago by Kranz et al. (**Figure 1.5**)<sup>133, 186</sup>. For example, they simultaneously acquired the topographical and electrochemical properties of glucose oxidase in a soft polymer matrix using the tapping mode of AFM-SECM (**Figure 1.5a**). The AFM-SECM probe was fabricated using micromachining techniques by coating a 100 nm thick gold layer on a conventional Si<sub>3</sub>N<sub>4</sub> cantilevers and subsequently insulated with a xylylene polymer layer (700 nm thickness). Negligible current was recorded when no glucose was added in the solution (**Figure 1.5a3**), indicative of no enzymatic activity. In contrast, an increased current was observed in the presence of glucose (**Figure 1.5a6**), which was attributed to the localized formation of H<sub>2</sub>O<sub>2</sub> when the tip scanned across the polymer matrix containing glucose oxidase. The current image provided the current intensity and distribution at different glucose oxidase locations, which corresponded well to the polymer pattern in the topographical image. In another example, they utilized the same AFM-SECM probe to study peroxidase activity immobilized on a protein gel spots. Similarly, no observable current was recorded in absence of the substrate (H<sub>2</sub>O<sub>2</sub>) in the solution because no enzymatic reaction occurred (**Figure 1.5b2**). However, periodical patterns in the current

image (**Figure 1.5b4**) with the addition of substrate revealed the changes of enzyme activity as result of the conversion of an enzymatic byproduct (ferrocinium methylhydroxide), and the measured patterns correlated well with the protein gel spots displayed in topographical image (**Figure 1.5b3**).

Enzyme activity measurement was also reported by Hirata et al. on glucose oxidase-based biosensor surface<sup>187</sup>. The AFM-SECM probe was prepared by first coating gold film on a commercial AFM probe and then isolating with a photoresist layer. An enzyme electrode was prepared on a polyelectrolyte thin film by successive layers of glucose oxidase/polystyrene sulfonate/poly-L-lysine on a HOPG surface. A dynamic force microscopy technique with magnetic field excitation was used to operate the AFM-SECM probe for precise probe positioning. Topography and oxidation current profiles of the enzyme electrode surface was successfully obtained. They also observed remarkable increase in oxidation current with substrate glucose addition. Moreover, the high-resolution current image revealed aggregation, grain, and membrane defect which were not identifiable in the topographical image. Both images together enabled high-resolution visualization of the biomolecular activity and analysis of the biosensing stability.



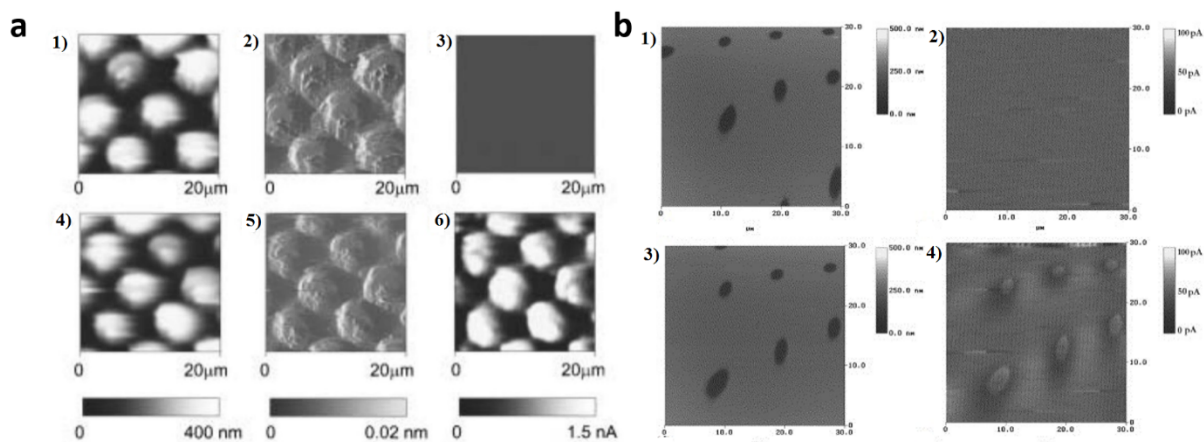


**Figure 1.5** (a) Simultaneously acquired height (first column), amplitude (middle column) and current images (last column) of the enzyme-containing periodic polymer. (b) Topography and current images of peroxidase activity.

Source: The figure is reprinted with copyright permission from Ref. <sup>133</sup> and Ref. <sup>186</sup>.

#### 1.4.3.2.2 Characterization of Cell (Membranes) and Proteins

AFM-SECM has also found increasing applications in the characterization of cells, virus, and proteins <sup>64, 206-208</sup>. For example, the interface characterization between living cells and functional scaffold substrates is the focus of a wide range of life science applications in order to understand spreading, adhesion, proliferation, migration and differentiation of cells. Higgins et al. <sup>197</sup> fabricated a polystyrene sulfonate (PPS) and poly-3,4-ethylenedioxythiophene (PEDOT) coated conductive colloidal AFM-SECM probe to measure the single cell force in mouse fibroblasts and investigated single cell interactions under different applied electric potentials. When compared to other AFM-based single cell force spectroscopy techniques, the as-prepared AFM-SECM probe not only enabled rapid adhesion measurements at the cell-biomaterial interface on multiple cells, but also varied the polymer adhesion behavior by applying different potential biases. Moreover, spatially

resolved electrochemical information such as oxygen reduction was simultaneously obtained.

Another interesting study by Nishizawa et al. utilized AFM-SECM as a biolithography technique to electrochemically draw micro patterns of biomolecules<sup>195, 196</sup>. Precise patterning of biomolecules on a substrate surface with maintained biological functionality is crucial for a range of biological applications. This study fabricated an AFM-SECM probe by converting the tip of a commercially available AFM cantilever probe into an electrode and used a contact AFM mode to generate etching agent (hypobromous acid) at the tip for locally etching away a protein-repellent layer covered on a glass slide (**Figure 1.6**). The resultant 2~3 nm deep etched area acted as protein-adhesive sites, and promoted subsequent precise adsorption of fibronectin, and the formation of a fibronectin pattern with a diameter of 2  $\mu\text{m}$  which is one order of magnitude smaller compared to their previous results.

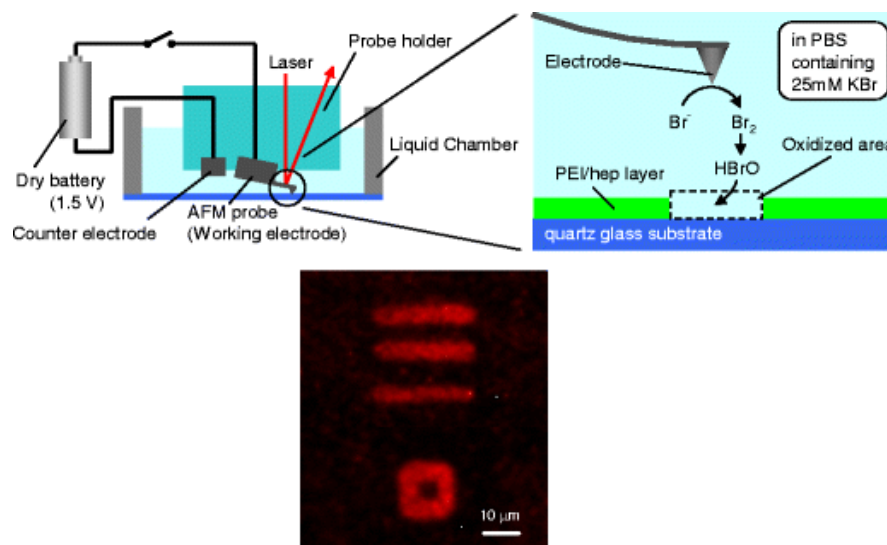


**Figure 1.6** Illustration of AFM-SECM as a biolithography technique to electrochemically draw micro patterns for protein adsorption.

Source: The figure is reprinted from Ref.<sup>195</sup> with copyright permission.

Viruses are fascinating nanomachines that have been used for applications such as nanocontainers in enzymatic catalysis and nanovectors for drug delivery<sup>190, 191</sup>. As traditional virus mapping techniques such as TEM often alter the virus structure during the characterization process, Demaille et al.<sup>190</sup> employed AFM-SECM for *in situ* mapping of the lettuce mosaic virus (LMV), a filamentous plant viruses, which was preserved in the live state during the imaging process. The virus particles were first immobilized on a gold substrate and then immunomarked with redox ferrocene (Fc)-PEG chains. Then, the tapping mode AFM-SECM was performed to acquire tip current and topography images (**Figure 1.7a**), which enabled the identification of the isolated virus particles the protein (red spots in **Figure 1.7b and c**), which was marked by redox antibodies. This study makes AFM-SECM an attractive tool for the characterization of both the topography and the redox activity of functionalized viruses at individual virus particle scale.

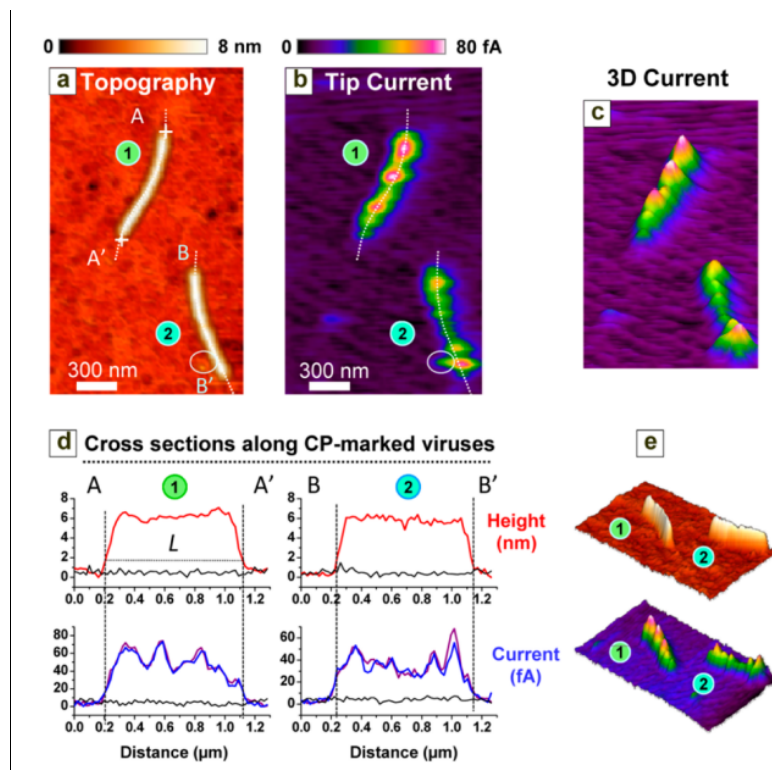


**Figure 1.7** Local AFM-SECM imaging results of coat proteins marked lettuce mosaic virus immobilized on a gold substrate. (a) topography and (b) tip current images. (c) 3D format of the tip current image which better show the string of current spots “borne” by the viruses. (d) Cross information of the topography and tip current images obtained along lines on the viruses from (a) and (b). (e) 3D titled views of the topography and tip current images.

Source: The figure is reprinted from Ref. <sup>190</sup>. Copyright (2015) American Chemical Society.

#### 1.4.3.2.3 Transportation Characterization

The characterization of molecular transport behavior through cell membrane at single-cell level remains a major challenge in cell physiology. Kranz et al. <sup>188</sup> demonstrated the utilization of AFM-SECM for high-resolution imaging of glucose transport through cellular membranes. Biological recognition element (e.g., glucose oxidase) was first immobilized onto the electrode surface of an AFM-SECM probe. This enabled the enzymatic conversion of the electroactive and inactive species formed at the sample surface by self-assembled thiol monolayers with reactive head groups. Dynamic mode of AFM and

generation/collection mode of SECM were both carried out for the imaging process. When glucose diffused through membrane pores towards an immobilized oxidase layer, the glucose was converted to gluconolactone (**Figure 1.8a**). The resulting current was measured by oxidation of an enzymatically generated by-product of  $\text{H}_2\text{O}_2$  at the AFM-SECM tip. The tip current can further be translated into an actual (local) glucose concentration experienced by the probe, simply by pre-calibrating the response of AFM probe/microsensor to glucose (**Figure 1.8b**). Simultaneous measurement of topography and current images were realized as shown in **Figure 1.8c** and **1.8d**. Furthermore, horseradish peroxidase deposited on the AFM-SECM probe surface was shown to enable simultaneous imaging of the topography of an individual micro-structured disk electrode and the local electrochemical activity.

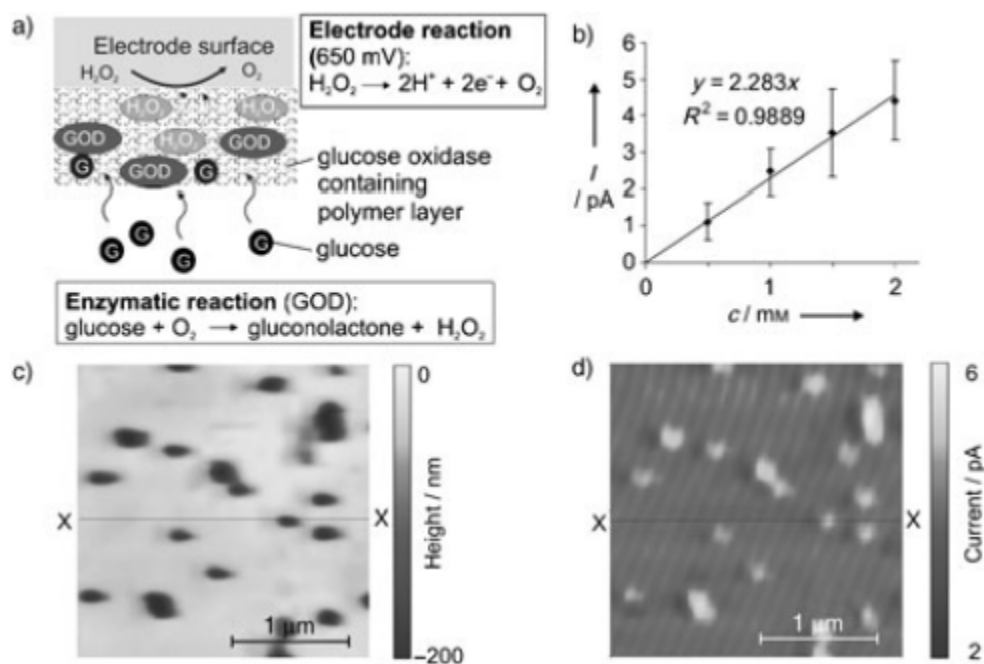


**Figure 1.8** (a) Schematic illustration of reactions for glucose detection with a glucose oxidase-based biosensor. (b) Glucose calibration of an AFM-tip-integrated biosensor. (c) Topography and (d) current images of glucose transporting through a porous polycarbonate membrane.

Source: The figure is reprinted with copyright permission from Ref. <sup>188</sup>.

**1.4.3.3 Applications in Chemical Process.** Early demonstrations of AFM-SECM focused on the study of crystal dissolution processes such as calcite<sup>180</sup>, or potassium ferrocyanide trihydrate crystals<sup>76</sup>. Fundamental understandings of crystallization or dissolution processes occurring at liquid/solid interfaces are of key importance for a wide range of chemical reactions. Macpherson et al.<sup>180</sup> proposed an attractive approach to study the initial stage of a dissolution process by applying a controlled transient perturbation to the solution and then record the resulting topography variations before and after the perturbation. For example, KBr crystal dissolution in a KBr saturated acetonitrile solution was electrochemically induced through oxidation of bromide to tribromide, which perturbs a dynamic dissolution/growth equilibrium at the crystal/solution interface. The tip current was recorded in the SECM configuration as a function of tip-substrate distance and time to determine the dissolution rate, while *in situ* topographical measurements by the electrochemically active AFM tip (operated in contact mode) permitted the identification of structural changes that accompany the dissolution process. Though only a topographical image was obtained, without electrochemical current images this work demonstrated the ability of AFM-SECM to induce and visualize surface dissolution reactions and to measure the corresponding kinetics.

Characterization of surface corrosion is also another application area of AFM-SECM for chemical processes<sup>158, 181-185</sup>. Gaining fundamental insight into corrosion processes requires spatially resolved information on morphological changes associated with electrochemical processes occurring at the metal/liquid interface. For example, copper is a widely used metallic material with extensive application in heat exchangers or electronics. The metal copper has excellent resistance towards corrosion even when

exposed to high moisture environment due to formation of patina of multi-layered oxides on its surface. However, local degradation may still occur on this passive layer when presented in chloride containing environments, particularly under acidic conditions. Therefore, the study of copper corrosion process is significant in material sciences to better predict and prevent its degradation. Kranz et al.<sup>185</sup> used AFM-SECM to monitor surface corrosion of pure copper in acidic chloride solution. They fabricated a recessed AFM-SECM probe by modifying a commercial silicon nitride cantilever with a layer of sputtered gold and then depositing a silicon nitride layer through chemical vapor deposition. Generation/collection mode was used for SECM imaging, and contact mode for AFM imaging. The release of  $\text{Cu}^{2+}$  ions was recorded via electrochemical reduction and collection of the metal ions on the conductive frame of the AFM-SECM probe. Simultaneous detection of the topographical changes resulting from the corrosion process enabled the distinction and correlation of local passivation and pitting phenomena.

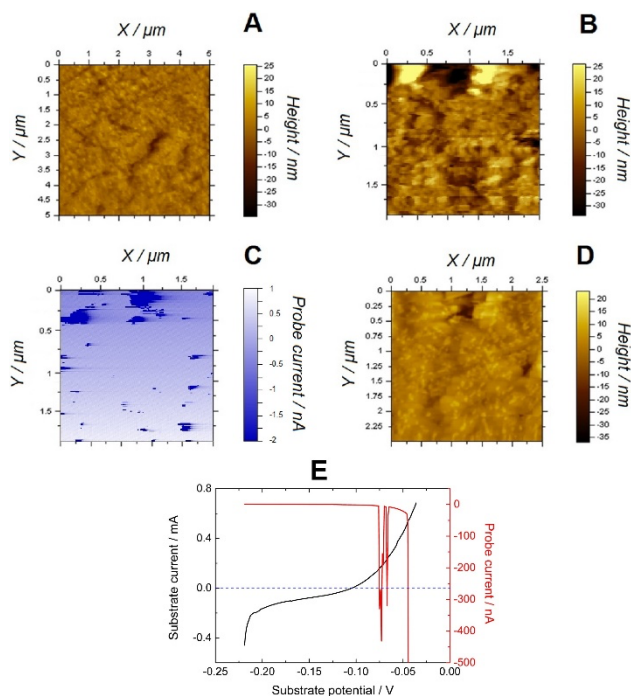


**Figure 1.9** (a,b,d) Topography and (c) current images recorded by AFM-SECM at different scanning dimensions, (e) Current response of AFM-SECM probe (red line, right axis) and copper substrate (black line, left axis).

Source: The figure is reprinted with copyright permission from Ref. <sup>185</sup>.

#### 1.4.4 Summary and Outlook on AFM-SECM Technique

The present literature review has provided an overview on the latest research progress of AFM-SECM, including AFM-SECM principles, probe design, operation modes, as well as applications in various disciplines or fields. Obviously, after nearly 20 years of the first successful demonstration of AFM-SECM, this hybrid technique has fulfilled its initial promise of simultaneous topography and electrochemistry imaging and continue to show its exciting potentials in emerging applications. However, AFM-SECM has still be considered as a highly specialized techniques and only applied by a small research community. Some notable challenges of AFM-SECM should be addressed to realize its full potentials.



The first major challenge lies in the cost, reliability and durability of the combined AFM-SECM probes. Though the combined probe is essentially an AFM probe with ultramicroelectrode incorporated at or close to its tip, the fabrication process is complex, time-consuming, and require sophisticated microprocessing equipment. The majority of the AFM-SECM probes reported so far are self-designed/fabricated and their reliability and durability are often limited or poorly characterized or tested. Commercial probes have become available only recently, but the cost and durability are still significantly more than standard SECM or AFM probes. It can be expected that further development of microprocessing techniques will greatly assist the mass production of AFM-SECM probes with low cost, excellent reliability and long lifetime, thereby encouraging more researchers to use AFM-SECM.

Another challenge is the further advancement of the AFM-SECM imaging resolution. Despite enhanced-spatial-resolution imaging capability has been achieved by the sharpened probe tip, the characterization images from AFM-SECM are still far from revealing the ultimate single molecule resolution or information. For example, though submicron scale imaging of local enzyme activity has been demonstrated<sup>133, 186</sup>, the local enzyme spots imagined by AFM-SECM still represented a large number of enzyme molecules instead of single enzyme molecular. Further probe miniaturization may help increase the AFM-SECM imaging resolution, and thus is expected to reveal more accurate individual properties of the nanosystem.

Finally, as evidenced in Subsection 1.4.2.3, only a few studies have dedicated to the theoretical simulation of the AFM-SECM probe current response, likely due to the more complex geometry of the AFM-SECM probes compared to conventional SECM

probes. The conventional SECM probe simulations have been mostly performed in an axisymmetric 2D space <sup>152</sup> using theoretical models of finite difference method <sup>209</sup>, finite element method <sup>210</sup>, or boundary element method <sup>211</sup>. Apparently, more research efforts should be devoted to the modeling of the AFM-SECM probes to provide better guidance to a robust AFM-SECM probe design and fabrication.

## CHAPTER 2

### COLLOIDAL CHEMISTRY AND CONTACT MECHANICS ANALYSIS OF REACTIVE NANOBUBBLES

Chapter 2 employed the injection of high-pressure gases through a hydrophobized ceramic membrane to produce different gaseous NBs (e.g., N<sub>2</sub>, O<sub>2</sub>, H<sub>2</sub> and CO<sub>2</sub>) in water, which is different from cavitation bubbles with potential internal low pressure and non-condensed gases. The results indicate that increasing the injection gas pressure (60–80 psi) and solution temperatures (6–40 °C) both reduced bubble sizes from approximately 400 to 200 nm, which are validated by two independent models developed from the Young-Laplace equation and contact mechanics. Moreover, the colloidal force model can also explain the effects of surface tension and surface charge repulsion on bubble sizes or internal pressures. The contact mechanics model incorporates the measurement of the tip-bubble interaction forces by atomic force microscope (AFM) and reveals the internal pressures and the hardness of NBs (e.g., Young's modulus) that vary slightly with the types of NBs. Both colloidal force balance model and our contact mechanics model yielded consistent prediction of the internal pressures of various NBs (120 psi-240 psi). The developed methods and model framework will be useful to unravel properties of NBs and support engineering applications of NBs (e.g., aeration or ozonation).

#### 2.1 Background and Challenges

##### 2.1.1 Properties and Applications of NBs

Micro/nanobubbles (MNBs) are ultra-small or ultrafine gas bubbles in diameter of <1 μm in liquid.<sup>212</sup> MNBs can be generated in many processes such as spiral-liquid-flow,<sup>213</sup>

venture tube nozzles,<sup>214</sup> cyclic pressurization and depressurization,<sup>6</sup> ejector type generator,<sup>215</sup> porous membrane generator<sup>212, 216</sup> and electrolytic generation.<sup>217, 218</sup> Specifically, NBs present unique characteristics that bulk bubbles (macro-bubbles) do not have, primarily including a high specific area (surface area per volume) and a long residence time in water due to their low buoyancy and high stability against coalesces, collapse or burst.<sup>219</sup> NBs have a higher efficiency of mass transfer compared to bulk scale bubbles due to the high specific surface areas.<sup>7, 8</sup> The high specific surface also facilitates physical adsorption and chemical reactions in the gas liquid interface. The collapse of NBs creates shock waves, which in turn, promotes the formation of hydroxyl radicals ( $\bullet\text{OH}$ ), a highly reactive oxidant that non-specifically reacts with and decomposes organic matters.<sup>14-16</sup>

MNBs have proven useful in many industrial and engineering applications, ranging from emulsion technology for chemical processing, pharmaceutical manufacturing, detergent-free cleaning,<sup>218</sup> water aeration,<sup>2</sup> ultra-sound imaging,<sup>220</sup> intracellular drug delivery,<sup>9</sup> mineral flotation,<sup>221</sup> water and wastewater treatment<sup>222, 223</sup> to seed germination and plant growth.<sup>47-49, 212</sup> For example, ozonation in water has strong antimicrobial effects against bacteria, fungi, protozoa, and viruses,<sup>224</sup> and has broad applications in pharmaceutical,<sup>225</sup> food,<sup>226, 227</sup> cosmetic<sup>228</sup> and medical fields.<sup>229, 230</sup> However, dissolved ozone concentrations in liquid reduce rapidly since it decays fast with a half-life time of approximately 20 min, especially at higher temperatures. Also, ozone is about 12 times less soluble in water than chlorine, which limits its comparative effectiveness at equivalent doses against target pollutants, such as persistent bacterial spores or cysts. By contrast, ozone NBs have significantly higher stability compared to regular dissolved ozone. The

increased hydraulic retention time permits the controllable release of ozone molecules and ensure stable dissolved ozone concentrations for reactions or antibacterial activity. Additionally, bacteria inactivation and removal by ozone or other NBs can also be attributed to the formation of hydroxyl radicals or other reactive species especially during collapse or burst.<sup>231</sup> Bacterial removal can be improved by the burst of high intensity number and smaller size of bubbles near the water surface in the bacterial suspension.<sup>232</sup> Ozone microbubbles caused 99.99% inactivation of *E. coli* cells with a lower ozone dose than bulk ozone bubbles.<sup>233, 234</sup> In addition, ozone MBs are effective against other types of bacteria such as *Bacillus subtilis* spores and *Cryptosporidium parvum*.<sup>231</sup> Furthermore, combinations of NBs with UV irradiation or ultrasonication may boost up radical formation and improve disinfection power of NBs.<sup>8, 235, 236</sup>

### **2.1.2 Colloidal Stability and Its Contributions from Mechanical Properties of NBs**

Colloidal stability of bulk NBs in liquids usually refers to the longevity of stable bubble sizes and size distribution, which is reported vary from a few hours to days or even months.<sup>237, 238</sup> It still remains largely debatable in the scientific community whether and how NBs are stabilized in liquids, despite that many theories were proposed such as the interplay of internal gaseous pressure and surface tension.<sup>239</sup> Surface tension is a strong localized stress parallel to the liquid/air interface, where the cohesive attraction force between liquid molecules is greater than the adhesive force between air molecules.<sup>239</sup> According to the Young-Laplace equation,<sup>237</sup> NBs with a radius of 200 nm may have an extraordinarily high internal pressure of 728 kPa. Thus, the lifetime of the bubbles is believed to be extremely short (e.g., microseconds to milliseconds<sup>240</sup>) as the high internal gas pressure should lead to instant dissolution of the gas into the bulk solution.<sup>241</sup> On the

other hand, some studies indicate that the gas pressure inside NBs may be lower than the predicted.<sup>237, 242, 243</sup>

The unusual stability of bulk NBs in liquid could be attributed to many potential factors such as surface coating,<sup>244, 245</sup> high surface zeta potentials,<sup>246, 247</sup> formation of surface barriers,<sup>248-250</sup> and high density mechanism.<sup>251, 252</sup> For example, surface adsorption of organic substances (e.g., sodium dodecyl sulfate and dodecyl tri- methyl ammonium chloride)<sup>253</sup> or other amphiphilic particles in liquid can lower the surface tension and stabilize the NBs.<sup>244</sup> According to the DLVO theory, NBs are usually negatively charged (-15~-45 mV) in water at neutral pH and thus could be stabilized due to the electrostatic repulsion between neighboring NBs.<sup>246, 247</sup> The electric double layer may also prevent the gas transfer and bubble coalescence.<sup>253, 254</sup> Moreover, the presence of anions (e.g., hydroxide ions) on the NB surface reduces surface tension of water, resulting in a lower internal pressure of NBs than the prediction by the Young-Laplace equation.<sup>237</sup> Ke Shuo et al. revealed that bulk nitrogen NBs are more stable in alkaline solutions than in water of low pH or high salinity.<sup>255</sup> The isoelectric point of the air NB surface is in a pH range of 3-4, and thus, under alkaline conditions, NBs carry greater negative charges and experience greater electrostatic repulsion, which may counteract the outbound force from the Laplace pressure inside NBs.<sup>253, 256</sup>

More recently, studies indicate that a strong hydrogen bond may form among water molecules on the surface of bulk NBs under a gas supersaturated environment.<sup>248-250</sup> This hydrogen bonded water layer acts as a tight network of “skin” that reduces the diffusivity of gas from NBs.<sup>257</sup> One interesting phenomenon is that water suspension of NBs is usually saturated or even oversaturated with the corresponding gas molecules.<sup>258, 259</sup> The

oversaturation may lead to a dynamic balance or equilibrium of the outbound and inbound diffusion fluxes of the gas. Moreover, the gas molecules trapped inside surface NBs are suspected to be highly condensed (1~3 orders of magnitude higher than that under the standard pressure and temperature) and thus may not follow the ideal gas law.<sup>260, 261</sup> Thus, the liquid/gas interface of NBs in liquid deserves systematic research to unravel unique mechanisms for their colloidal stability. Wang et al. employed the spectroscopic force measurement and observed that the surface of a NB is kinetically stable against high internal pressures and the gas-water interface has great diffusive resistance.<sup>262</sup>

### **2.1.3 Characterization of NBs**

Characterization of the unique colloidal and chemical behavior of NBs has always been challenging due to the small bubble sizes in liquid. Dynamic Light Scattering (DLS) or Laser Diffraction techniques have been used for the size distribution of bulk NBs in liquid.<sup>212, 216, 237</sup> Laser-Doppler microelectrophoresis is used to measure zeta potential,<sup>212, 216, 263</sup> while Nanoparticle Tracking Analysis (NTA) seems the only way to measure the numerical concentration or density of bulk NBs.<sup>218, 244</sup> While cryo-TEM was among the early techniques that provided visual evidence of NBs in liquid,<sup>264, 265</sup> recent work also employed atomic force microscope (AFM)<sup>255, 266</sup> and fluorescent confocal microscope to investigate the morphology of NBs in various liquids (e.g., water containing rhodamine 6G,<sup>267</sup> water containing NaCl<sup>268</sup>). Moreover, the reactivity and electrochemistry of surface NBs at the electrode surface were studied using cyclic voltammetry to analyze mechanisms of bubble nucleation, growth, and stability.<sup>269</sup>

AFM is a powerful technique to study the surfaces of soft samples such as live biological cells.<sup>1, 270, 271</sup> Intermolecular forces between probe tip and cell surface could

reveal many material properties (e.g., adhesion, cell stiffness, cell elasticity and cytoplasmic turgor pressure).<sup>1, 270</sup> For example, the Young's modulus of the studied material could be probed by AFM to indicate stiffness or elasticity based on the Derjaguin, Muller, Toropov (DMT) model. Similarly, Hooke's law was applied to determine the pressure inside the bacterium, the turgor pressure inside the bacterial cytoplasm that produces an outbound pressure and provide mechanical strength of bacterial cells.<sup>1, 270</sup> Moreover, AFM was also performed to analyze surface NBs and nanodroplets, which are distinguished by their different morphology (e.g., water/air contact angles), force curves or responses to different tip-surface interaction forces.<sup>267, 272, 273</sup> A recent study employed a sharp AFM probe (DNP-10, Bruker) with a nominal spring constant  $0.35 \text{ N}\cdot\text{m}^{-1}$  to fully penetrate a single NB and contact the highly ordered pyrolytic graphite (HOPG) substrate.<sup>261</sup> The measured adhesion force between the probe tip and the HOPG surface (0.7 pN) was smaller than that (4.6 pN) directly measured in air with the same AFM probe, which implied that the gas density of NBs near the substrate was up to 2~3 orders of magnitude higher than that under the standard pressure and temperature according to the van der Waals force theory. Shuo W. et al. used molecular simulation to discover that the gas layers of NBs near the substrate exhibited a high-density state.<sup>261, 274</sup>

Understanding colloidal stability and other properties under environmentally relevant conditions is crucial for many potential engineering applications of NBs (e.g., aeration or ozonation). This study evaluated the effects of internal gas pressure and solution temperature on bubble size distribution and mechanical properties of NBs in water. We generated different gaseous NBs in water via a hydrophobized porous ceramic membrane using compressed gases as we reported previously.<sup>275, 276</sup> Dynamic light scattering (DLS)



and AFM were used to measure the bubble sizes, zeta potential, the Young's modulus and stiffness of NBs. Furthermore, the bubble concentration were analyzed using Nanoparticle Tracking Analysis (NTA) to provide new insight into the longevity of NBs in liquid. Finally, this work employed two novel modeling approaches to analyze the bubble size dependence on internal pressures of NBs and solution temperatures, among many other parameters that could be interpreted by the models. One model was established based on the modified Laplace-Young equation that considers colloidal forces acting on the water/gas interfaces of NBs, whereas the other model was built upon the contact mechanic theories. The two model predictions have been successfully validated with experimental data and reached coherent predictions on the internal pressures of NBs.

## **2.2 Materials and Methods**

### **2.2.1 Production and Characterization of NBs in Water Under Different Injection Gas Pressures and Different Storage Temperatures**

Nitrogen nanobubbles (N<sub>2</sub> NBs), oxygen nanobubbles (O<sub>2</sub> NBs), hydrogen nanobubbles (H<sub>2</sub> NBs), and carbon dioxide nanobubbles (CO<sub>2</sub> NBs) were separately generated by injection of their compressed ultra-high purity gases (99.999%, Airgas Inc.) through a tubular ceramic membrane (140 nm pore size, MSKTB01014UM, Sterlitech, U.S) into deionized (DI) water at room temperature. The outer surface of the tubular ceramic membranes was coated with stearic acid (octadecanoic acid) as detailed elsewhere.<sup>275</sup> The gases were dispersed via the ceramic membrane into 500 mL of DI water continuously for 90 min under a flow of 0.45 L·m<sup>-1</sup> to reach stable bubble size distribution in water, as we reported previously.<sup>212</sup> The pressure of the injection gas flow was adjusted by cylinder-compatible regulators in a range between 60 psi (~414 kPa) and 80 psi (~552 kPa). To

investigate the effect of temperature on size distribution of NBs in water, O<sub>2</sub> NBs and N<sub>2</sub> NBs were generated in DI water as mentioned above and stored in sealed sample tubes as shown in **Figure 2.1** (without exposure to room light). The DI water was pre-cooled or preheated under different temperature (6°C, 20°C and 40°C). The bubble size distribution, zeta potential and bubble number concentration were measured at different times (e.g., 1-2 months).

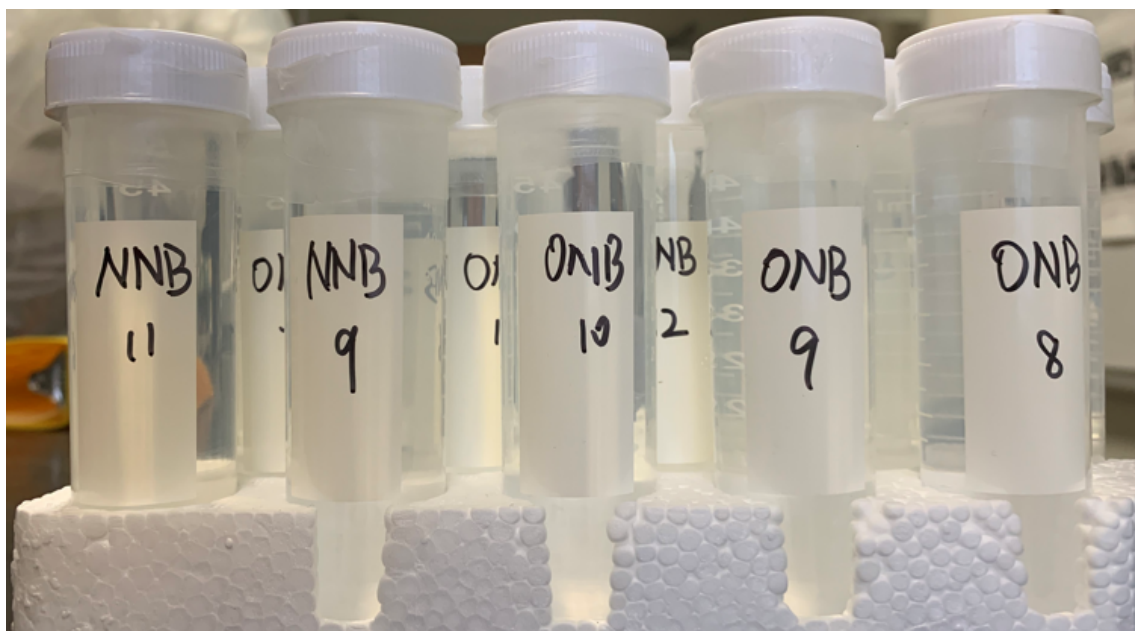


**Figure 2.1** O<sub>2</sub> NBs and N<sub>2</sub> NBs kept in sealed sample tubes.

Dynamic light scattering (DLS) on a Zetasizer Nano ZS instrument (Malvern Instruments) was used to measure the bubble size distribution of the water suspension of NBs immediately after preparation. The same Zetasizer Nano ZS instrument was used to measure the zeta potential (ZP) of NBs. Furthermore, the concentrations of NBs in water was measured by the nanoparticle tracking analysis (NTA) (NS300, NanoSight instrument) with a 532 nm laser light source.<sup>27</sup> This NTA was equipped with a 20× magnification microscope and a high-speed camera. Each result was obtained from the average of five

measurements, and each measurement was last for 60 s. The camera level was usually set at 10, the threshold was set at 30 and the solution viscosity was 1 centipoise (1 centipoise =  $10^{-2}$  P =  $10^{-3}$  Pa·s). The concentration of NBs was counted and obtained by the nanoparticle tracking analysis software (Nanosight NTA 3.2).

### 2.2.2 Modeling Analysis of Colloidal Stability of NBs in Water

According to our previous study,<sup>275</sup> the suspended or bulk NBs in water could be stabilized by the outbound and inbound pressures from a number of interfacial forces. The outbound pressure ( $P_{out}$ ) is ascribed to surface charge repulsion and internal gas pressure ( $P_{int}$ ).

$$P_{out} = \frac{\sigma^2}{2 \cdot D \cdot \epsilon_0} + P_{int} \quad (2.1)$$

Where  $D$  is the relative dielectric constant of the gas bubbles (assumed unity) and  $\sigma$  is the surface charge density ( $C \cdot m^{-2}$ ), which is calculated by the Gouy-Chapman equation when zeta potential is less than 80 mV:<sup>212</sup>

$$\sigma = \frac{\epsilon \cdot \epsilon_0}{\lambda_D} \cdot \zeta \cdot [(1+z/r)] \cdot \exp(-z/\lambda_D) \quad (2.2)$$

Where  $\epsilon_0$  is the dielectric permittivity of a vacuum,  $8.854 \times 10^{-12}$  ( $C \cdot V^{-1} \cdot m^{-1}$ ),  $\epsilon$  is the dielectric constant of water, 80.36 (20 °C),  $\zeta$  is the zeta potential of NBs (V),  $z$  is the

distance from the particle's surface to the slipping plane (0.335 nm),  $r$  is the bubble radius (nm), and  $\lambda_D$  is the Debye length (nm).<sup>275</sup>

The surface tension pressure of NBs ( $P_r$ ) exerted from the surrounding water molecules, the atmospheric pressure ( $P_0$ ), and the water head pressure ( $P_h$ ) contribute to the inbound pressure ( $P_{in}$ ):

$$P_{in} = P_r + P_0 + P_h \quad (2.3)$$

$$P_r = \frac{2 \cdot \gamma}{r} \quad (2.4)$$

$$P_h = \rho \cdot g \cdot h \quad (2.5)$$

Where  $\gamma$  is the water surface tension (72.80 mN·m<sup>-1</sup> at 20 °C),<sup>277</sup>  $r$  is the radius of NBs (m),  $g$  is the gravity acceleration (9.80 m·s<sup>-2</sup>),  $\rho$  is the density of water (kg·m<sup>-3</sup>), and  $h$  is the height of water (m). When the bulk NBs are stabilized in water (i.e.,  $P_{in} = P_{out}$ ), their radius can be related to the NB's internal pressure and other factors:

$$P_{int} = \frac{2 \cdot \gamma}{r} + (P_0 + \rho \cdot g \cdot h) - \zeta^2 \left( \frac{\varepsilon}{\lambda_D} \right)^2 \frac{\varepsilon_0}{2 \cdot D} \quad (2.6)$$

By measuring the colloidal properties such as bubble's hydrodynamic radius ( $r$ ) and zeta potential ( $\zeta$ ) of NBs, we could potentially estimate or predict the internal pressures of NBs ( $P_{int}$ ). This model equation, however, assumes that NBs are at a quasi-steady state

without significant dissolution or other forms of changes that destabilizes their sizes or internal pressures, which was achieved in our experimental condition where NBs were produced and stored in sealed gas-saturated solutions with minimum disturbances or agitation.

### **2.2.3 Visualization and Mechanical Properties Assessment of NBs in Water**

**2.2.3.1 Visualization of Surface NBs by AFM.** Silicon wafers ( $\emptyset 3''$  Silicon wafer, Type P/<111>, TED PELLA) were used as substrates to produce surface  $N_2$  and  $O_2$  NBs that were first produced in water under an injection pressure of 60 psi at 20 °C. To deposit NBs on silicon substrates, we dropped 0.15 mL of the NB water droplet onto the clean substrate surface and waited for about 10 minutes to allow the NBs to attach to the substrate surface, which was placed under the AFM instrument. We used PeakForce quantitative nanomechanical mapping (PF-QNM) on a Dimension Icon AFM instrument (Bruker, Santa Barbara, CA) with NanoScope version 9.4 software and NanoScope V to analyze the topography and mechanical properties of surface NBs in liquid. Silicon nitride cantilevers (scanasyst-fluid, Bruker) with a nominal tip radius of 20 nm and a nominal spring constant of  $0.7 \text{ N}\cdot\text{m}^{-1}$  were used to directly immerse into the droplet and sweep the surface NBs at a scanning rate of 1 Hz to avoid tip-sample interactions or induce any bubble deformation, as a bubble-height decrease was observed when the scan rate was high (e.g., 50–100 Hz).<sup>275</sup> The set point was carefully selected to yield a low loading force (500 pN) that applied to the surface NBs.<sup>237, 278</sup> The spring constant of the cantilever was calibrated via thermal

tuning after deflection sensitivity calibrated by a PF-QNM Ramp on silicon surface in water. The calibration of the spring constant was carefully performed before experiments.

**2.2.3.2 Mechanical Property Assessment of NBs in Water.** The two common contact models, Derjaguin-Muller-Toporov (DMT) and Johnson-Kendall-Roberts (JKR), are typically used to calculate the Young's modulus and stiffness of soft or deformable materials such as living cells and colloids.<sup>273, 279-283</sup> A sharp AFM probe was used to compress a local sample surface to induce the indentation ( $\delta$ ) as illustrated in Figure 2.6a<sup>284</sup> The internal pressure of the soft sample body can be calculated by Equation (2.7), where the loading force ( $F_{loading}$ ) is the compression force that the AFM probe tip exerts on the sample surface and  $a$  is the radius of the spherical contact area, which is related to the indentation ( $\delta$ ) and the AFM tip radius ( $R$ ) in Equation (2.8) according to the contact geometry shown in Figure 2.6b.  $F_{loading}$  was controlled by AFM at a level of  $500 \pm 50$  pN and  $\delta$  was directly read from the force-distance curve. Thus, the internal pressure of NBs can be calculated by the applied loading force ( $F_{loading}$ ) and the corresponding indentation ( $\delta$ ). It is worth noting that in addition to the internal gas pressure, surface tension force ( $\sim 5 \times 10^{-5}$  pN) may also contribute to the force balance with the applied loading force. However, compared to the loading force, this surface tension force is negligible. Furthermore, the Young's modulus of NBs could be calculated by Equation (2.9).<sup>285, 286</sup>

$$P_{int} = \frac{F_{loading}}{\pi \cdot a^2} \quad (2.7)$$

$$(R - \delta)^2 + a^2 = R^2 \quad (2.8)$$

$$\delta = \frac{a^2}{R} - \frac{2}{3} \sqrt{\frac{6 \cdot \pi \cdot W \cdot a}{E^*}} \quad (2.9)$$

$$F_{adh} = \frac{3 \cdot \pi \cdot R \cdot W}{2} \quad (2.10)$$

Where  $W$  is the adhesion energy per unit area ( $\text{J} \cdot \text{m}^{-2}$ ) and  $E^*$  is the reduced Young's modulus (MPa).  $W$  could be calculated by Equation (2.10) with the tip-sample adhesion force ( $F_{adh}$ ) read directly from the force-distance curve. Rearranging Equations (2.9) -(2.10) leads to Equation (2.11), which corresponds to the JKR model. By contrast, the DMT model in Equation (2.12) has a slightly different form relating the Young's modulus to the interface forces and indentation.

After the determination of the reduced Young's modulus ( $E^*$ ), the sample's Young's modulus ( $E_s$ ) was calculated by Equation (2.13), which shows that  $E^*$  is related to the Poisson's ratios ( $\nu_s$  and  $\nu_T$ ) and the Young's moduli ( $E_s$  and  $E_T$ ) of the sample and tip, respectively. Since the AFM probe has  $E_T$  of typically 160–290 GPa, which is significantly greater than that of NBs, the deformation of the tip could be neglected when engaged against the NB's surface. Thus, Equation (2.13) is simplified to allow the determination of samples'  $E_s$  with  $E^*$ .<sup>287</sup>

$$E^* = \frac{F_{adh} \cdot R \cdot \sqrt{2 \cdot R - \delta}}{9 \cdot \delta^{3/2} \cdot (R - \delta)^2} \quad (2.11)$$

$$E^* = \frac{F_{loading} + F_{adh}}{\sqrt{R \cdot \delta^3}} \quad (2.12)$$

$$E^* = \left[ \frac{3}{4} \left( \frac{1 - \nu_s^2}{E_s} + \frac{1 - \nu_T^2}{E_T} \right) \right]^{-1} \approx \left[ \frac{3}{4} \left( \frac{1 - \nu_s^2}{E_s} \right) \right]^{-1} \quad (2.13)$$

To ensure reproducibility and accuracy of the experimental results (e.g., the force-distance curves obtained from the tip-NB contact), morphological mapping of surface NBs was repeated at least three times on each sample with a scan area of  $1 \times 1 \mu\text{m}$ . Several force measurements were obtained on the center of one discrete NB surface to produce stable and reproducible values of Young's modulus and stiffness. To ensure the stability of the AFM tip during the mechanical measurement, modulus and stiffness measurements are carried out on the silicon substrate surface before each sample. The measured modulus values should have variations of less than 15%. Otherwise, the cantilever tip would be changed. We extracted all the force-distance curves and re-calculated the Young's modulus of NBs using the JKR and DMT models in Equation (2.11) and Equation (2.12). The tip-bubble contact is defined as the point when the tip experiences a significant attractive force that usually causes a jump-in peak in the force-distance curve.<sup>1</sup> The adhesion force ( $F_{adh}$ ) was obtained from the force curves, whereas other parameters with variables used in JKR or DMT model calculations include: (1) the tip of curvature ( $R$ ) is *c.a.*  $20 \pm 5 \text{ nm}$ ; (2) the



Poisson's ratio of NBs ( $\nu_s$ ) is 0.3, as typically used for soft colloids;<sup>1</sup> (3) the measured indentation ( $\delta$ ) varied slightly ( $9\pm 3$  nm) under the current loading force and was used in Equation (2.11) or (2.12) to calculate the reduced Young's modulus ( $E^*$ ) to obtain the JKR or DMT model results.

## 2.3 Results and Discussion

### 2.3.1 Effect of the Injection Gas Pressure on Bubble Size Distribution of NBs in Water

The bubble size distribution of four types of gaseous bulk NBs (**Figure 2.2**) exhibits evident dependence on the injection gas pressure changes. **Figure 2.3** further demonstrates that the average bubble size monotonously decreased with an injection gas pressure increase from 60 psi to 80 psi. For example, the average hydrodynamic diameters of O<sub>2</sub> NBs reduced from 294 nm to 199 nm after the injection gas pressure increased from 60 psi to 80 psi. The influence of injection gas pressure on NBs' size also implies that the DLS detected NBs instead of other nanomaterials or nanoparticles that should not vary in sizes with the injection gas pressure.<sup>1</sup> This dependence of bubble size on internal pressure is supported by the colloidal stability model in Equation (2.6). **Tables 2.1-2.2** summarizes the major parameters we used in the model calculation.

**Table 2.1** Parameter Values Utilized in the Colloidal Model Calculation in Equation (2.6)

Solution type	Parameters	Four different NBs			
		O <sub>2</sub>	N <sub>2</sub>	H <sub>2</sub>	CO <sub>2</sub>
DI water	Water surface tension ( $\gamma$ )		0.0728 N·m <sup>-1</sup>		
	Water head pressure (P <sub>h</sub> ), Pa		980		
	Atmospheric pressure (P <sub>0</sub> ), Pa		101325		
	Dielectric constant of water ( $\epsilon$ )		80.36 (20 °C)		
	Dielectric permittivity of a vacuum ( $\epsilon_0$ ), C·V <sup>-1</sup> ·m <sup>-1</sup>		8.854×10 <sup>-12</sup>		
	Internal pressure of NBs, Pa	The injection gas pressure in <b>Figure 2.3</b>			
	Zeta potential of NBs ( $\zeta$ ), mV	-40±5	-28±5	-20±5	-20±5

**Figure 2.3** shows the model predictions (solid and dotted lines) of bubble diameters ( $2 \cdot r$ ) decrease when the internal gas pressure increased. However, the predicted results of bubble sizes deviated from the measured hydrodynamic diameters, probably because the DLS-measured hydrodynamic diameters are the colloidal sizes of NBs in water with interferences from electric double layer formation, coalesces, and other detection variations or artifact. Additionally, the model calculation employed the injection pressures as the internal pressure of NBs, which may not be valid due to bubble expansion or shrinkage. Thus, we varied the internal pressure between one and three times that of the injection gas pressure in the calculation and yielded the prediction results (red and blue dotted lines) that match the experimental data. This implies that the internal pressure of NBs could be one to two times higher than the injection pressure, though they are at similar order of magnitude.

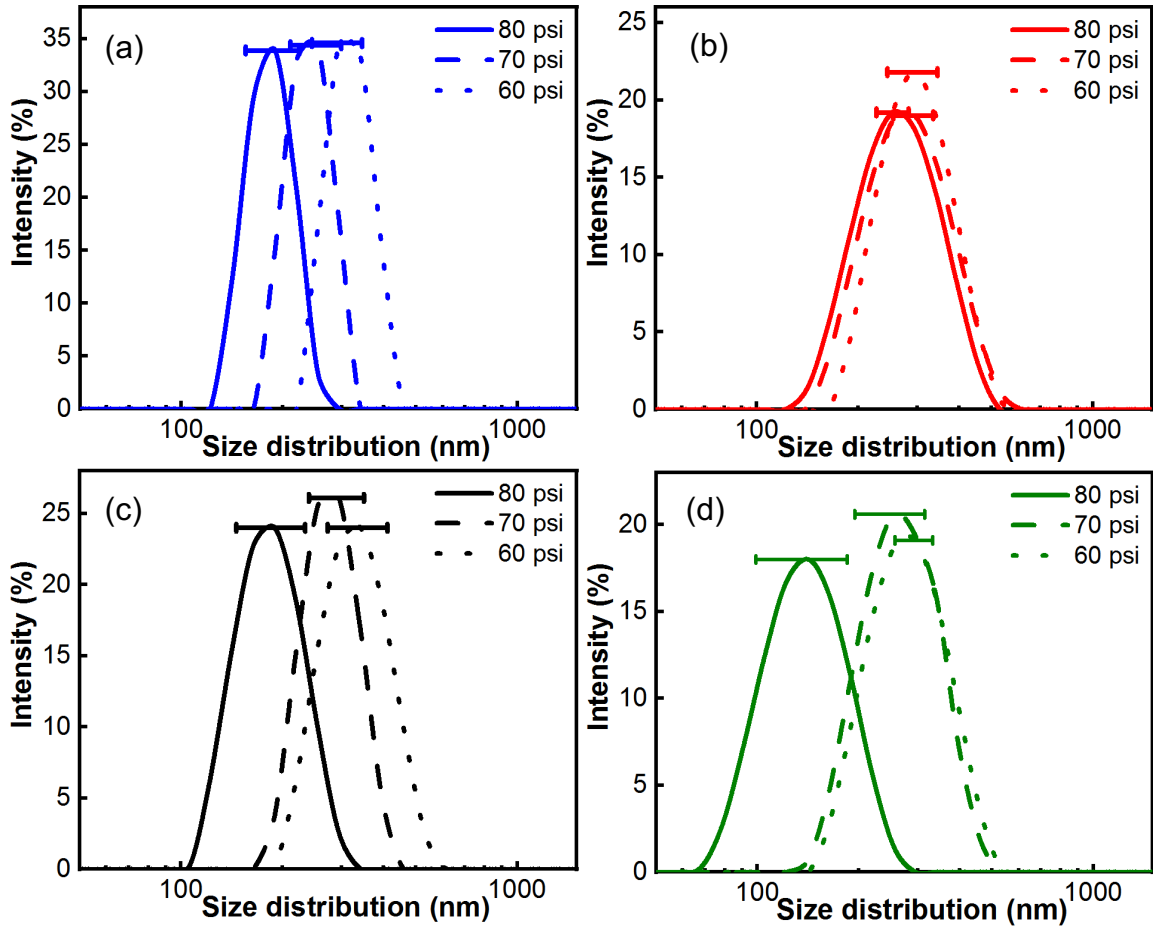


**Figure 2.2** Bubble size distribution in hydrodynamic diameter of (a) O<sub>2</sub>, (b) N<sub>2</sub>, (c) H<sub>2</sub>, and (d) CO<sub>2</sub> NBs under different injection gas pressures.

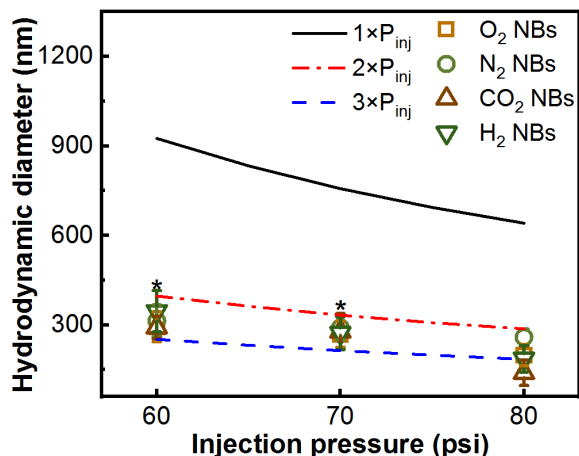


**Figure 2.3** The hydrodynamic diameters of four kinds of NBs in deionized (DI) water under different injection gas pressures. The solid and dotted lines indicate model predictions with different internal pressures used in Equation (2.6).<sup>1</sup> The difference in the NB hydrodynamic diameters produced under 80 psi and the data under 60 or 70 psi was analyzed by a one-way ANOVA (*t*-test, two sided, a significance level of 0.05). The normality of replicate data was examined using the Shapiro Wilks W Test. \*indicates a significant difference ( $p < 0.05$ ) between the two groups of data for the same NB types.

### 2.3.2 Visualization and Assessment of Mechanical Properties of Surface NBs in Water

The spontaneous attachment of bulk NBs on hydrophobic surfaces (e.g. silicon and HOPG) has been reported in literature,<sup>275, 288-293</sup> Bubble attachment on hydrophobic surfaces is primarily due to the van der Waals attraction.<sup>294, 295</sup> The left columns in **Figure 2.4a and 2.4b** show the AFM images of O<sub>2</sub> NBs and N<sub>2</sub> NBs on a silicon wafer. The diameters of these NBs are around  $80 \pm 20$  nm with heights of  $20 \pm 5$  nm, indicating that surface bubbles deformed or spread horizontally on the surface as reported elsewhere.<sup>295</sup> In the AFM's Peakforce tapping mode, the height of NBs may further be underestimated due to the tip-induced deformation.<sup>291, 296</sup> The reduced height in the AFM images is a commonly observed image-processing artifact due to the hysteresis of the servo system.<sup>297</sup> For example, AFM-image leveling is generated from fitting an image profile line with polynomial equations,<sup>279</sup> which may cause discrepancies from a realistic objective height.

Despite of these potential errors, surface NBs are clearly different from surface and bulk NBs according to the Knudsen number analysis, which indicates bulk NBs are not a Knudsen gas type, whereas the surface NBs are Knudsen type.<sup>298</sup> A Knudsen gas is a gas with the mean free path of molecules ( $\lambda$ ) greater than bubble size (height or diameter). A Knudsen number much greater than one indicates Knudsen diffusion is important and the internal gas molecules in surface NBs rarely collide with each other but interact more frequently with the solid substrate and the liquid/gas interface.<sup>299-301</sup>

**Figure 2.4a and 2.4b** middle and right columns provide the mapping of Young's modulus and stiffness with the dark areas corresponding to the surface NBs. AFM generated data of Young's modulus and stiffness in **Figure 2.5a** and **2.5b** are extracted from **Figures 2.4**. **Figure 2.5a** and **2.5b** show that with an injection gas pressure increase from 60 to 80 psi, the Young's modulus of O<sub>2</sub> NBs increased from 20.9±6.0 to 27.8±3.6 MPa, while the stiffness increased from 0.32±0.09 to 0.68±0.03 N·m<sup>-1</sup> (**Figure 2.5c**), which compares well with the prior literature.<sup>302</sup> The measured Young's moduli are greater than the predicted level of ~10 MPa by the classical Young-Laplace equation, because it does not consider the colloidal factors as we used in Equation (2.6). Moreover, both the JKR model and the DMT model were used to verify the AFM-generated Young's moduli of NBs under different gas injection pressures. Obviously, the JKR model predictions of Young's moduli for O<sub>2</sub> and N<sub>2</sub> NBs were consistently less than the DMT predictions or AFM-generated data ( $p < 0.05$ ), which are close to each other. The  $t$ -test analysis indicates that the DMT model prediction results have no significant differences from the AFM-generated data ( $p > 0.05$ ).

**Figure 2.5d** presents the calculated internal pressures of O<sub>2</sub> and N<sub>2</sub> NBs using Equation (2.7) in with the indentation ( $\delta$ ) determined from the force-distance curves obtained on the surface NBs as illustrated in **Figure 2.6**. The calculated internal pressure also increased with the increasing injection pressure when producing bulk NBs in water, which corroborated with the colloidal model prediction in **Figure 2.3**. Moreover, the internal pressure is again shown to be higher than the corresponding injection pressure. Some previous studies have also reported high internal gas pressures of 1000–3000 psi (calculated from the reported gas density of 100 to 280 kg·m<sup>-3</sup>).<sup>303, 304</sup> We predicted lower internal pressures (120–240 psi) that correspond to the gas density of approximately 10–20 kg·m<sup>-3</sup> at room temperature. Thus, the O<sub>2</sub> and N<sub>2</sub> NBs still remain in a dense gas phase as previously reported.<sup>261</sup>

We need to admit that surface NBs and bulk NBs may differ from each other with respect to their shapes, morphologies, internal pressures and stability mechanisms. For example, after deposition of bulk NBs onto a solid substrate, they transform into surface NBs with rapid deformation from spherical to spherical-cap. Moreover, there could be dynamic influx or outflux of the gaseous molecules across the liquid/gas interface that changes the internal states such as gaseous densities, molecular concentrations, and internal pressures. Nevertheless, our experimental results of the internal pressures in Subsection 2.3.1 and 2.3.2, independently obtained from the colloidal force model and AFM indentation methods, both reveals that the internal pressure varied with the injection pressure. Moreover, the surface NBs are shown to have a similar order of magnitude of internal pressures with the bulk NBs, though the surface NBs may have deformed to spherical-cap compared to bulk NBs and thus may have a larger radius of curvature than

bulk NBs and a reduced Laplace pressure. As such, the internal state changes after bulk NBs transformed to surface NBs should be negligible.

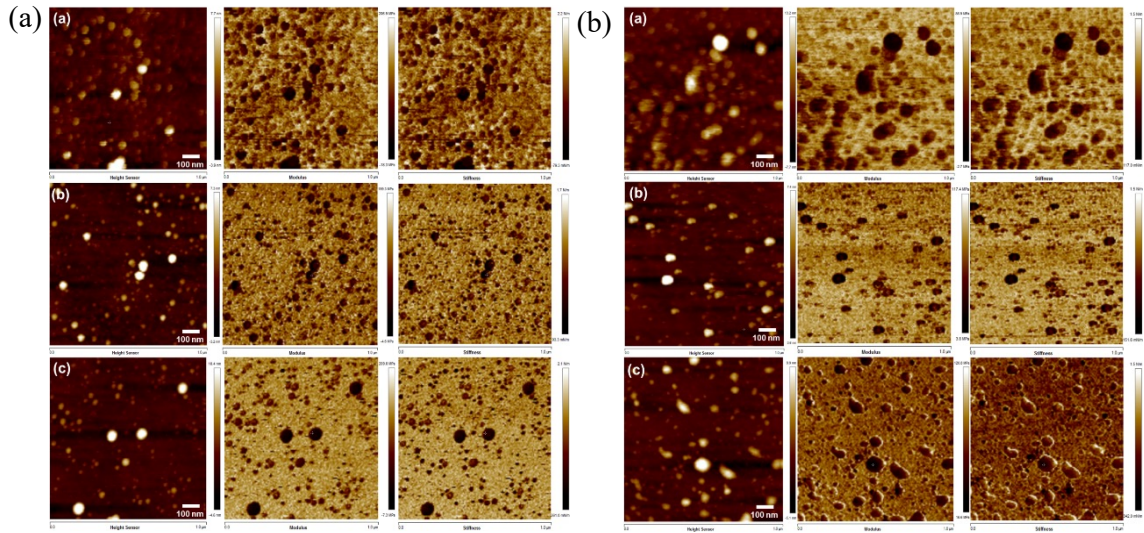


**Figure 2.4** Typical AFM morphological image (left), modulus mapping (middle) and stiffness mapping (right) of  $O_2$  NBs (a) and  $N_2$  NBs (b) on silicon wafer surface generated under different injection gas pressures: (a) 60 psi, (b) 70 psi, and (c) 80 psi.

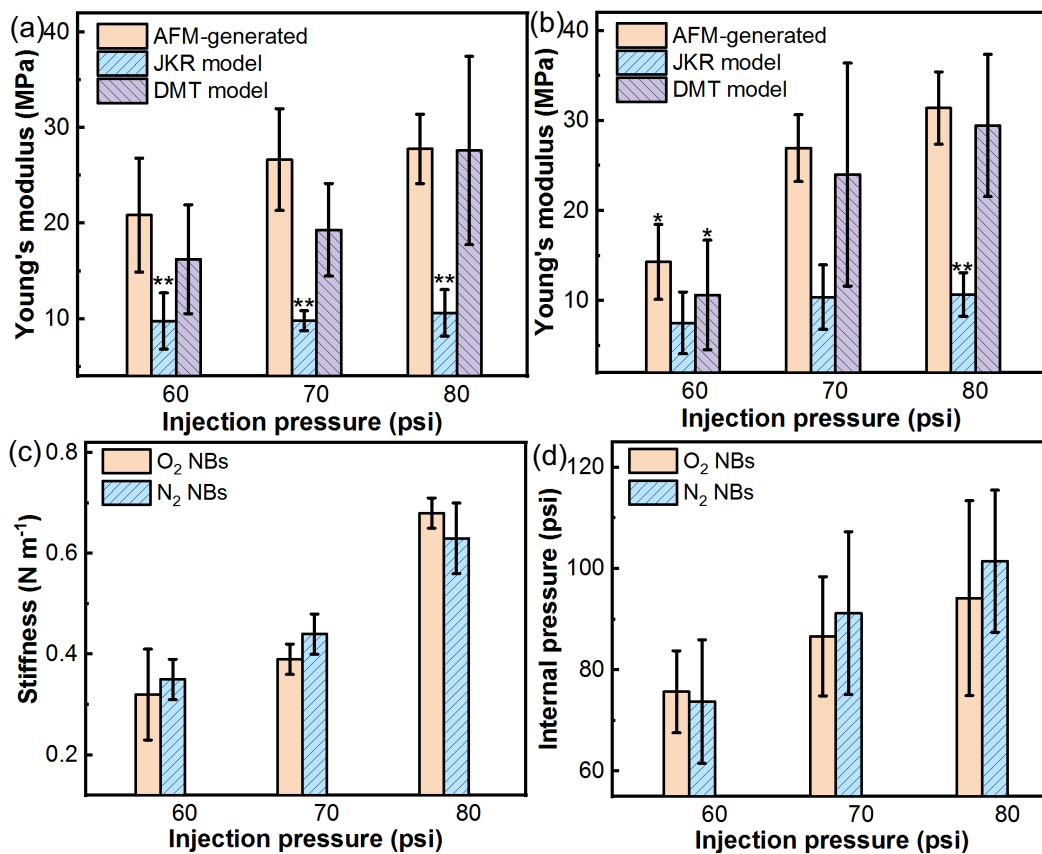


**Figure 2.5** (a) and (b) are the Young's moduli of O<sub>2</sub> and N<sub>2</sub> NBs as measured by AFM (AFM-generated) and calculated by the JKR and DMT models; (c) O<sub>2</sub> and N<sub>2</sub> NB stiffness as measured by AFM under different injection pressures; and (d) comparison of the calculated internal pressure of O<sub>2</sub> and N<sub>2</sub> NBs and the injection gas pressure levels. Error bars are produced from the indentation uncertainties ( $\delta$ ) and adhesion force ( $F_{adh}$ ) read from force curves measured by AFM. The significance of difference for the comparison between the Young's moduli of NBs produced under 80 psi and the data under 60 or 70 psi was analyzed by a one-way ANOVA ( $t$ -test, two sided, a significance level of 0.05). \*indicates a significant difference ( $p < 0.05$ ) between the data groups with under-80 psi data. \*\*indicates a significant difference ( $p < 0.05$ ) between the data group with the other two sets of data using the same specific injection pressure.



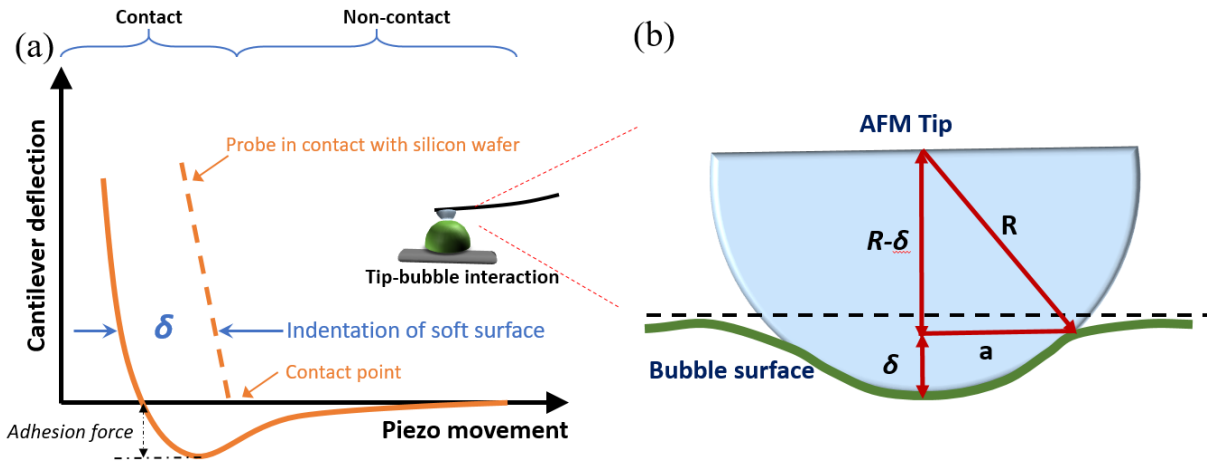


**Figure 2.6** (a) The force-distance curve showing the indentation ( $\delta$ ) of the AFM probe in contact with a bubble surface. (b) An illustration of the AFM tip geometry on the NB deformed surface.

### 2.3.3 Effect of Water Temperatures on Bubble Sizes and NB Concentrations

Water temperatures affect water surface tension, density, and the dielectric constant as well as gaseous solubility, which may indirectly change the stability of NBs in water.<sup>251, 305</sup>.

**Figure 2.7a** and **2.7b** show the bubble sizes of O<sub>2</sub> NBs and N<sub>2</sub> NBs both decreased when the water temperatures increased from 6 to 40 °C. This interesting result could be attributed to the lower water surface tension at higher temperatures that reduces the NBs' size according to the model in Equation (2.6) or the classic Young-Laplace equation. Moreover, **Figure 2.7c** shows that at higher water temperatures (40 °C), both O<sub>2</sub> and N<sub>2</sub> NBs had reduced surface charges, suggesting the bubble-size changes caused a restructured electric double layer due to the bubble size change. **Figure 2.7d** shows the model prediction supports the observed trend of the average hydrodynamic diameters from DLS with water temperatures. **Table 2.2** lists the parameters used in the model calculation of the NB diameters under various water temperatures. Moreover, the predicted diameters using 2–3 times of injection gas pressure (i.e.,  $3 \times P_{inj}$ ) well matched the experimental data, which

agrees with the abovementioned analysis. The NBs' size was reported to be temperature dependent as temperature affects the gas solubility.<sup>306</sup> Moreover, NBs may both grow and shrink when the temperature changes due to the Ostwald ripening (bubbles grow and burst into small bubbles).<sup>307</sup> This suggests the need to further improve the model to incorporate the dissolution or solubility factors under temperature variations when analyzing the bubble size.

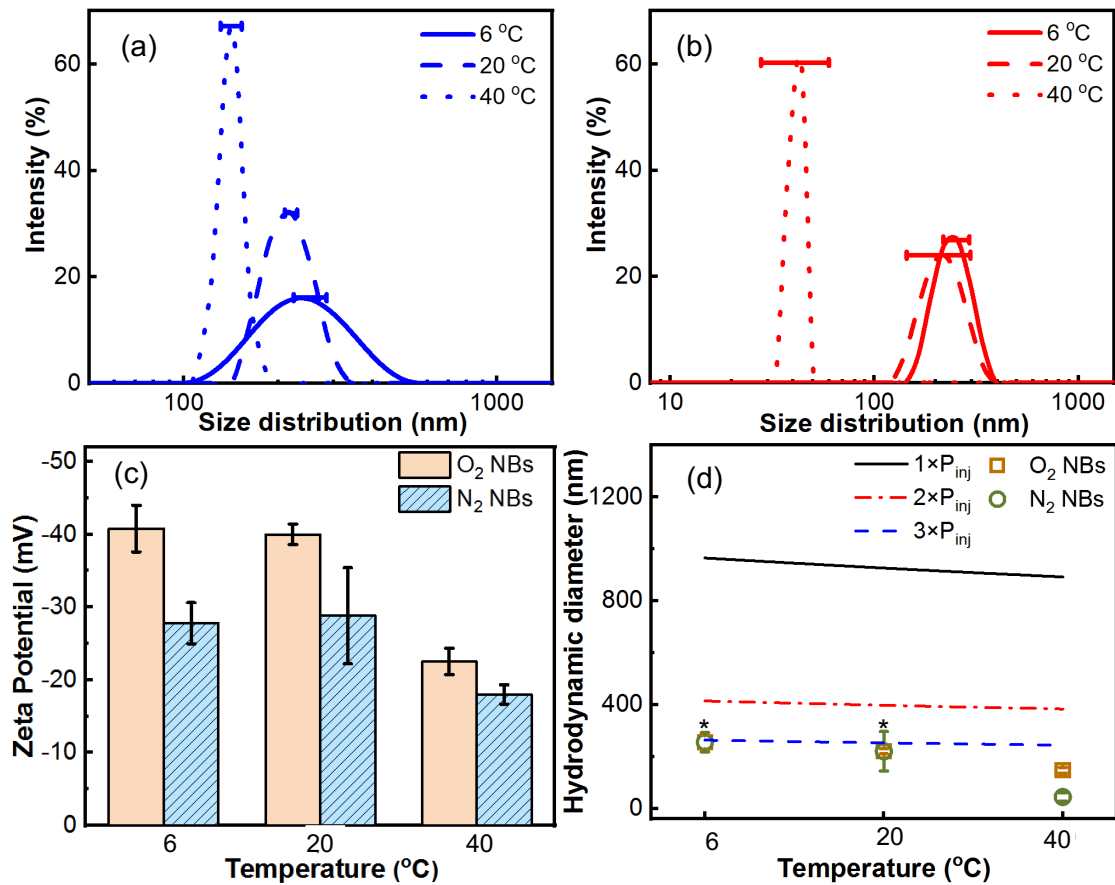


**Figure 2.7** (a) and (b) are the O<sub>2</sub> and N<sub>2</sub> NBs' size distribution produced under 60 psi; (c) the zeta potential of NBs in DI water; (d) a comparison of the observed and model-predicted NB diameters in DI water under different water temperatures. The significance of difference for comparison between the NBs' hydrodynamic diameter produced under 40 °C and the data under 6 or 20 °C was analyzed by a one-way ANOVA (*t*-test, two sided, a significance level  $\alpha = 0.05$ ).

**Table 2.2** Parameters Used in the Calculation of Bubble Size at Different Water Temperatures Using Equation (2.6)

Water temperature (°C)	Water surface tension (mN·m <sup>-1</sup> )	Water density (kg·m <sup>-3</sup> )	Dielectric constant of water
6	75.13	999.90	86.40
20	72.80	998.19	80.36
40	69.47	992.25	73.28

### 2.3.4 The Concentration Changes of NBs Under Different Water Temperatures and Storage Times

As one of the key factors for the long-term stability of aqueous NBs, the temperature effect on bubble concentrations and sizes is also evident as shown in **Figure 2.8a**. The freshly prepared O<sub>2</sub> and N<sub>2</sub> NB concentrations ranged from 4–6×10<sup>8</sup> bubbles·mL<sup>-1</sup> under a room temperature, which is consistent with the literature reports.<sup>308</sup> Bubble concentrations were at similar levels of magnitude at 6 and 20 °C, although the concentrations slightly reduced at a lower temperature. At 40 °C the bubble concentration was significantly reduced by one order of magnitude from a few 10<sup>8</sup> bubbles ml<sup>-1</sup> to 6.4±1.4×10<sup>7</sup> bubbles·ml<sup>-1</sup> for O<sub>2</sub> NBs and 4.7±1.3×10<sup>7</sup> bubbles·ml<sup>-1</sup> for N<sub>2</sub> NBs. Thus, at high temperatures, large-sized NBs may be susceptible to expansion, bursting, or coalescing, whereas smaller NBs shifted the size distribution to a lower range. Furthermore, we analyzed the bubble size distribution and concentrations in water after storage for different times. **Figure 2.8b** indicates that with the storage time, the concentrations of both N<sub>2</sub> and O<sub>2</sub> NBs' suspension decreased progressively. The bubbles sizes measured by DLS were stable for 1~2 months as shown in **Table 2.3**. In the third month, the bubble size distribution became hard to detect, and the zeta potential also decreased significantly.

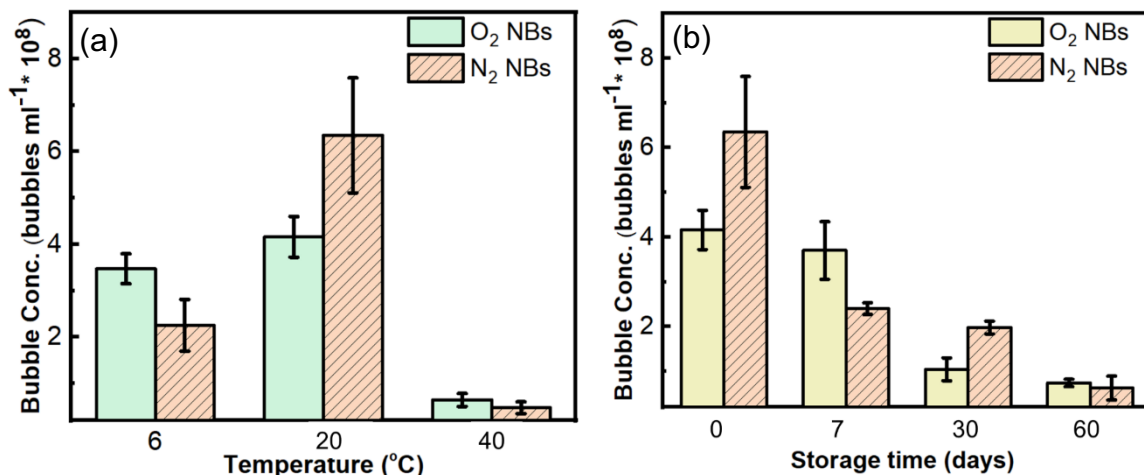


**Figure 2.8** (a) O<sub>2</sub> and N<sub>2</sub> NB concentrations in DI water that were prepared at different temperatures and stored no more than 24 hours. (b) O<sub>2</sub> and N<sub>2</sub> NBs concentrations in DI water after storage in the dark at room temperature (20°C).

**Table 2.3** Hydrodynamic Diameter, Zeta Potential and Dissolved Oxygen Level of N<sub>2</sub> and O<sub>2</sub> NBs With Different Storage Time Under Room Temperature (20°C).

Nitrogen NBs			
Time (month)	Hydrodynamic diameter (nm)	Zeta potential (mV)	DO (mg/L)
0	318.9±43.3	-28.8±6.6	5.2±0.3
1	271.8±54.9	-21.5±6.3	9.2±0.1
2	343.3±92.0	-16.9±5.4	9.5±0.1
3	Not detectable	-12.9±6.8	9.5±0.1
4	Not detectable	-8.6±4.4	9.5±0.1
Oxygen NBs			
Time (month)	Hydrodynamic diameter (nm)	Zeta potential (mV)	DO (mg/L)
0	224.7±19.6	-40.0±1.4	28.7±0.5
1	226.2±46.0	-24.2±9.5	9.6±0.1
2	Not detectable or data is not repeatable	-4.4±3.5	9.6±0.1
3	Not detectable	-1.9±2.6	9.5±0.1
4	Not detectable	-3.2±3.4	9.5±0.1

## CHAPTER 3

### ELECTROCHEMICAL CHARACTERIZATION METHOD DEVELOPMENT FOR REACTIVE NANOBUBBLES

Scanning electrochemical microscopy (SECM) is used to measure the local electrochemical behavior of liquid/solid, liquid/gas and liquid/liquid interfaces. Atomic force microscopy (AFM) is a versatile tool to characterize micro- and nanostructure in terms of topography and mechanical properties. However, conventional SECM or AFM provides limited laterally resolved information on electrical or electrochemical properties at nanoscale. For instance, the activity of a nanomaterial surface at crystal facet levels is difficult to resolve by conventional electrochemistry methods. This chapter reports the application of the combination of AFM and SECM, namely, AFM-SECM, to probe nanoscale surface electrochemical activity while acquiring high-resolution topographical data. Such measurements are critical to understanding the relationship between nanostructure and reaction activity, which relevant to a wide range of applications in material science, life science and chemical processes. The versatility of the combined AFM-SECM is demonstrated by mapping topographical and electrochemical properties of nanobubbles (NBs). Compared to previously reported SECM imaging of nanostructures, this AFM-SECM enables quantitative assessment of local surface activity or reactivity with higher resolution of surface mapping.

#### 3.1 Background and Challenges

Characterization of electrochemical (EC) behavior can provide critical insights into the kinetics and mechanisms of interfacial reactions in diverse fields, such as biology,<sup>309, 310</sup> energy,<sup>311, 312</sup> material synthesis,<sup>313-315</sup> and chemical process.<sup>316, 317</sup> Traditional EC

measurements including electrochemical impedance spectroscopy <sup>59</sup>, electrochemical noise methods <sup>60</sup>, galvanostatic intermittent titration <sup>318</sup>, and cyclic voltammetry <sup>57</sup> are usually performed at macroscopic scale and provide a surface-average response. Thus, it is difficult to extract information on how (electro) chemical-activity is distributed across a surface, but local scale surface properties in nanoscale are especially important where nanomaterials are widely used. Therefore, new techniques capable of simultaneously capturing both nanoscale multidimensional information and electrochemistry are highly desirable.

Scanning electrochemical microscopy (SECM) is a widely used technique for measuring the localized electrochemical activity of materials at micro- and nanoscales <sup>61</sup>. Typically, SECM uses an ultra-microelectrode as a probe for detecting electroactive chemical species as it scans a sample surface to spatially resolve local electrochemical properties.<sup>67</sup> The measured current at the probe is produced by reduction (or oxidation) of the mediator species, and this current is an indicator of the electrochemical reactivity in the surface of sample. SECM has evolved significantly after its first inception in 1989<sup>68, 69</sup> but it is still challenged by two main limitations. Since EC signals are typically sensitive to tip-substrate interaction characteristics, one limitation of SECM is that keeping the probe at a constant-height prevents a direct correlation of electrochemical activity with the surface landscape, due to the convolution of topography with the collected EC information.<sup>71</sup> Second, it is difficult for a commercial SECM system to obtain sub-micrometer ( $\mu\text{m}$ ) image resolution as the spatial resolution is partially determined by the probe dimensions, which is in micrometer scale.<sup>319</sup> Therefore, nanoelectrodes, the electrodes with a diameter in the

nanometer range, are increasingly used in SECM to achieve the resolution below sub-micrometer scale.<sup>320-323</sup>

To provide a constant tip-substrate distance control and obtain a higher spatial electrochemical resolution, several hybrid techniques of SECM have been operated, such as ion conductance positioning<sup>74</sup>, shear force positioning<sup>73</sup>, alternating current SECM<sup>75</sup>, and atomic force microscopy (AFM) positioning. Among these instrumentations, SECM integrating AFM positioning (AFM-SECM) has become a highly promising approach. As AFM is capable of providing fixed tip-substrate distances, the integrated AFM-SECM technique enables simultaneous acquisition of nanoscale surface structural and electrochemical information through mapping or sample sweeping with the sharp AFM tips. Since the first successful operation of AFM-SECM by MacPherson and Unwin in 1996<sup>324</sup>, significant improvements have been achieved on probe design and fabrication, as well as its applications in various research fields such as electrochemistry in chemical and biological processes. For example, AFM-SECM has been implemented for imaging composite material surfaces, such as noble metal nanoparticles<sup>166</sup>, functionalized or dimensionally stable electrodes<sup>167, 175</sup>, and electronic devices<sup>147</sup>. AFM-SECM is capable of mapping the electrochemically active sites from the tip current image.

Simultaneous topographical and electrochemical measurements could also be achieved by other techniques such as conductive AFM<sup>78-81</sup>, electrochemical AFM (EC-AFM)<sup>82-85</sup>, scanning ion conductance microscopy-scanning electrochemical microscopy (SICM-SECM)<sup>74, 86</sup>, and scanning electrochemical cell microscopy (SECCM)<sup>87, 88</sup>. The comparison between these techniques has been discussed in our review paper.<sup>309</sup>

Characterization of NBs mainly used dynamic light scattering (DLS) or laser diffraction techniques for determine the size distribution of bulk NBs,<sup>212, 216, 237</sup> microelectrophoresis for the measurement of zeta potential,<sup>212, 216, 263</sup> and nanoparticle tracking analysis (NTA) technique to analyze the NBs numerical concentration and size distribution.

The aim of the chapter was to employ atomic force microscopy-scanning electrochemical microscopy (AFM-SECM) to demonstrate the electrochemical mapping and measurement on nanobubbles in water. We measured and compared the electrochemical behavior the liquid/gas interfaces for surface nanobubbles (NBs) on gold or silicon substrate. NBs are bubbles with a diameter of  $< 1 \mu\text{m}$  (also known as ultrafine bubbles),<sup>3</sup> and they elicit many intriguing properties,<sup>4, 5</sup> including long residence time in the solutions<sup>6, 325</sup> and higher efficiency of gas mass transfer.<sup>7, 325</sup> Furthermore, the collapse of NBs creates shock waves and the formation of hydroxyl radicals ( $\bullet\text{OH}$ ).<sup>14, 15, 326</sup> We measured the electrochemical reactivity of oxygen NBs in the solution to better understand the fundamental chemical properties of NBs.

## **3.2 Materials and Methods**

### **3.2.1 Nanobubbles Generation**

Different NBs were generated by direct injection of compressed ultra-high purity gases (99.999%, Airgas Inc.) through a tubular ceramic membrane (140 nm pore size, MSKTB01014UM, Sterlitech, U.S) into deionized water as we reported previously.<sup>275</sup> The pressure of the injection gas flow was adjusted by regulators (CGA540 for  $\text{O}_2$ ) under a gas pressure at 60 psi ( $\sim 414$  kPa). The gas was injected continuously for 90 min under a



pressure of 414 kPa and a flow of  $0.45 \text{ L}\cdot\text{m}^{-1}$  to reach stable bubble size distribution and a saturation point.

### 3.2.2 Traditional Electrochemical Measurement in Bulk Solution

As shown in **Figure 3.1**, the electrochemical experiments were carried out on a CHI 660 electrochemical workstation (CH Instrument, USA). A traditional three-electrode system with a 3 mm platinum wire as the counter electrode, an Ag/AgCl electrode as the reference, and an Pt disk electrode (3.0 mm diameter) as the working electrode was employed. All potentials in this paper refer to the Ag/AgCl. The cyclic voltammogram of Pt working electrode was recorded at  $50 \text{ mV s}^{-1}$ . To maintain facile and reproducible electrochemistry, the electrolyte solution was prepared with 20 mM  $\text{K}_3\text{Fe}(\text{CN})_6$  in 0.5M KCl as a supporting electrolyte.<sup>327</sup> The solution was then mixed with ONBs water or DI water (as control group) under a ratio of 1:1. The experiments were operated under 0 to 0.5 V versus Ag/AgCl.

Electrochemical impedance measurements (EIS) were performed at open circuit potential with an amplitude of the sinusoidal potential signal of 10 mV AC over the frequency range from 100 kHz to 10 mHz in 0.5M KCl solution, which was mixed with NBs water or DI water (as control group) under a ratio of 1:1 before test. The open circuit potential on the peak voltage achieved from CV measurements.

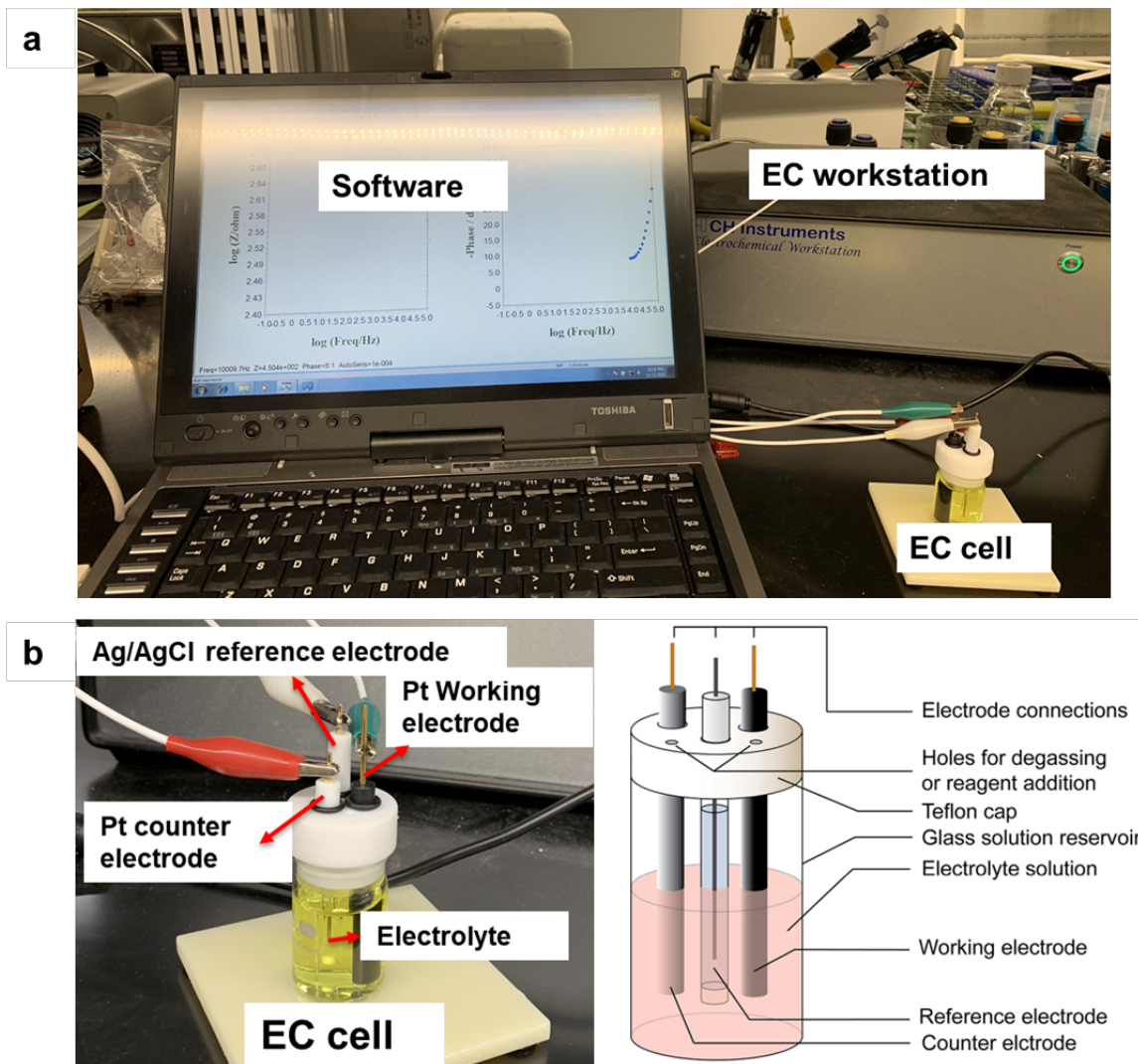


**Figure 3.1** (a) Set up of electrochemical measurements system. (b) Photo and schematic representation of the electrochemical cell.

Source: The right part of b) is reprinted from reference.<sup>328</sup>

### 3.2.3 Topographical and Electrochemical Imaging by AFM-SECM

AFM-SECM measurements were conducted using Dimension Icon with the SECM accessory and CHI 700E bi-potentiostat.<sup>93</sup> Fresh gold plates (Au on Si; model 119-017-307, Bruker, CA) in size of 40 mm×40 mm were used as the substrate to immobilize NBs. The AFM-SECM probes acted as working electrode (Peakforce-secm, Bruker Nano Inc, CA, US), which have a tip radius of 25 nm, and a tip height of 215 nm. As shown in **Figure**

**3.2**, the sample acted as another working electrode, which shares the same pseudo-reference using the Ag wire electrode (0.25 mm in diameter, 249-000-056, Bruker Nano Inc, CA, US) and the counter electrode of a Pt wire (0.25 mm in diameter, 248-000-004, Bruker Nano Inc, CA, US).

10 mM  $[\text{Ru}(\text{NH}_3)_6]^{3+}$  with supporting electrolyte of 0.1 M KCl was used in the presented test. 5~10mM is a commonly used concentration of  $[\text{Ru}(\text{NH}_3)_6]^{3+}$  in literature to obtain good current signals.<sup>175</sup> More examples of commonly used redox mediators in AFM-SECM measurements are summarized in **Table 3.1**.

1.8 mL of the water suspension of oxygen NBs was added on gold substrate in the EC sample cell and stabilized for 10 min. Then 0.9 mL of NBs suspension was decanted and replaced by 0.9 mL of a 10 mM  $\text{Ru}(\text{NH}_3)_6\text{Cl}_3$  solution in 0.1M KCl. Open circuit potential was checked and followed by CVs with a DC bias range from 0 to -400 mV. The probe and the sample could be biased at different potentials (vs the Ag wire pseudo-reference electrode), to enable different redox reactions. In the presented work, the tip reduces the  $[\text{Ru}(\text{NH}_3)_6]^{3+}$  to  $[\text{Ru}(\text{NH}_3)_6]^{2+}$  at -400 mV versus an Ag wire pseudo-reference electrode.

The potential range mentioned here “High E” and “Low E” could be +0.3 V or -0.3 V of “init E/Final E” is a safe choice to start the CV test. Then, the potential range could be adjusted based on the potential value that led to a plateau current in the CV curve. Scan rate could vary between 0.01 V/s to 0.1 V/s. A higher scan rate attributes to a higher sensibility, but the charging current would also increase. Also, at high scan rates the voltammograms presented distorted shapes.<sup>329</sup> A higher sensitivity value should be

selected as long as CV test does not show “overflow”. If an “overflow” message showed, then the sensitivity should be decreased.

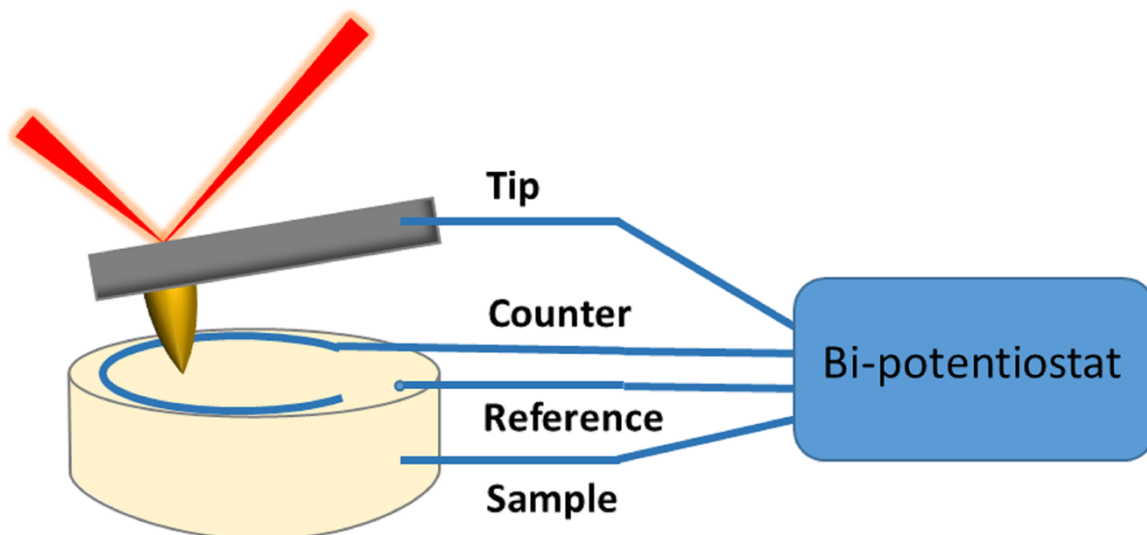


**Figure 3.2** Schematic of AFM-SECM system.

**Table 3.1** Examples of Redox Mediators Used in the Literature

Reaction	$E_0 / V$	Concentration	Applied Potential	Ref
$2H^+ + 2e^- \rightleftharpoons H_2$	0			
$[Ru(NH_3)_6]^{3+} + e^- \rightleftharpoons [Ru(NH_3)_6]^{2+}$	0.10 (NHE)	10 mM	-0.4 V (Ag/AgCl)	175
$2NO_2^- + 3H_2O + 4e^- \rightleftharpoons N_2O + 6OH^-$	0.15(NHE)	0.1 M	+0.95V (Ag/AgCl)	183
$[Fe(CN)_6]^{3-} + e^- \rightleftharpoons [Fe(CN)_6]^{4-}$	0.358(NHE)	2~5 mM	+0.0 ~ 0.5V(Ag/AgCl)	180
$ClO_4^- + H_2O + 2e^- \rightleftharpoons ClO_3^- + 2OH^-$	0.36(NHE)	0.1~1 M	+0.30 V(SCE)	173
$[IrCl_6]^{3-} + 3e^- \rightleftharpoons Ir + 6Cl^-$	0.77(NHE)	10 mM	+1.0 V(Ag/AgCl)	179
$SO_4^{2-} + H_2O + 2e^- \rightleftharpoons SO_3^{2-} + 2OH^-$	-0.93 (NHE)	10 mM	-0.45 V(Ag/AgCl)	185
$AgCl + e^- \rightleftharpoons Ag + Cl^-$	0.22233(NHE)			

### 3.3 Results and Discussion

#### 3.3.1 Traditional Electrochemical Measurements

The CV measurements (**Figure 3.3**) on the electrolyte solution (20 mM  $K_3Fe(CN)_6$  in 0.5M KCl) containing NBs ( $O_2$ ,  $H_2$ ,  $N_2$ ,  $CO_2$ ) shows a higher current peak under the applied potential compared to the same electrolyte solution without NBs. This indicated that NBs may have the potential to facilitate the diffusion and mass transfer of  $[Fe(CN)_6]^{3+}$  from bulk solution to the electrode interface and result in a higher peak current.<sup>8, 330</sup> In amperometry, the potential applied to a electrode and the current is a result of the oxidation/reduction reactions at the electrode surface. The current is recorded as the analytical signal.<sup>331</sup>

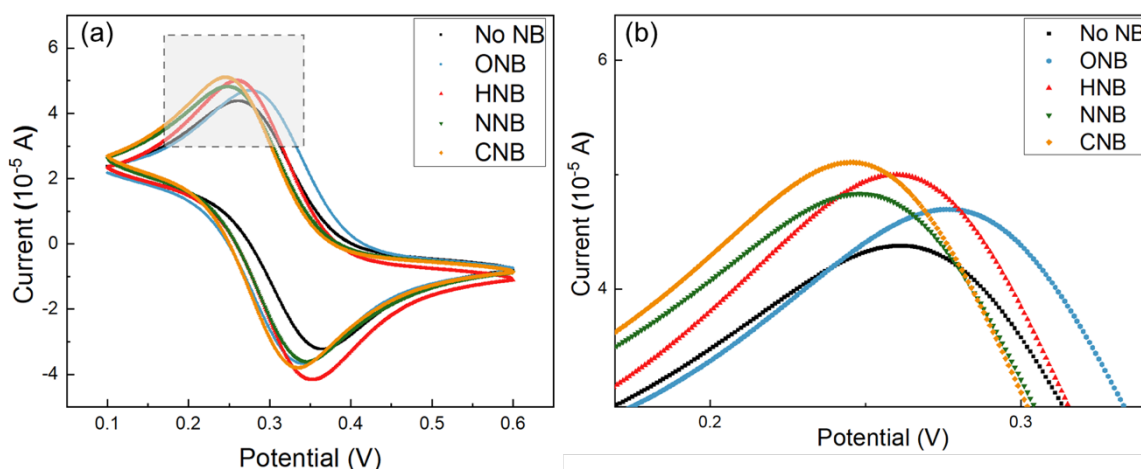


**Figure 3.3** (a) Cyclic voltammetry of NBs water containing different types of gas. (b) Zoom view of the grey-squared part of (a).

The EIS measurements can reveal the conductivities of the electrodes. In Nyquist plot, a semi-circle in high frequencies is related to the electron transfer process. While in

low frequencies, a linear part is corresponded to the diffusion limited process.<sup>332</sup> The Nyquist plot (**Figure 3.4**) here shows a small semi-circle in high-frequencies, a big semi-circle in middle frequencies and a linear part in low frequencies. The presence of two semi-circles associated to two RC circuits.<sup>333</sup> The diameter of the semicircle can be assigned as the charge-transfer resistance ( $R_{ct}$ ) at the interface between the electrode and the electrolyte.<sup>334</sup> A reasonable explanation is that NBs attached on the surface of cathode and form a layer.  $Fe(CN)_6^{3-}$  passes through the layer of the attached NBs and reached to the vicinity near the surface of Pt electrode. After reduced to  $Fe(CN)_6^{4-}$ , the products transfer from the attached NBs layer and diffuse to bulk solution.<sup>332</sup> Electrolyte solutions containing NBs, especially with carbon dioxide NBs, hydrogen NBs, and nitrogen NBs showed a smaller charge-transfer resistance, which may indicate that NBs could promote the charge transfer at the interface of electrode and solution.

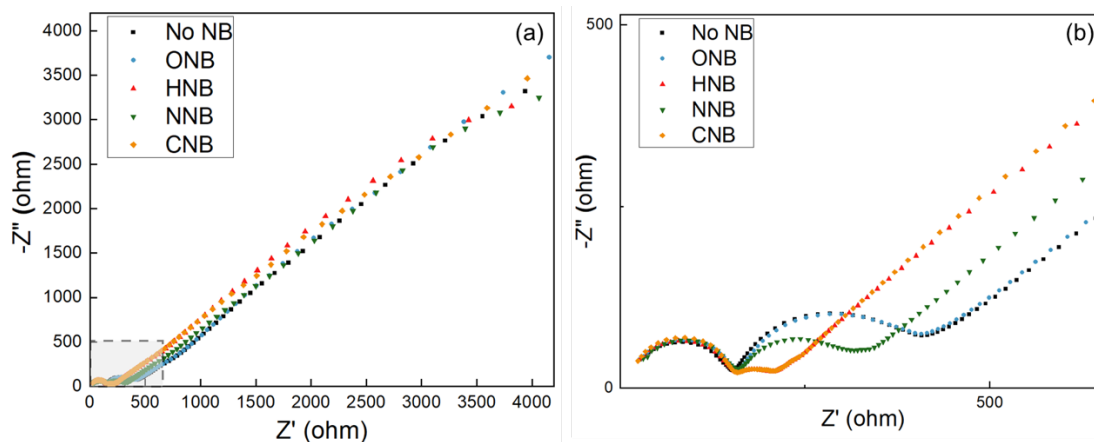


**Figure 3.4** Nyquist plot of NBs water containing different types of gas. (b) Zoom view of the grey-squared part of (a).

### 3.3.2 Topography and Current Imaging of Oxygen NBs by AFM-SECM

Previous studies that characterized NBs with AFM only reported topography images to reveal the size and distribution of NBs immobilized on a solid substrate.<sup>335, 336</sup> Our experiments revealed both morphological and electrochemical information. Individual oxygen nanobubbles (ONBs) can be clearly identified in **Figure 3.5**, which provides the topography as well as the tip current mapping or information. The tip current was generated by the redox reaction of  $[\text{Ru}(\text{NH}_3)_6]^{3+}$  that is reduced to  $[\text{Ru}(\text{NH}_3)_6]^{2+}$  at the tip under a bias potential at -0.4V, as depicted in **Figure 3.5c**. A comparison of the topography and current image evidences the good correlation between the locations of the NBs and the current spots. This result confirms that ONBs could facilitate the diffusion and mass transfer of  $[\text{Ru}(\text{NH}_3)_6]^{3+}$  from bulk solution to the tip area<sup>8</sup> and result in a higher current (relative to the substrate background current of 6 pA) when the AFM-SECM tip scanned over NBs.<sup>330</sup>

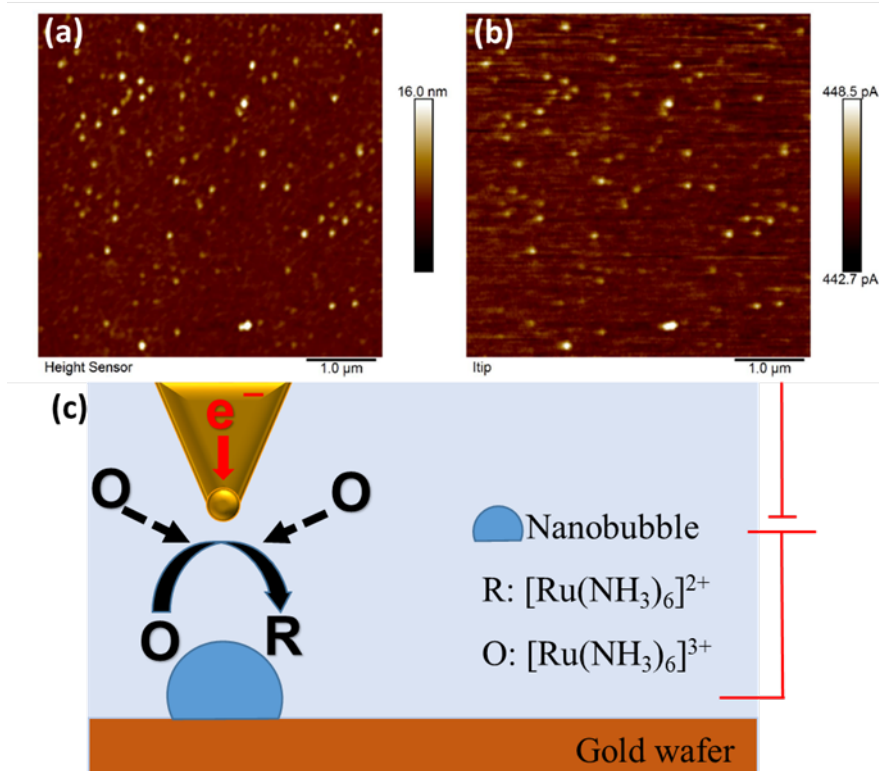


**Figure 3.5** Simultaneously acquired topography (a) and tip current (b) images of oxygen NBs in electrolyte containing 10 mM  $[\text{Ru}(\text{NH}_3)_6]^{3+}$  and 0.1 M KCl. The tip with a tip radius of 25 nm was biased at -0.4V (c) Schematic illustration of AFM-SECIM measurement of NBs.

In the presented measurement, -0.4 V versus Ag/AgCl (-0.18V versus NHE) was chosen to perform the reduction of  $[\text{Ru}(\text{NH}_3)_6]^{3+}$ . The probe may reduce the  $[\text{Ru}(\text{NH}_3)_6]^{3+}$  to  $[\text{Ru}(\text{NH}_3)_6]^{2+}$  at -0.35 to -0.5 V vs Ag wire pseudo-reference electrode, while the sample maybe biased at 0 to -0.1 V for  $[\text{Ru}(\text{NH}_3)_6]^{3+}$  regeneration. This value depends on the plateau current measured in the CV scan. It will also vary with different redox mediators as summarized in **Table 3.1**.



## CHAPTER 4

### INFLUENCES OF AIR, OXYGEN, NITROGEN, AND CARBON DIOXIDE NANOBUBBLES ON SEEDS GERMINATION AND PLANTS GROWTH

Nanobubbles (NBs) hold promise in green and sustainable engineering applications in diverse fields (e.g., water/wastewater treatment, food processing, medical applications, and agriculture). This chapter investigated the effects of four types of NBs on seed germination and plant growth. Air, oxygen, nitrogen, and carbon dioxide NBs were generated and dispersed in tap water. Different plants including lettuce, carrot, fava bean, and tomato were used in germination and growth tests. The seeds in water containing NBs exhibited 6-25% higher germination rates. Especially, nitrogen NBs exhibited considerable effects in the seed germination, whereas air and carbon dioxide NBs did not significantly promote germination. The growth of stem length and diameter, leave numbers, and leave width were promoted by NBs (except air). Furthermore, the promotion effect was primarily ascribed to the generation of exogenous reactive oxygen species (ROS) by NBs and higher efficiency of nutrient fixation or utilization.

#### 4.1 Background and Challenges

Microbubbles (MBs) are generally defined as gaseous bubbles with diameter less than 100  $\mu\text{m}$  and larger than 10  $\mu\text{m}$ .<sup>2</sup> Nanobubbles (NBs) are bubbles with a diameter of  $< 1 \mu\text{m}$  (also known as ultrafine bubbles).<sup>3</sup> The ultrasmall sizes of the micro- and nanobubbles (MNBs) elicit many intriguing properties.<sup>5</sup> For example, NBs have long residence times in the solutions due to their low buoyancy<sup>3,25</sup> and high efficiency of gas mass transfer due to the reduced bubble size (high surface area) and increased internal pressure.<sup>7, 325</sup> Furthermore, the increased specific surface area of NBs increases the contact area between

liquid and gas,<sup>8</sup> which facilitate mass transfer, sorption, and chemical reactions at the gas/liquid interface. Therefore, MNBs have rapidly transformed into innovative technologies with versatile applications in agriculture, aquaculture, food engineering, waste water treatment, and medical applications (e.g. drug delivery for chemotherapy).<sup>8, 9,</sup>  
<sup>11</sup> The application of oxygen NBs enhanced the oxygen concentration from 7.7 mg/L in normal distilled water to 31.7 mg/L after 30 minutes.<sup>12</sup> Thus, NBs are also used in aquaculture to improve the water quality and replenish dissolved oxygen, which increases the productivity of fish in limited space.<sup>13</sup>

The collapse of NBs creates shock waves, which in turn, promotes the formation of hydroxyl radicals ( $\bullet\text{OH}$ ), a highly reactive oxygen species (ROS) that nonspecifically reacts with and decomposes organic matters.<sup>14, 16</sup> MBs have also been demonstrated to remove residual pesticides of vegetables and improve the quality of produce.<sup>17</sup> The collapse of NBs creates the shock waves and promotes the formation of hydroxyl radicals which is essential for pollutant degradation.<sup>14, 15</sup> Applying NBs in water treatment could efficiently remove water contaminants (e.g., rhodamine B, p-nitrophenol, and alachlor.).<sup>2, 19</sup> For example, Fenitrothion is an agricultural pesticide that is harmful to fish, animals, and humans. Ozone MBs were shown to remove and degrade fenitrothion in lettuce, cherry tomatoes, and strawberries.<sup>18</sup>

Recently, NBs have been introduced into agricultural applications (e.g., promoting plant growth and germination). For example, several studies demonstrated that the use of NBs promotes fast germination time and growth of seeds.<sup>47-49</sup> Germination rates of barley seeds submerged in water containing NBs (bubbles formed from gas mixtures of nitrogen and pure air) were 15–25% greater than those of seeds submerged in distilled water with

the same concentration of dissolved oxygen.<sup>50</sup> Germination of seed is one of the first and most fundamental life stages of a plant and largely determines plant growth and yield production.<sup>337</sup> Germination begins with water uptake by the seed (imbibition) and ends with the start of elongation by the embryonic axis. Germination is a complex process during which the seed must quickly recover physically from maturation drying, resume a sustained intensity of metabolism, complete essential cellular events to allow for the embryo to emerge, and prepare for subsequent seedling growth.<sup>338</sup> For germination to occur, seeds require moisture, a suitable temperature, and in most cases aerobic atmosphere.<sup>338</sup>

In addition, MBs have proven to facilitate the growth of plants such as lettuce in the nutrient solutions.<sup>51</sup> Water containing air MBs led to a 2.1 times greater fresh lettuce leaf weight and 1.7 greater dry leaf weight than macro-bubble treated plants.<sup>52</sup> NBs were shown to enhance the growth of plant by improving oxygen supply as nutrients elements.<sup>339</sup> Moreover, according to a previous study,<sup>53</sup> rice growth did not differ between plants irrigated with NB water (water saturated by oxygen nanobubbles) and those irrigated with control water (without nanobubbles), but NB water significantly reduced cumulative CH<sub>4</sub> emission during the rice-growing season by 21%. The amounts of iron, manganese, and arsenic that leached into the drainage water before full rice heading were also reduced by the NB water. However, most of these previous studies used MBs for plant growth promotion and only a few of them employed NBs. Seiichi Oshita et al. showed accelerated seed germination rates in mixed nitrogen and air NBs water compared to that in distilled water, and indicated that NBs promoted physiological activity of plants because of the generation of exogenous ROS and increased the mobility of the water molecules in bulk.<sup>48</sup>

<sup>49</sup> One of the key advantages of NBs for agricultural applications is that potentially

environmentally-harmful chemicals in fertilizer or insecticide production and utilization can be reduced or eliminated. NBs could be a more environmentally sustainable alternative to improve crop yield.

Despite of the intensive studies on agricultural applications of NBs, the enhancement mechanisms for NBs (e.g., different types or compositions) on seed germination and plant growth remain elusive. Moreover, the roles of ROS produced in the suspension of NBs in the germination and growth process are not fully understood. In this study, we investigated the effects of four types of NBs on the germination and growth of plants. Air, oxygen, nitrogen, and carbon dioxide NBs were generated in tap water, and applied on the germination and growth tests for lettuce, carrot, tomato and Fava bean. Tap water was used as a watering reference datum (control group) for comparison. Photoluminescence technique was used to characterize the ROS generation in different suspension of NBs. We further analyzed the potential mechanisms behind the promotion effects of NBs and the roles of reactive oxygen radicals and nutrient delivery in germination and plant growth.

## **4.2 Materials and Methods**

### **4.2.1 Production and Storage of NBs Suspensions Containing Air, O<sub>2</sub>, CO<sub>2</sub>, and N<sub>2</sub>**

Different kinds of NBs including air nanobubbles (ANBs), oxygen nanobubbles (ONBs), carbon dioxide nanobubbles (CNBs), and nitrogen nanobubbles (NNBs) were generated by direct injection of compressed air (Ultra zero grade air, Airgas Inc.), oxygen (purity 99.999%, Airgas Inc.), carbon dioxide (purity 99.99%, Airgas Inc.), and nitrogen (purity 99.999%, Airgas Inc.) through a tubular ceramic membrane (100 nm pore size, WAF0.1,

Refracton, USA) into tap water as we reported previously.<sup>253</sup> The gases were injected continuously for 90 min under a pressure of 414 kPa and a flow of 0.45 L·m<sup>-1</sup> to reach stable bubble size distribution and a saturation point.<sup>253</sup> The hydrodynamic diameters of the produced NBs were measured by dynamic light scattering (DLS) on a Zetasizer Nano ZS instrument (Malvern Instruments) as reported previously.<sup>253, 276</sup> The bubble size distribution is shown in **Figure 4.1**. Dynamic light scattering (DLS) on a Zetasizer Nano ZS instrument (Malvern Instruments), was used to monitor bubbles size distribution (BSD). The suspension of NBs was transferred into glass cuvettes with 1 cm light transmission path and tested immediately by DLS. The BSD were performed at a scattering angle of 173° and a temperature of 25°C. The triplicate measurements for each sample were performed and each measurement consisted of fifteen runs.

The used tap water was firstly left at ambient temperature for 24 hours to allow the free residual chlorine to exit water.<sup>340</sup> Fresh NBs suspension was used immediately for the plant growth tests. However, for germination tests, all types of NBs suspension were generated every three days, stored separately in closed 1-gallon water bottles and used daily. The pH for ANBs, ONBs, and NNBs and tap water were between 6 and 7 and the pH for CNBs was around 4.5. We monitored the dissolved oxygen of the freshly and stored NBs suspension with Orion Star A329 Multi-Parameter Meters (Thermo-Fisher Scientific, USA).

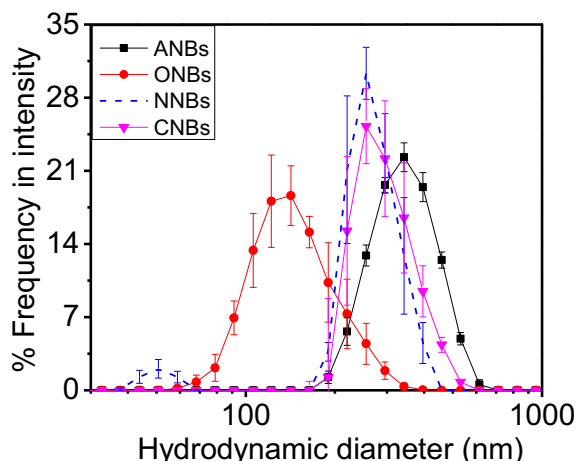


**Figure 4.1** Hydrodynamic diameter of ANBs, ONBs, NNBs, and CNBs.

#### 4.2.2 Examination of ROS Production in Water Suspension of NBs

The generation of hydroxyl radicals ( $\bullet\text{OH}$ ) by NBs was detected by a photoluminescence (PL) technique with terephthalic acid as a probe molecule.<sup>341, 342</sup> Terephthalic acid readily reacts with  $\bullet\text{OH}$  to produce highly fluorescent product, 2-hydroxyterephthalic acid. The intensity of the PL peak of 2-hydroxyterephthalic acid is in proportion to the amount of  $\bullet\text{OH}$  radicals produced in water. This method relies on the PL signal at 425 nm of the hydroxylation of terephthalic acid with  $\bullet\text{OH}$  generated by NBs.

Compressed air, oxygen, nitrogen and carbon dioxide were separately purged into 300 mL of the  $5 \times 10^{-4}$  M terephthalic acid solution with a concentration of  $2 \times 10^{-3}$  M NaOH in a 1L beaker for 30 min at a constant temperature of 20 °C. To increase the collapse rate of NBs, an ultrasonic wave (100 W, 42 kHz $\pm$ 6%) was applied to the four paralleled samples of control and NB suspensions for different times (0 min, 0.5 min, 3 min and 6 min). After ultrasonication, the PL spectra of these liquid samples were measured on a Hitachi fluorescence spectrophotometer to determine the generated 2-hydroxyterephthalic acid.

### 4.2.3 Germination Tests

Lettuce, carrot, and fava bean seeds were used in germination tests. The seeds of lettuce (*Lactuca sativa*), carrot Scarlet-Nantes type (*Daucus carota ssp. sativus*) and fava bean (*Vicia faba*) were purchased from Home Depot in July 2017 with details shown on the package in **Figure 4.2**.



**Figure 4.2** Image of the seeds. (a) Carrot; (b) Tomato; (c) Lettuce; (d) Fava bean.

For each seed type, five paralleled groups were prepared to investigate the effects of four different NBs on their germination rates, which were calculated daily by the percentage of germinating seed number to the total number on the Petri dish.<sup>343</sup> Among the five groups, there was a control group using tap water without NBs. The other four groups were performed by watering the seeds with suspensions of different NBs including ANBs, ONBs, NNBs, and CNBs. Each group was composed of 25 seeds, and each 5 seeds were separately submerged in 10 mL of the tested NB suspension inside a non-sterilized petri dish (**Figure 4.3**). All petri dishes were kept at the same room temperature (~23 °C) and natural light conditions. During the germination experiments, the tap water and the NBs solutions were changed every 24 hours from the stored bottles to avoid the depletion of

oxygen or water evaporation and also to replenish the dose of NBs.<sup>49</sup> Germination tests for lettuce, carrot, and bean seeds lasted for about 6–10 days. The seed's sizes and weights were measured before and after the tests. The hypocotyl lengths were measured daily to compare hypocotyl elongation. Images were captured daily for all tested seeds, and processed by the ImageJ software to measure the hypocotyl length of the seeds.<sup>344</sup> The images, hypocotyl elongations, and germination rates of the tested seeds were compared among all different applied NBs.

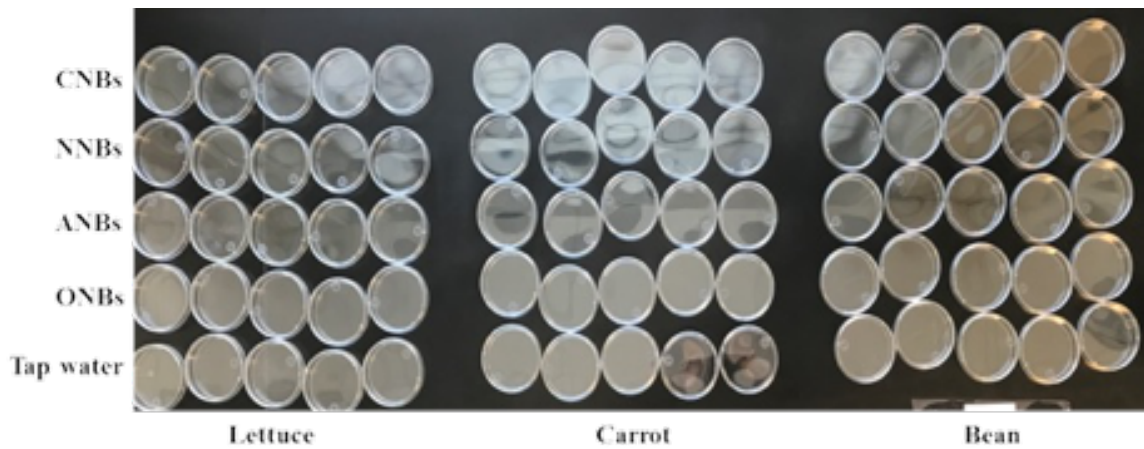


**Figure 4.3** The setup of seeds germination tests.

#### 4.2.4 Plant Growth Tests

For growth study Fava bean (*Vicia faba*), carrot, and tomato san marzano (*Solanum lycopersicum*) were grown in the garden soil (Miracle-Gro soil). The plants were grown in rectangle tabletop planters with saucers as shown in **Figure 4.4**. The height, width, and length of the planters were 16.75, 20.02, and 60.33 centimeter(cm) respectively. Five groups of each plant type were cultivated. All groups were subjected to irrigation every



three days by saturated water suspension of ANBs, ONBs, NNBs, CNBs, and tap water only (control group). For each group, five seeds were inoculated in one planter with an apart distance of approximately 10 cm. For growth tests, the length or diameter (cm) of the leaves, stem, and root were measured depending on the growth rate with a Caliper. The results were expressed as an average with standard deviation as the error bars.

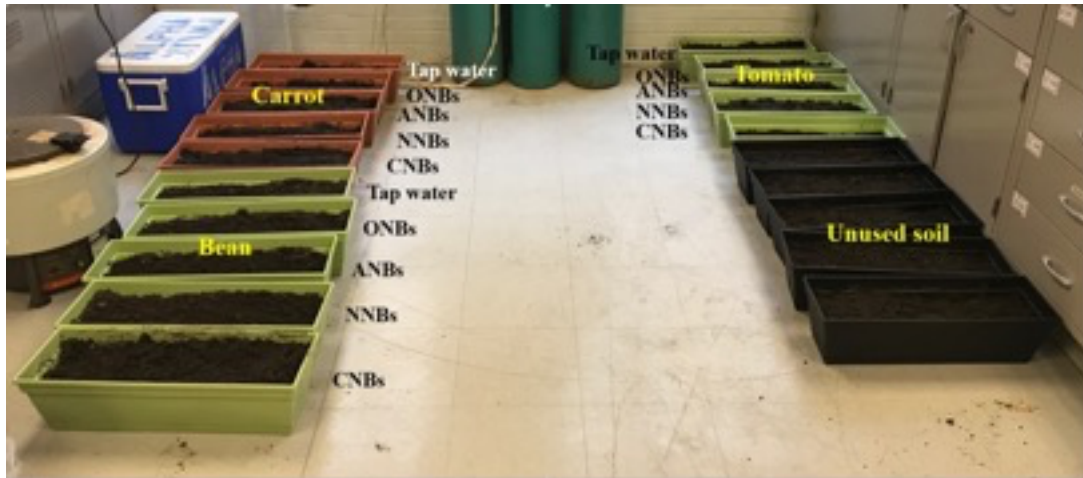


**Figure 4.4** Real photo of the setup of the plants growth tests.

#### 4.2.5 Statistical Analysis

All comparisons were made between the control samples (irrigated by tap water only) and the test groups that underwent the treatments with different NB waters in all the tests. The significance of difference for comparison was analyzed by one-way ANOVA (t-test, two sided, a significance level  $\alpha = 0.05$ ). The results of the  $t$  tests are summarized in **Table 4.1**. The normality of replicate data on seed germination and plant growth data was examined, when necessary, upon Shapiro Wilks W Test by SPSS 11.5 ( $p > 0.05$ ).

**Table 4.1** *p* Values For The T-Tests Between Control Groups (Irrigated By Tap Water Only) And The Test Groups That Underwent The Treatments With Different NB Waters On Seeds Germination And Plant Growth Data. Shaded Cells Indicate That  $P > 0.05$  And Thus There Is No Statistical Difference Between The Test Group And Control Group.

<b>Germination rates (Figure 4.5, a-c)</b>				
	ONBs	ANBs	NNBs	CNBs
Lettuce (a)	1.35E-01	2.34E-01	1.47E-02	2.65E-02
Carrot (b)	3.12E-01	1.00E+00	4.52E-03	6.09E-01
Bean (c)	1.95E-01	1.04E-02	2.76E-03	3.84E-01
<b>Hypocotyl length (Figure 4.6, a-c)</b>				
	ONBs	ANBs	NNBs	CNBs
Lettuce (a)	8.32E-02	1.65E-02	1.81E-02	2.95E-01
Carrot (b)	1.16E-02	9.16E-01	1.23E-02	4.05E-01
Bean (c)	1.50E-02	2.10E-01	8.36E-02	7.84E-01
<b>Stem length (Figure 4.7, a-c)</b>				
	ONBs	ANBs	NNBs	CNBs
Bean (a)	1.92E-04	1.67E-01	1.59E-03	5.88E-03
Carrot (b)	2.73E-02	4.21E-03	5.10E-03	5.48E-03
Tomato (c)	2.18E-03	5.90E-02	6.14E-03	6.20E-03
<b>Stem diameter (Figure 4.8, d-f)</b>				
	ONBs	ANBs	NNBs	CNBs
Bean (d)	3.33E-02	1.67E-03	2.43E-07	3.04E-02
Carrot (e)	9.65E-04	9.65E-04	9.65E-04	9.65E-04
Tomato (f)	6.27E-10	6.86E-05	1.36E-08	2.25E-06
<b>Leaves length (Figure 4.11, a-c)</b>				
	ONBs	ANBs	NNBs	CNBs
Bean (a)	3.63E-02	6.80E-03	7.73E-01	1.14E-03
Carrot (b)	3.04E-01	3.47E-01	6.51E-01	1.20E-02
Tomato (c)	1.15E-02	4.60E-03	1.17E-02	2.62E-03
<b>Leaves width (Figure 4.11, d-f)</b>				
	ONBs	ANBs	NNBs	CNBs
Bean (d)	4.02E-01	7.91E-03	6.21E-04	9.38E-01
Carrot (e)	3.70E-03	4.10E-01	2.36E-02	2.47E-02
Tomato (f)	6.27E-10	6.86E-05	1.36E-08	2.25E-06

## 4.3 Results

### 4.3.1 Effect of Different Types of NBs on the Germination Rates of Vegetable Seeds

**Figure 4.5** shows that four types of NBs consistently promoted the germination rates of lettuce, carrot and bean. After 6 days of submersion, the lettuce germination rate reached 100% with NNBs ( $p < 0.05$  as shown in **Table 4.1**) followed by CNBs, ONBs, ANBs, and tap water, which corresponded to the germination rates of 85%, 85%, 82%, and 80%, respectively. The same results were achieved on carrot and bean, for which the germination rates were highest under irrigation by NNB water. For carrot and bean, ANBs and CNBs did not significantly promote germination compared to tap water. ( $p > 0.05$ ) Thus, NNBs had a considerable promotion effect on the germination rate, probably because of the effective delivery of nitrogen elements or other growth factors by NBs.<sup>7, 325</sup>

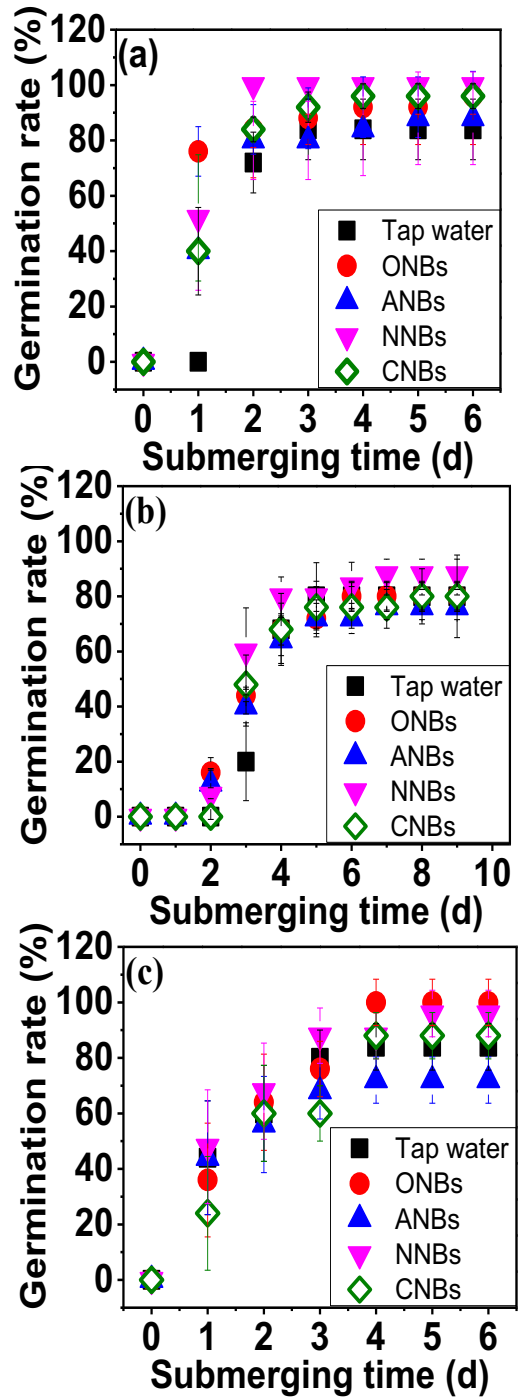


**Figure 4.5** Effect of different types of NBs on the germination rates of (a) lettuce, (b) carrot, and (c) bean.

### 4.3.2 Effect of NB Type on the Hypocotyl Length of Vegetable Seeds

**Figure 4.6** shows that the hypocotyl length growth was fasten by exposure to NNBs, or ONBs ( $p < 0.05$ ). For all three kinds of seeds, CNBs made no significant difference to the hypocotyl length ( $p > 0.05$ ). ANBs appeared to slow down the growth rates of hypocotyls length compared to tap water, which is observed in last two days. **Figure 4.7** shows the hypocotyl growth process of lettuce under immersion into different NB waters and tap waters. Clearly, the promotion effects by NBs became evident on the 4<sup>th</sup> and 6<sup>th</sup> days of incubation. Seeds exposed to NBs had a higher germination rate and hypocotyl length than seeds treated with tap water.

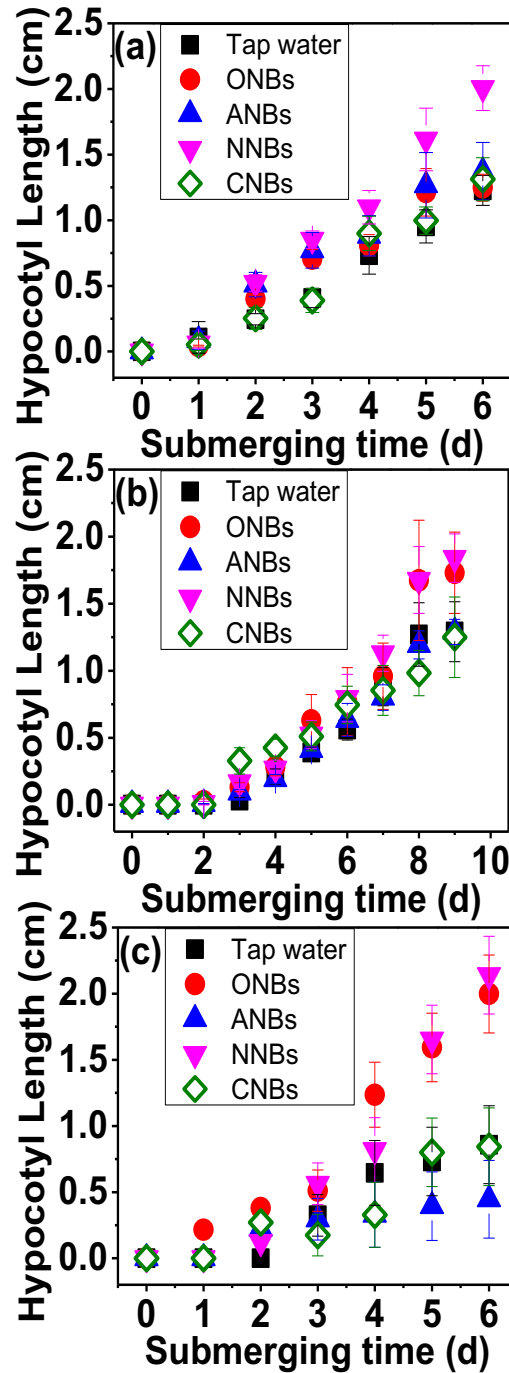


**Figure 4.6** Effect of different types of NBs on the hypocotyl length during germination of (a) lettuce, (b) carrot, and (c) bean.

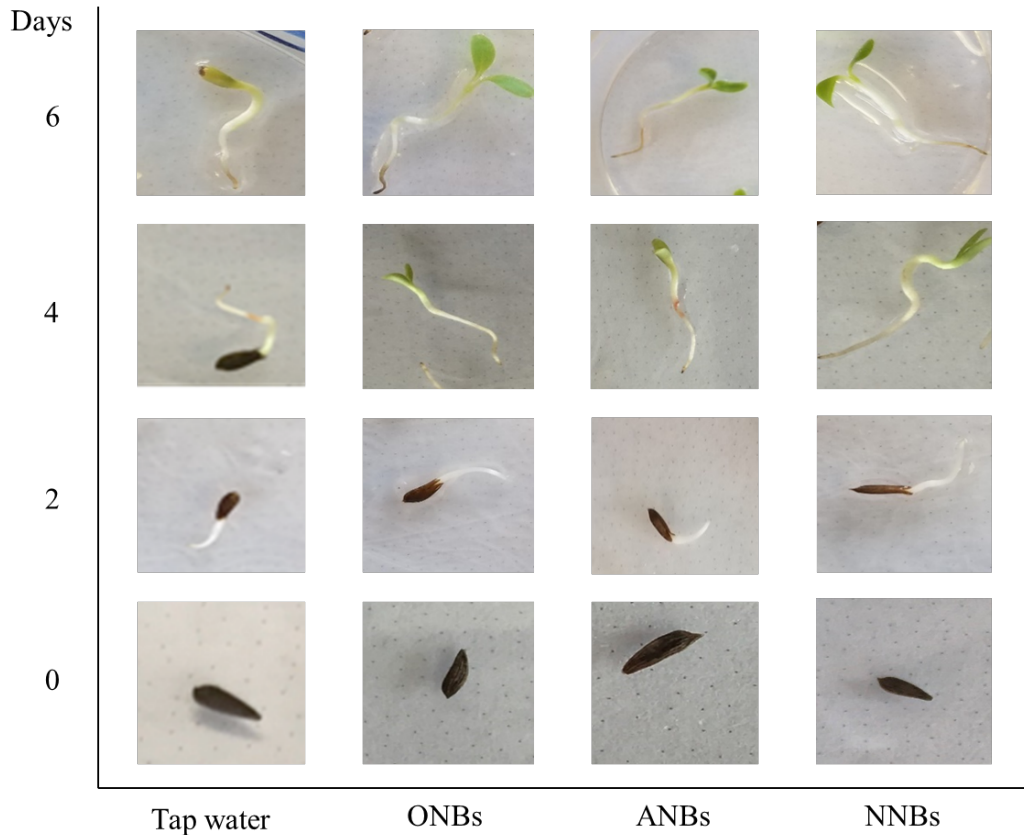


**Figure 4.7** Photos of hypocotyl growth process of lettuce seeds at different submersion days.

### 4.3.3 Effect of NBs Type on the Vegetable Growth

**Figures 4.8** presents the leaf numbers of tomato, carrot and beans under exposure to different kinds of NBs. Compared to tap water, the numbers of leaves were increased with exposure to most of the tested NBs. NNBs led to significantly increase in tomato leaves number ( $p < 0.05$ ), whereas ANBs did not increase but instead reduced the number of tomato leaves. The  $t$ -test indicated that compared to tap water, NNBs had a significant promotion effect on all plants ( $p < 0.05$ ); CNBs only had a significant promotion effect on bean plant; and ONBs promoted tomato. Conversely, ANBs had a negative effect on tomato growth. Other groups did not show significant differences from the control group.

**Figures 4.9** shows that beans after one week of watering by four different NBs grew quite differently. NBs-treated beans grew faster with apparent leaves sprouting out of their buds, whereas the tap water-treated ones had no leaf sprout during the same initial growth period.

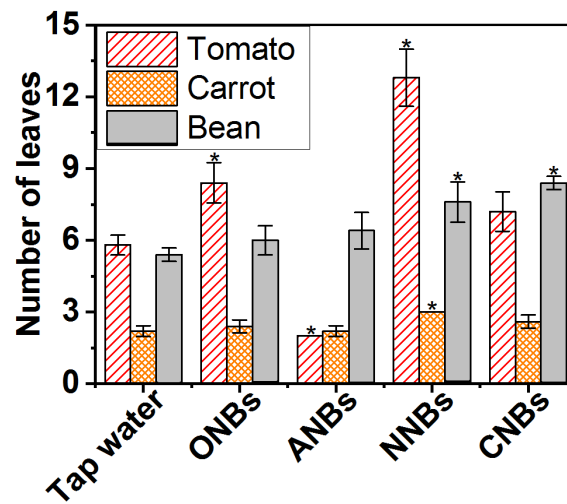


**Figure 4.8** Influence of water type on number of leaves of tomato, carrot, and bean after 37 days. \* denotes significant differences ( $p < 0.05$ ) between the values of NB treatment groups and control group of the same kind of plants.



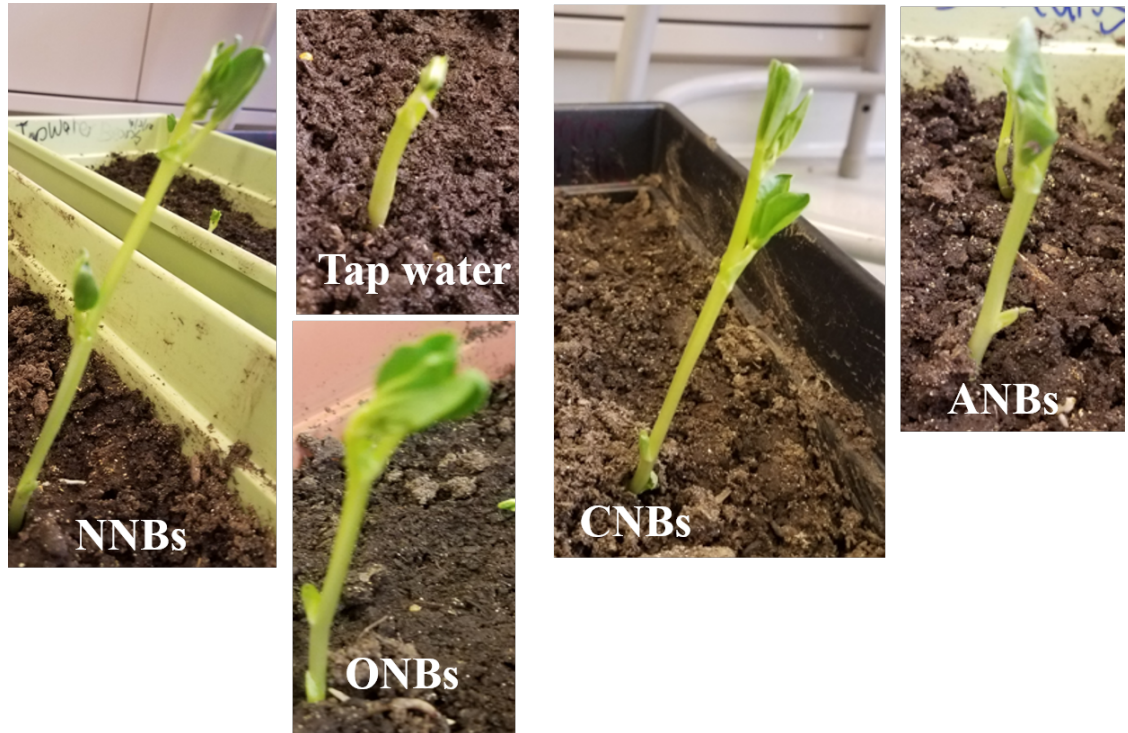


**Figure 4.9** Growth of beans taken after the first week of the test.

The effect of NBs on the stem length and diameter is demonstrated in **Figure 4.10** ( $p < 0.05$ ). Similar to the results of the leaf number, some of the results show that stem length and diameter were both increased by NBs. However, ANBs appeared to inhibit the growth of stem length for bean and tomato after 30 days compared to tap water. Stem length exhibited distinct time-dependent growth (left column of **Figure 4.10**). However, stem diameter did not change with exposure time and also the effect of NBs varied on three types of vegetables. For example, for bean's stem diameter, NNBs promoted its growth and CNBs/ONBs' effects were negligible, whereas ANBs had an inhibitory effect. For tomato, the stem diameter was considerably increased by ONBs, NNBs, and CNBs.

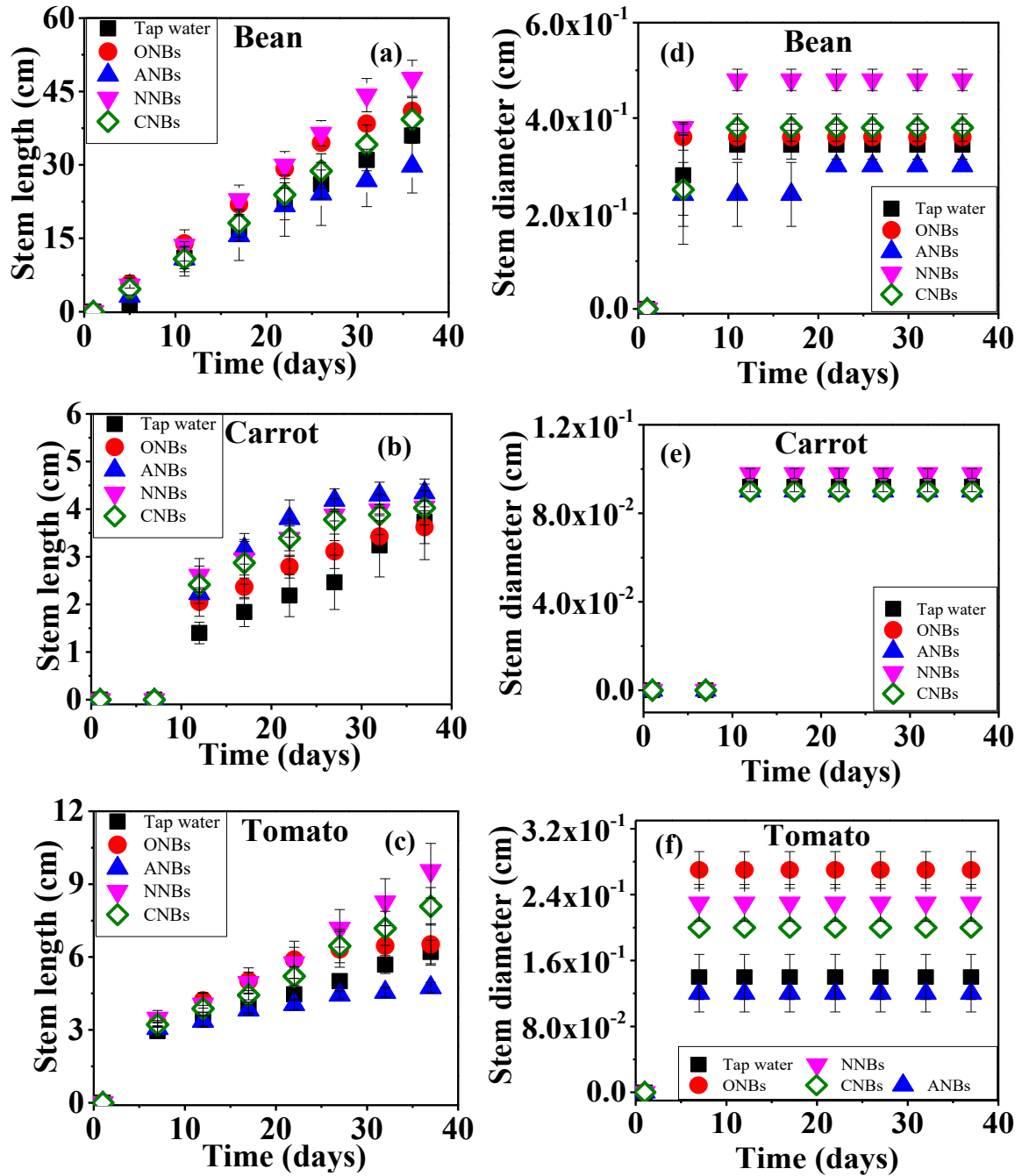


**Figure 4.10** Effect of different types of NBs on stem length of bean (a), carrot (b), and tomato (c) and stem diameter of bean (d), carrot (e), and tomato (f).

**Figure 4.11(a-c)** indicate that there was no significant difference for the leaves length of beans and carrots watered by NBs and tap water (except tomato). **Figure 4.11(d-**

e) also show NNBs' promotion effect on the leaf width of beans and carrots compared to control group with tap water ( $p < 0.05$ ), whereas other NBs made no clear differences. For tomato, its leaf length and width were both enhanced by NNBs water, but inhibited by ANBs. Our results are inconsistent with a previous study that showed ANBs significantly promoted the height, length of leaves and aerial fresh weight of *Brassica campestris*.<sup>12</sup> **Figure 4.12** shows that tomatoes with submersion to CNBs, NNBs and ONBs had bigger leaves than those with tap water.

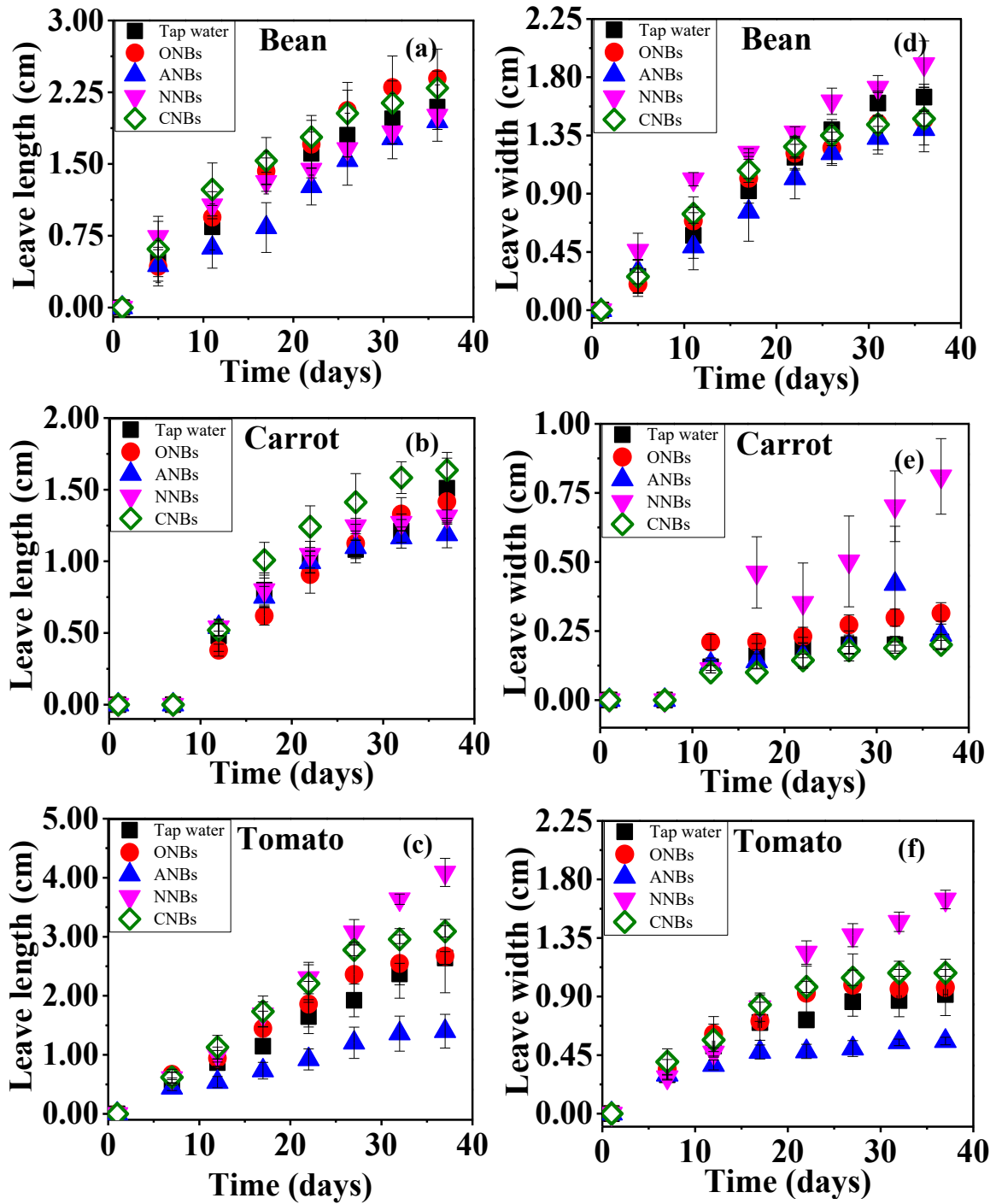


**Figure 4.11** Effect of different types of NBs on leaves length of bean (a), carrot (b), and tomato (c); and leaves width of bean (d), carrot (e), and tomato (f).

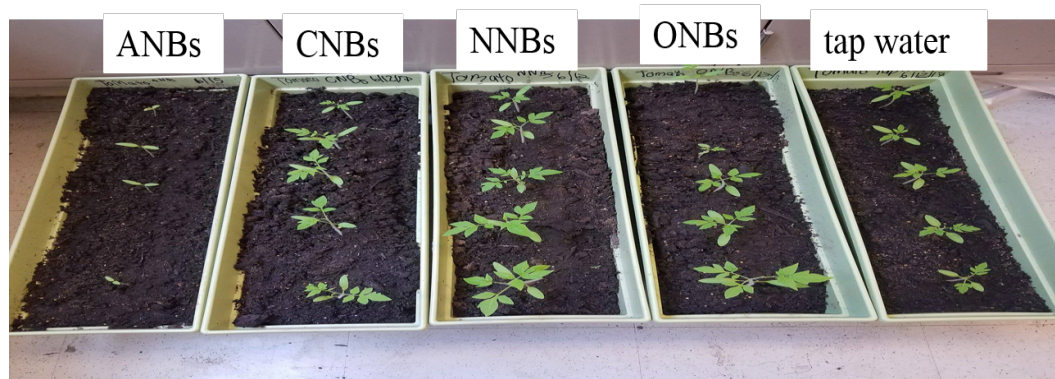


**Figure 4.12** Photos of tomato leaves after the same amount and frequency of watering by NBs water and tap water.

#### 4.3.4 ROS Generation by NBs and Dissolved Oxygen Measurement

The ultrasound could accelerate the aggregation process of NBs in an aqueous solution and promote collapse and ROS generation.<sup>345</sup> We measured the  $\bullet\text{OH}$  radicals in the water saturated with NBs under different sonication time. Without sonication, the PL intensity of different NB solutions is similar with the control group, indicating that terephthalic acid could self-decompose and there were no significant or detectable amounts of ROS in NB waters without sonication. **Figure 4.13** reveals that  $\bullet\text{OH}$  radicals were produced in the NBs water, and both ONBs and ANBs generated considerable amounts of  $\bullet\text{OH}$  radicals. NNBs seemed to quench some radical formation resulted from the sonication, which produced some  $\bullet\text{OH}$  radicals under sonication. CNBs did not produce considerable levels of  $\bullet\text{OH}$  radicals in the solution under the sonication.

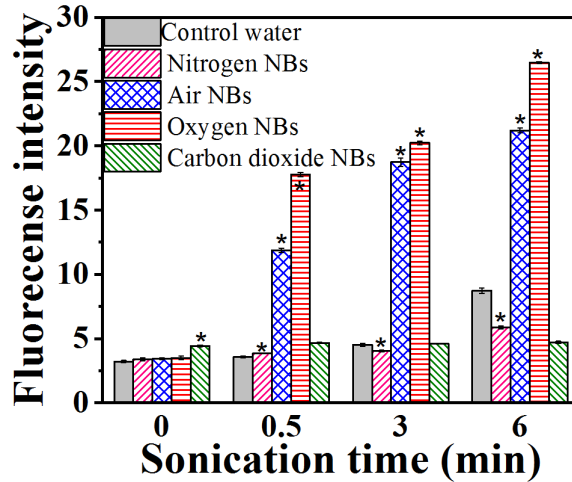


**Figure 4.13** Fluorescence intensity of different NBs water under sonication (100 W). \* denotes significant differences ( $p < 0.05$ ) between the values of NB groups and control group under same sonication time.

**Figure 4.14** shows the changes of dissolved oxygen (DO) levels in water that was saturated with different kinds of NBs and tap water. ANBs water had almost the same DO concentration ( $8.7 \text{ mg}\cdot\text{L}^{-1}$  on average) with tap water. NNBs and CNBs reduced dissolved oxygen levels below the level in tap water. The dissolved oxygen level in ONBs suspension progressively reduced from  $41.8$  to  $15.0 \text{ mg}\cdot\text{L}^{-1}$ , whereas the level of dissolved oxygen increased in the water suspension of NNBs and CNBs, probably due to oxygen gas transfer from the ambient air. The water was re-spiked with NBs every three days, which replenished DO in ONBs suspension from  $15.0$  to  $41.8 \text{ mg}\cdot\text{L}^{-1}$ .

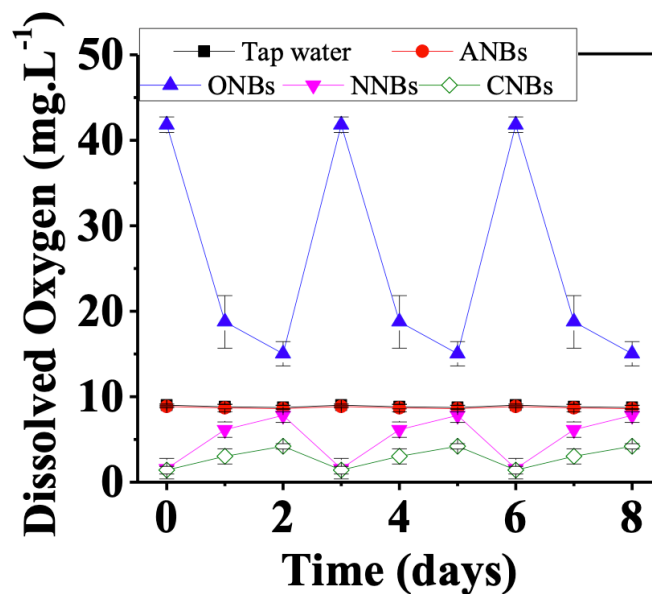


**Figure 4.14** The changes of dissolved oxygen levels in water suspension of different NBs.

## 4.4 Discussion

### 4.4.1 ROS Effects on Germination and Plant Growth

As ROS is one of the activation agents involved in cell wall loosening and cell elongation,<sup>48</sup> the continuous supply of ROS by NBs may sustain a long-lasting stimulation of living organisms and thus promotes plant growth.<sup>47</sup> Shu Liu et al. compared the physiological promotion effects of ONB water and H<sub>2</sub>O<sub>2</sub> solutions,<sup>47</sup> indicating that the oxidative capacity of ONBs water was equivalent to 0.5 mM H<sub>2</sub>O<sub>2</sub> and the oxidative capacity of gas-mixture NBs water was equivalent to 0.3 mM H<sub>2</sub>O<sub>2</sub>. ONB water and equivalent concentration H<sub>2</sub>O<sub>2</sub> solutions exhibited a similar effect in promoting the germination rate of barley seeds.<sup>47</sup> Additionally, NB water was shown to induce the expression of genes related to cell division and cell expansion.<sup>48</sup>

In the past, ROS production in seeds has been widely regarded as a symptom of oxidative stress that potentially lead to deleterious consequences such as cell death and cell

damage (e.g., oxidative degradation of lipids, proteins, and nucleic acid).<sup>346</sup> Research in recent decades, however, has highlighted new roles for ROS as important physiological regulators of cellular signaling pathways.<sup>49</sup> Additionally, both endogenous and exogenous sources contribute to the formation of intracellular ROS.<sup>347</sup> Owusu-Ansah and Banerjee discovered that moderately high ROS level in the progenitor population sensitizes them to differentiation, and establishes a signalling role for ROS in the regulation of hematopoietic cell fate.<sup>348,349</sup> Bailly et al. suggested a concept of the “oxidative window for germination”,<sup>350</sup> a critical range of ROS level at which the occurrence of the cellular events associated with germination is optimal. As reported previously,<sup>350</sup> a low level of ROS during imbibition is inhibitory to germination and may result in decreased antimicrobial defense. A high level of ROS could destroy cells and produce pathological effects.<sup>351, 352</sup> The amount of ROS produced in the NB water could be tuned to match the range of “oxidative window”,<sup>47</sup> depending on specific types of NBs (pure oxygen or oxygen mixture with air).<sup>347</sup> Although ROS such as  $\bullet\text{OH}$  has a short lifetime, NB water may be able to yield a constant submicromolar level of  $\bullet\text{OH}$ ,<sup>47</sup> which substantially enhances germination and plant growth by NBs.

In our research, ONBs generated a considerable amount of ROS and ONBs did not significantly promote the germination of carrot seeds. However, ONBs had a promotion effect on tomato's growth, which indicates the ROS effect could be plant specific. A previous study revealed that the oxidative window for carrot seeds is narrow and the amount of exogenous  $\bullet\text{OH}$  produced by ONBs could be above the toxic threshold of carrot seeds,<sup>49</sup> which is why ONBs had no obvious promotion on carrot sees. Meanwhile, though NNBs only generated a small amount of ROS, it significantly promoted seed germination



for all three kinds of seeds, which could be related to not only the proper ROS but also the possible increased nitrogen accessibility to plants.

#### **4.4.2 Effects of the Growth Elements Delivered by NBs**

Nitrogen and carbon, as key elements of biomass growth, have the profound effect on germination rate, plant growth and properties.<sup>353, 354</sup> Injecting the solution of NNBs could provide more accessibility to N<sub>2</sub> and enhance the efficiency of molecular nitrogen fixation by diazotrophs or nitrogen-fixing organisms,<sup>355</sup> which convert N<sub>2</sub> to ammonia by nitrogenase and thus promote seed germination or plant growth.<sup>356, 357</sup> Thus, NNBs or nanobubble technologies may hold the potential to promote the plant's element absorption and utilization efficiency without secondary pollution.

Oxygen is extremely important for nutrient absorption in plants as oxygen is responsible for transporting nutrients across the cell wall and into the roots of the plant. As more oxygen is absorbed into the root, nutrient absorption will be improved. The root of the crop need enough oxygen to sustain own metabolism and the whole plant growth.<sup>358</sup> Root hypoxia can lead to the weakening of the root respiration, which may shift from aerobic to anaerobic and decrease the root growth, ion transport, and root fluid flow. Therefore, consistent with the previous research,<sup>52</sup> we found that ONBs increased the lettuce and carrot germination, probably because ONBs supports plant root's breath.<sup>359</sup> By contrast, ANBs have substantially different properties from NNBs or ONBs, which could explain the resulted different phytoplankton effects. For example, ANBs has a different ionization energy than NNBs, as well as different surface charges and zeta potentials in aqueous solutions. For example, the ionization energy of nitrogen is 14.5 eV, compared to 34 eV for air.<sup>360</sup> Thus, NNBs has higher ZPs compared to ANBs.<sup>253</sup> High ZPs of NNBs

would enhance their ability to absorb the positively charged plant nutrient ions and promote the plant growth.

## CHAPTER 5

### CONCLUSION AND OUTLOOK

The presented study in Chapter 2 aims to unravel the internal pressures of NBs in water and provide new insights into the colloidal stability mechanisms of NBs. The dependence of bubble sizes and mechanical properties in water on the internal gas pressure and water temperatures were analyzed using experimental approaches and two independent models based on colloidal force balance and contact mechanics. The colloidal force balance model was derived from the Young-Laplace equation and correctly interpreted the effects of multiple factors (e.g., surface tension and surface charge repulsion) on the NBs' stability, in addition to the Laplace pressure in the classical Young-Laplace equation. The experimental measurement and model prediction both revealed the bubble size decreases at high injection or internal gas pressures. The model further implies that NBs elicit much higher internal pressures (120~240 psi) than the injection gas pressures (60-80 psi). Unlike the sensitive impacts of internal pressures, the zeta potential of NBs was not found to affect bubble size or distribution in our previous study,<sup>361</sup> which matches the model prediction. Furthermore, this study presents another contact mechanics model that employs AFM to directly probe the Young's modulus of NBs and further validated the measured and predicted internal pressures that are 2~3 times of the injection pressure.

A combined AFM-SECM technique which enabled high-resolution multimodal imaging, has been elaborated in the Chapter 3. This technique allows for topography to be mapped simultaneously with the SECM current collected or mapped on single nanobubbles. Experiments were performed using commercial probes batch-fabricated by Bruker Company. These probes were designed to provide chemical compatibility with a wide

range of electrochemical environments, electrochemical performance, mechanical stability, and multiple-cycle handling.<sup>71</sup> However, the stability and durability of the AFM-SECM are critical for the measurement of the electrochemical information with reliable and high resolution.

Moreover, sample preparation is very important as well since the solid particles have to be immobilized on the substrate completely so that particles do not detach during the imaging process. In addition, to scan or probe electrochemical or electrical properties of sample surfaces (e.g., electrode), the binding between samples and substrates needs to ensure the electrical conductivity. Overall, we demonstrated that AFM-SECM enables high-resolution imaging of oxygen NBs. Clearly, this AFM-SECM technique is anticipated to play important roles in interfacial electrochemical analysis and will have broad applications in different research fields, such as material science, chemistry, and life science.<sup>309, 319</sup>

In the agricultural application, nitrogen NBs showed a considerable promotion in both seeds germination and plant growth for all species in our experiments, similar with oxygen NBs. According to photoluminescence results, different NBs had different ROS generation abilities, which provide a partial explanation for the promotion on seeds germination. Additionally, NBs may more effectively deliver nutrients (e.g., nitrogen or oxygen) to plants or to nitrogen-fixer in roots environment due to the high surface area and mass diffusion rates. Clearly, we speculated that nitrogen or oxygen exert different mechanisms of plant growth enhancement. For instance, enhanced nitrogen delivery might be the governing factor for nitrogen NBs, while oxygen NBs may play a different role such as enhancing the activity of aerobic root microorganisms and indirectly promote plant

growth. The effects of NBs vary slightly with the types of seeds or plants, which deserves future studies. Moreover, the potential applications of NBs may not be limited to plant growth promotion and agriculture, but also applicable to other chemical or industrial processes such as phytoremediation as an efficient, green and cost-effective approach to boost up plant growth for pollution removal or remediation.

## REFERENCES

1. Hans-Jürgen Butt; Brunero Cappella; Michael Kappl, Force measurements with the atomic force microscope: Technique, interpretation and applications. *Surface Science Reports* **2005**, *59*, 1-152.
2. Tatek Temesgen; Thi Thuy Bui; Mooyoung Han; Tschung-il Kim; Hyunju Park, Micro and nanobubble technologies as a new horizon for water-treatment techniques: A review. *Advances in Colloid and Interface Science* **2017**, *246*, 40-51.
3. Muidh Alheshibri; Jing Qian; Marie Jehannin; Vincent SJ Craig, A history of nanobubbles. *Langmuir* **2016**, *32*, 11086-11100.
4. Guangming Liu; Zhihua Wu; Vincent SJ Craig, Cleaning of protein-coated surfaces using nanobubbles: an investigation using a quartz crystal microbalance. *The Journal of Physical Chemistry C* **2008**, *112*, 16748-16753.
5. Aliasghar Ghadimkhani; Wen Zhang; Taha Marhaba, Ceramic membrane defouling (cleaning) by air Nano Bubbles. *Chemosphere* **2016**, *146*, 379-384.
6. Fernanda Yumi Ushikubo; Takuro Furukawa; Ryou Nakagawa; Masatoshi Enari; Yoshio Makino; Yoshinori Kawagoe; Takeo Shiina; Seiichi Oshita, Evidence of the existence and the stability of nano-bubbles in water. *Colloids and Surfaces A: Physicochemical and Engineering Aspects* **2010**, *361*, 31-37.
7. Wallace W Bowley; Graeme L Hammond, Controlling factors for oxygen transfer through bubbles. *Industrial & Engineering Chemistry Process Design and Development* **1978**, *17*, 2-8.
8. Ashutosh Agarwal; Wun Jern Ng; Yu Liu, Principle and applications of microbubble and nanobubble technology for water treatment. *Chemosphere* **2011**, *84*, 1175-1180.
9. Zhonggao Gao; Anne M Kennedy; Douglas A Christensen; Natalya Y Rapoport, Drug-loaded nano/microbubbles for combining ultrasonography and targeted chemotherapy. *Ultrasonics* **2008**, *48*, 260-270.
10. Joachim Dzubiel, Explicit and implicit modeling of nanobubbles in hydrophobic confinement. *Anais da Academia Brasileira de Ciências* **2010**, *82*, 3-12.
11. Hiroya Ishikawa; Mitsuya Shimoda; Akiyoshi Yonekura; Yutaka Osajima, Inactivation of Enzymes and Decomposition of  $\alpha$ -Helix Structure by Supercritical Carbon Dioxide Microbubble Method. *Journal of Agricultural and Food Chemistry* **1996**, *44*, 2646-2649.

12. Kosuke Ebina; Kenrin Shi; Makoto Hirao; Jun Hashimoto; Yoshitaka Kawato; Shoichi Kaneshiro; Tokimitsu Morimoto; Kota Koizumi; Hideki Yoshikawa, Oxygen and air nanobubble water solution promote the growth of plants, fishes, and mice. *PLoS One* **2013**, *8*, e65339.
13. Yoshihisa Kurita; Ikuo Chiba; Akihiro Kijima, Physical eradication of small planktonic crustaceans from aquaculture tanks with cavitation treatment. *Aquaculture International* **2017**, *25*, 2127-2133.
14. Pan Li; Masayoshi Takahashi; Kaneo Chiba, Enhanced free-radical generation by shrinking microbubbles using a copper catalyst. *Chemosphere* **2009**, *77*, 1157-1160.
15. Masayoshi Takahashi; Taro Kawamura; Yoshitaka Yamamoto; Hirofumi Ohnari; Shouzou Himuro; Hideaki Shakutsui, Effect of shrinking microbubble on gas hydrate formation. *The Journal of Physical Chemistry B* **2003**, *107*, 2171-2173.
16. Masayoshi Takahashi; Kaneo Chiba; Pan Li, Free-radical generation from collapsing microbubbles in the absence of a dynamic stimulus. *The Journal of Physical Chemistry B* **2007**, *111*, 1343-1347.
17. H Ikeura; F Kobayashi; M Tamaki, Ozone microbubble treatment at various water temperatures for the removal of residual pesticides with negligible effects on the physical properties of lettuce and cherry tomatoes. *Journal of Food Science* **2013**, *78*.
18. H Ikeura; F Kobayashi; M Tamaki, Removal of residual pesticide, fenitrothion, in vegetables by using ozone microbubbles generated by different methods. *Journal of Food Engineering* **2011**, *103*, 345-349.
19. Xikui Wang; Jingang Wang; Peiquan Guo; Weilin Guo; Guoliang Li, Chemical effect of swirling jet-induced cavitation: Degradation of rhodamine B in aqueous solution. *Ultrasonics Sonochemistry* **2008**, *15*, 357-363.
20. Kenneth M Kalumuck; Georges L Chahine, The use of cavitating jets to oxidize organic compounds in water. *Journal of Fluids Engineering* **2000**, *122*, 465-470.
21. Xikui Wang; Yong Zhang, Degradation of alachlor in aqueous solution by using hydrodynamic cavitation. *Journal of Hazardous Materials* **2009**, *161*, 202-207.
22. Wayne W Carmichael; Gregory L Boyer, Health impacts from cyanobacteria harmful algae blooms: Implications for the North American Great Lakes. *Harmful Algae* **2016**, *54*, 194-212.
23. Mohammad Hadi Dehghani, Removal of cyanobacterial and algal cells from water by ultrasonic waves — A review. *Journal of Molecular Liquids* **2016**, *222*, 1109-1114.

24. John R Jones; Roger W Bachmann, Prediction of phosphorus and chlorophyll levels in lakes. *Water Pollution Control Federation* **1976**, 2176-2182.
25. Saad Y. Jasim; Jayaprakash Saththasivam, Advanced oxidation processes to remove cyanotoxins in water. *Desalination* **2016**.
26. Beom Sik Kang; Chi-Yong Eom; Wonduck Kim; Pyoung il Kim; Sun Yi Ju; Jaewon Ryu; Gui Hwan Han; Jeong-II Oh; Hoon Cho; Seung Ho Baek; Gueeda Kim; Minju Kim; Jaekyung Hyun; EonSeon Jin; Si Wouk Kim, Construction of target-specific virus-like particles for the delivery of algicidal compounds to harmful algae. *Environmental Microbiology* **2015**, *17*, 1463-1474.
27. Zhou Fang; Lei Wang; Xingya Wang; Limin Zhou; Shuo Wang; Zhenglei Zou; Renzhong Tai; Lijuan Zhang; Jun Hu, Formation and stability of surface/bulk nanobubbles produced by decompression at lower gas concentration. *The Journal of Physical Chemistry C* **2018**, *122*, 22418-22423.
28. Hugh Turrall; Mark Svendsen; Jean Marc Faures, Investing in irrigation: Reviewing the past and looking to the future. *Agricultural Water Management* **2010**, *97*, 551-560.
29. Alice Newton; John Icely; Sonia Cristina; Ana Brito; Ana Cristina Cardoso; Franciscus Colijn; Simona Dalla Riva; Flemming Gertz; Jens Wuergler Hansen; Marianne Holmer, An overview of ecological status, vulnerability and future perspectives of European large shallow, semi-enclosed coastal systems, lagoons and transitional waters. *Estuarine, Coastal and Shelf Science* **2014**, *140*, 95-122.
30. Md Shahidul Islam; Masaru Tanaka, Impacts of pollution on coastal and marine ecosystems including coastal and marine fisheries and approach for management: a review and synthesis. *Marine Pollution Bulletin* **2004**, *48*, 624-649.
31. Robert J Orth; Tim JB Carruthers; William C Dennison; Carlos M Duarte; James W Fourqurean; Kenneth L Heck; A Randall Hughes; Gary A Kendrick; W Judson Kenworthy; Suzanne Olyarnik, A global crisis for seagrass ecosystems. *Bioscience* **2006**, *56*, 987-996.
32. Frederick T Short; Beth Polidoro; Suzanne R Livingstone; Kent E Carpenter; Salomão Bandeira; Japar Sidik Bujang; Hilconida P Calumpang; Tim JB Carruthers; Robert G Coles; William C Dennison, Extinction risk assessment of the world's seagrass species. *Biological Conservation* **2011**, *144*, 1961-1971.
33. Michelle Waycott; Carlos M Duarte; Tim JB Carruthers; Robert J Orth; William C Dennison; Suzanne Olyarnik; Ainsley Calladine; James W Fourqurean; Kenneth L Heck; A Randall Hughes, Accelerating loss of seagrasses across the globe threatens coastal ecosystems. *Proceedings of the National Academy of Sciences* **2009**, *106*, 12377-12381.



34. Noël J Diepens; Evelyne Buffan-Dubau; Hélène Budzinski; Jean Kallerhoff; Georges Merlina; Jérôme Silvestre; Isabelle Auby; Nathalie Tapie; Arnaud Elger, Toxicity effects of an environmental realistic herbicide mixture on the seagrass *Zostera noltei*. *Environmental Pollution* **2017**, *222*, 393-403.
35. J. W. Knox; M. G. Kay; E. K. Weatherhead, Water regulation, crop production, and agricultural water management—Understanding farmer perspectives on irrigation efficiency. *Agricultural Water Management* **2012**, *108*, 3-8.
36. Hedley, C. B. and Knox, J. W. and Raine, S. R. and Smith, R. Water: advanced irrigation technologies. *Encyclopedia of Agriculture and Food Systems*, **2014**, 378-406.
37. World Health Organization, Food and Agriculture Organization. Diet, nutrition and the Prevention of chronic diseases. *Report of a Joint WHO/FAO Expert Consultation* Geneva, **2003**, 147-149.
38. Petra Döll, Impact of Climate Change and Variability on Irrigation Requirements: A Global Perspective. *Climatic Change* **2002**, *54*, 269-293.
39. David Molden, Comprehensive assessment of water management in agriculture. Water for food, water for life: a comprehensive assessment of water management in agriculture. *London: Earthscan and Colombo: International Water Management Institute* **2007**.
40. Charlotte de Fraiture; Dennis Wichelns, Satisfying future water demands for agriculture. *Agricultural Water Management* **2010**, *97*, 502-511.
41. A. Daccache; J. W. Knox; E. K. Weatherhead; A. Daneshkhah; T. M. Hess, Implementing precision irrigation in a humid climate – Recent experiences and on-going challenges. *Agricultural Water Management* **2015**, *147*, 135-143.
42. Yost M. A.; Kitchen N. R.; Sudduth K. A.; Sadler E. J.; Drummond S. T.; Volkmann M. R., Long-term impact of a precision agriculture system on grain crop production. *Precision Agriculture* **2017**, *18*, 823-842.
43. Corwin D. L.; Lesch S. M., Apparent soil electrical conductivity measurements in agriculture. *Computers and Electronics in Agriculture* **2005**, *46*, 11-43.
44. Raphael A. Viscarra Rossel; Johan Bouma, Soil sensing: A new paradigm for agriculture. *Agricultural Systems* **2016**, *148*, 71-74.
45. Hideki Tsuge, *Micro-and Nanobubbles: Fundamentals and Applications*. CRC Press: 2014. Boca Raton, FL, Jenny Stanford Publishing

46. Kosaku Kurata; Hiroyasu Taniguchi; Takanobu Fukunaga; Junpei Matsuda; Hidehiko Higaki, Development of a compact microbubble generator and its usefulness for three-dimensional osteoblastic cell culture. *Journal of Biomechanical Science and Engineering* **2007**, *2*, 166-177.
47. Shu Liu; Seiichi Oshita; Yoshio Makino; Qunhui Wang; Yoshinori Kawagoe; Tsutomu Uchida, Oxidative capacity of nanobubbles and its effect on seed germination. *ACS Sustainable Chemistry and Engineering* **2015**, *4*, 1347-1353.
48. Shu Liu; Seiichi Oshita; Saneyuki Kawabata; Dang Quoc Thuyet, Nanobubble water's promotion effect of barley (*hordeum vulgare* l.) sprouts supported by rna-seq analysis. *Langmuir* **2017**, *33*, 12478-12486.
49. Shu Liu; Seiichi Oshita; Saneyuki Kawabata; Yoshio Makino; Takahiko Yoshimoto, Identification of ROS produced by nanobubbles and their positive and negative effects on vegetable seed germination. *Langmuir* **2016**, *32*, 11295-11302.
50. Shu Liu; Yoshinori Kawagoe; Yoshio Makino; Seiichi Oshita, Effects of nanobubbles on the physicochemical properties of water: The basis for peculiar properties of water containing nanobubbles. *Chemical Engineering Science* **2013**, *93*, 250-256.
51. Park JS; Ohashi K; Kurata K; Lee JW, Promotion of lettuce growth by application of microbubbles in nutrient solution using different rates of electrical conductivity and under periodic intermittent generation in a deep flow technique culture system. *European Journal of Horticultural Science* **2010**, 198-203.
52. Jong-Seok Park; Kenji Kurata, Application of microbubbles to hydroponics solution promotes lettuce growth. *Hort Technology* **2009**, *19*, 212-215.
53. Kazunori Minamikawa; Masayoshi Takahashi; Tomoyuki Makino; Kanako Tago; Masahito Hayatsu, Irrigation with oxygen-nanobubble water can reduce methane emission and arsenic dissolution in a flooded rice paddy. *Environmental Research Letters* **2015**, *10*, 084012.
54. Dilfuza Egamberdieva; Faina Kamilova; Shamil Validov; Laziza Gafurova; Zulfiya Kucharova; Ben Lugtenberg, High incidence of plant growth-stimulating bacteria associated with the rhizosphere of wheat grown on salinated soil in Uzbekistan. *Environmental Microbiology* **2008**, *10*, 1-9.
55. Peter A Bron; Peter Van Baarlen; Michiel Kleerebezem, Emerging molecular insights into the interaction between probiotics and the host intestinal mucosa. *Nature Reviews Microbiology* **2012**, *10*, 66.
56. HAJ Hoitink; MJ Boehm, Biocontrol within the context of soil microbial communities: a substrate-dependent phenomenon. *Annual Review of Phytopathology* **1999**, *37*, 427-446.

57. Noémie Elgrishi; Kelley J. Rountree; Brian D. McCarthy; Eric S. Rountree; Thomas T. Eisenhart; Jillian L. Dempsey, A practical beginner's guide to cyclic voltammetry. *Journal of Chemical Education* **2018**, *95*, 197-206.
58. Jaroslav Heyrovský; Jaroslav Kůta, *Principles of polarography*. New York, NY, Elsevier: 2013.
59. Tiziano Bellezze; Giampaolo Giuliani; Annamaria Viceré; Gabriella Roventi, Study of stainless steels corrosion in a strong acid mixture. Part 2: anodic selective dissolution, weight loss and electrochemical impedance spectroscopy tests. *Corrosion Science* **2018**, *130*, 12-21.
60. Ehsani A; Mahjani MG; Hosseini M; Safari R; Moshrefi R; Mohammad Shiri H, Evaluation of *Thymus vulgaris* plant extract as an eco-friendly corrosion inhibitor for stainless steel 304 in acidic solution by means of electrochemical impedance spectroscopy, electrochemical noise analysis and density functional theory. *Journal of Colloid and Interface Science* **2017**, *490*, 444-451.
61. Shigeru Amemiya; Allen J. Bard; Fu-Ren F. Fan; Michael V. Mirkin; Patrick R. Unwin, Scanning Electrochemical Microscopy. *Annual Review of Analytical Chemistry* **2008**, *1*, 95-131.
62. Andrew J. Wain, Scanning electrochemical microscopy for combinatorial screening applications: A mini-review. *Electrochemistry Communications* **2014**, *46*, 9-12.
63. Cynthia G. Zoski, Review—Advances in Scanning Electrochemical Microscopy (SECM). *Journal of The Electrochemical Society* **2016**, *163*, H3088-H3100.
64. Stefan Bergner; Preety Vatsyayan; Frank-Michael Matysik, Recent advances in high resolution scanning electrochemical microscopy of living cells—a review. *Analytica Chimica Acta* **2013**, *775*, 1-13.
65. Michael A. O'Connell; Andrew J. Wain, Combined electrochemical-topographical imaging: a critical review. *Analytical Methods* **2015**, *7*, 6983-6999.
66. Allen J Bard; Larry R Faulkner; Johna Leddy; Cynthia G Zoski, *Electrochemical methods: fundamentals and applications*. New York, NY, Wiley: 1980; Vol. 2.
67. Michael V Mirkin; Wojciech Nogala; Jeyavel Velmurugan; Yixian Wang, Scanning electrochemical microscopy in the 21st century. Update 1: five years after. *Physical Chemistry Chemical Physics* **2011**, *13*, 21196-21212.
68. Allen J. Bard; Fu Ren F. Fan; Juhyoun Kwak; Ovadia Lev, Scanning electrochemical microscopy. Introduction and principles. *Analytical Chemistry* **1989**, *61*, 132-138.

69. Royce C Engstrom; Christine M Pharr, Scanning electrochemical microscopy. *Analytical Chemistry* **1989**, *61*, 1099A-1104A.
70. David Polcari; Philippe Dauphin-Ducharme; Janine Mauzeroll, Scanning electrochemical microscopy: a comprehensive review of experimental parameters from 1989 to 2015. *Chemical Reviews* **2016**, *116*, 13234-13278.
71. Michael R Nellist; Yikai Chen; Andreas Mark; Sebastian Gödrich; Christian Stelling; Jingjing Jiang; Rakesh Poddar; Chunzeng Li; Ravi Kumar; Georg Papastavrou, Atomic force microscopy with nanoelectrode tips for high resolution electrochemical, nanoadhesion and nanoelectrical imaging. *Nanotechnology* **2017**, *28*, 095711.
72. Anisha N Patel; Christine Kranz, (Multi) functional Atomic Force Microscopy Imaging. *Annual Review of Analytical Chemistry* **2018**.
73. Markus Ludwig; Christine Kranz; Wolfgang Schuhmann; Hermann E Gaub, Topography feedback mechanism for the scanning electrochemical microscope based on hydrodynamic forces between tip and sample. *Review of Scientific Instruments* **1995**, *66*, 2857-2860.
74. Celeste A Morris; Chiao-Chen Chen; Lane A Baker, Transport of redox probes through single pores measured by scanning electrochemical-scanning ion conductance microscopy (SECM-SICM). *Analyst* **2012**, *137*, 2933-2938.
75. Kathrin Eckhard; Wolfgang Schuhmann, Alternating current techniques in scanning electrochemical microscopy (AC-SECM). *Analyst* **2008**, *133*, 1486-1497.
76. Julie V Macpherson; Patrick R Unwin, Combined scanning electrochemical-atomic force microscopy. *Analytical Chemistry* **2000**, *72*, 276-285.
77. Wanyi Fu; Wen Zhang, Hybrid AFM for nanoscale physicochemical characterization: recent development and emerging applications. *Small* **2017**, *13*, 1603525.
78. Arjan P Quist; Ami Chand; Srinivasan Ramachandran; Chiara Daraio; Sungho Jin; Ratnesh Lal, Atomic force microscopy imaging and electrical recording of lipid bilayers supported over microfabricated silicon chip nanopores: Lab-on-a-chip system for lipid membranes and ion channels. *Langmuir* **2007**, *23*, 1375-1380.
79. Hezy Cohen; Claude Noguez; Daniela Ullien; Shirley Daube; Ron Naaman; Danny Porath, Electrical characterization of self-assembled single- and double-stranded DNA monolayers using conductive AFM. *Faraday Discussions* **2006**, *131*, 367-376.

80. Jong Won Chung; Hoichang Yang; Birendra Singh; Hyunsik Moon; Byeong-kwan An; Sang Yoon Lee; Soo Young Park, Single-crystalline organic nanowires with large mobility and strong fluorescence emission: a conductive-AFM and space-charge-limited-current study. *Journal of Materials Chemistry* **2009**, *19*, 5920-5925.
81. Deng-Zhu Guo; Shi-Min Hou; Geng-Min Zhang; Zeng-Quan Xue, Conductance fluctuation and degeneracy in nanocontact between a conductive AFM tip and a granular surface under small-load conditions. *Applied Surface Science* **2006**, *252*, 5149-5157.
82. Rocca E.; Bertrand G.; Rapin C.; Labrune J. C., Inhibition of copper aqueous corrosion by non-toxic linear sodium heptanoate: mechanism and ECAFM study. *Journal of Electroanalytical Chemistry* **2001**, *503*, 133-140.
83. Francesca M. Toma; Jason K. Cooper; Viktoria Kunzelmann; Matthew T. McDowell; Jie Yu; David M. Larson; Nicholas J. Borys; Christine Abelyan; Jeffrey W. Beeman; Kin Man Yu; Jinhui Yang; Le Chen; Matthew R. Shaner; Joshua Spurgeon; Frances A. Houle; Kristin A. Persson; Ian D. Sharp, Mechanistic insights into chemical and photochemical transformations of bismuth vanadate photoanodes. *Nature Communication* **2016**, *7*, 12012-12012.
84. Takashi Kouzeki; Shinya Tatezono; Hisao Yanagi, Electrochromism of orientation-controlled naphthalocyanine thin films. *The Journal of Physical Chemistry* **1996**, *100*, 20097-20102.
85. Yoshiaki Yamaguchi; Masashi Shiota; Yasuhide Nakayama; Nobumitsu Hirai; Shigeta Hara, Combined in situ EC-AFM and CV measurement study on lead electrode for lead-acid batteries. *Journal of Power Sources* **2001**, *93*, 104-111.
86. David J. Comstock; Jeffrey W. Elam; Michael J. Pellin; Mark C. Hersam, Integrated ultramicroelectrode-nanopipet probe for concurrent scanning electrochemical microscopy and scanning ion conductance microscopy. *Analytical Chemistry* **2010**, *82*, 1270-1276.
87. Neil Ebejer; Mathias Schnippering; Alexander W. Colburn; Martin A. Edwards; Patrick R. Unwin, Localized high resolution electrochemistry and multifunctional imaging: scanning electrochemical cell microscopy. *Analytical Chemistry* **2010**, *82*, 9141-9145.
88. Neil Ebejer; Aleix G. Güell; Stanley C. S. Lai; Kim McKelvey; Michael E. Snowden; Patrick R. Unwin, Scanning electrochemical cell microscopy: a versatile technique for nanoscale electrochemistry and functional imaging. *Annual Review of Analytical Chemistry* **2013**, *6*, 329-351.
89. Keisuke Ikehata; Ling Wang-Staley; Xiaoyan Qu; Yuan Li, Treatment of groundwater contaminated with 1, 4-dioxane, tetrahydrofuran, and chlorinated

- volatile organic compounds using advanced oxidation processes. *Ozone: Science and Engineering* **2016**, *38*, 413-424.
90. Melania Reggente; Daniele Passeri; Marco Rossi; Emanuela Tamburri; Maria Letizia Terranova, Electrochemical atomic force microscopy: in situ monitoring of electrochemical processes. *AIP Conference Proceedings* **2017**, *1873*, 020009.
  91. E Ventosa; W Schuhmann, Scanning electrochemical microscopy of Li-ion batteries. *Physical Chemistry Chemical Physics* **2015**, *17*, 28441-28450.
  92. Dan Guo; Guoxin Xie; Jianbin Luo, Mechanical properties of nanoparticles: basics and applications. *Journal of Physics D: Applied Physics* **2013**, *47*, 013001.
  93. Zhuangqun Huang; Peter De Wolf; Rakesh Poddar; Chunzeng Li; Andreas Mark; Michael R Nellist; Yikai Chen; Jingjing Jiang; Georg Papastavrou; Shannon W Boettcher, PeakForce scanning electrochemical microscopy with nanoelectrode probes. *Microscopy Today* **2016**, *24*, 18-25.
  94. Sina S Jamali; Simon E Moulton; Dennis E Tallman; Maria Forsyth; Jan Weber; Gordon G Wallace, Applications of scanning electrochemical microscopy (SECM) for local characterization of AZ31 surface during corrosion in a buffered media. *Corrosion Science* **2014**, *86*, 93-100.
  95. N Esmaceli; J Neshati; I Yavari, Scanning electrochemical microscopy for the investigation of corrosion inhibition of triazino-benzimidazole-2-thiones in hydrochloric acid solution. *Research on Chemical Intermediates* **2016**, *42*, 5339-5351.
  96. Tzu-En Lin; Stefania Rapino; Hubert H Girault; Andreas Lesch, Electrochemical imaging of cells and tissues. *Chemical Science* **2018**, *9*, 4546-4554.
  97. Angelika Holzinger; Charlotte Steinbach; Christine Kranz, Scanning Electrochemical Microscopy (SECM): Fundamentals and Applications in Life Sciences. *Electrochemical Strategies in Detection Science* **2015**, 125.
  98. Qin hao Zhang; Zhenni Ye; Zejie Zhu; Xiaoyan Liu; Jianqing Zhang; Fahe Cao, Separation and kinetic study of iron corrosion in acidic solution via a modified tip generation/substrate collection mode by SECM. *Corrosion Science* **2018**, *139*, 403-409.
  99. Qin hao Zhang; Pan Liu; Zejie Zhu; Zhenni Ye; Jianqing Zhang; Fahe Cao; Xiaogang Li, Quantitative analysis of the polarization behavior of iron in an aerated acidic solution using SECM. *Electrochemistry Communications* **2018**, *93*, 143-147.
  100. Jose L Fernandez; Allen J Bard, Scanning electrochemical microscopy. 47. imaging electrocatalytic activity for oxygen reduction in an acidic medium by the

- tip generation– substrate collection mode. *Analytical Chemistry* **2003**, *75*, 2967-2974.
101. Kathrin Eckhard; Xingxing Chen; Florin Turcu; Wolfgang Schuhmann, Redox competition mode of scanning electrochemical microscopy (RC-SECM) for visualisation of local catalytic activity. *Physical Chemistry Chemical Physics* **2006**, *8*, 5359-5365.
  102. Marques AG; Izquierdo J; Souto RM; Simões AM, SECM imaging of the cut edge corrosion of galvanized steel as a function of pH. *Electrochimica Acta* **2015**, *153*, 238-245.
  103. Michaela Nebel; Stefanie Grützke; Nizam Diab; Albert Schulte; Wolfgang Schuhmann, Microelectrochemical visualization of oxygen consumption of single living cells. *Faraday Discussions* **2013**, *164*, 19-32.
  104. Vikram Singh; Aarti Tiwari; Tharamani C Nagaiah, Facet-controlled morphology of cobalt disulfide towards enhanced oxygen reduction reaction. *Journal of Materials Chemistry A* **2018**.
  105. Aarti Tiwari; Vikram Singh; Tharamani C Nagaiah, Tuning the MnWO<sub>4</sub> morphology and its electrocatalytic activity towards oxygen reduction reaction. *Journal of Materials Chemistry A* **2018**, *6*, 2681-2692.
  106. Gunther Wittstock; Malte Burchardt; Sascha E. Pust; Yan Shen; Chuan Zhao, Scanning Electrochemical Microscopy for Direct Imaging of Reaction Rates. *Angewandte Chemie International Edition* **2007**, *46*, 1584-1617.
  107. Jan Clausmeyer; Michaela Nebel; Stefanie Grützke; Yasin U Kayran; Wolfgang Schuhmann, Local Surface Modifications Investigated by Combining Scanning Electrochemical Microscopy and Surface-Enhanced Raman Scattering. *ChemPlusChem* **2018**, *83*, 414-417.
  108. Liang Liu; Daniel Mandler, *Sol–Gel Coatings by Electrochemical Deposition in The Sol-Gel Handbook*, Weinheim, Germany, Wiley-VCH: **2015**.
  109. Jin-He Zhou; Ji-Peng Zhao; Lian-Kui Wu; Ji-Ming Hu, Localized electro-reduction of p-type Cu<sub>2</sub>O by SECM under light irradiation. *Electrochemistry Communications* **2016**, *72*, 171-175.
  110. Stuart AG Evans; Karine Brakha; Martial Billon; Pascal Mailley; Guy Denuault, Scanning electrochemical microscopy (SECM): localized glucose oxidase immobilization via the direct electrochemical microspotting of polypyrrole–biotin films. *Electrochemistry Communications* **2005**, *7*, 135-140.
  111. Emad El-Deen M El-Giar; David O Wipf, Microparticle-based iridium oxide ultramicroelectrodes for pH sensing and imaging. *Journal of Electroanalytical Chemistry* **2007**, *609*, 147-154.

112. Javier Izquierdo; Livia Nagy; Ágnes Varga; Juan J Santana; Géza Nagy; Ricardo M Souto, Spatially resolved measurement of electrochemical activity and pH distributions in corrosion processes by scanning electrochemical microscopy using antimony microelectrode tips. *Electrochimica Acta* **2011**, *56*, 8846-8850.
113. Mara Serrapede; Guy Denuault; Maciej Sosna; Giovanni Luca Pesce; Richard J. Ball, Scanning electrochemical microscopy: using the potentiometric mode of secm to study the mixed potential arising from two independent redox processes. *Analytical Chemistry* **2013**, *85*, 8341-8346.
114. G. Binnig; C. F. Quate; Ch Gerber, Atomic force microscope. *Physical Review Letters* **1986**, *56*, 930-933.
115. Mi Li; Dan Dang; Lianqing Liu; Ning Xi; Yuechao Wang, Atomic force microscopy in characterizing cell mechanics for biomedical applications: A review. *IEEE Transactions on Nanobioscience* **2017**, *16*, 523-540.
116. Nader Jalili; Karthik Laxminarayana, A review of atomic force microscopy imaging systems: application to molecular metrology and biological sciences. *Mechatronics* **2004**, *14*, 907-945.
117. Yves F Dufrêne; Toshio Ando; Ricardo Garcia; David Alsteens; David Martinez-Martin; Andreas Engel; Christoph Gerber; Daniel J Müller, Imaging modes of atomic force microscopy for application in molecular and cell biology. *Nature Nanotechnology* **2017**, *12*, 295.
118. Peter Eaton; Paul West, *Atomic force microscopy*. New York, NY, Oxford university press: **2010**.
119. Bert Voigtländer, Static atomic force microscopy. *Atomic Force Microscopy*, , **2019**; pp 199-208.
120. Victor J Morris; Andrew R Kirby; A Patrick Gunning, Atomic force microscopy for biologists. *World Scientific*: **1999**.
121. Victor Bellitto, *Atomic Force Microscopy: Imaging, Measuring and Manipulating Surfaces at the Atomic Scale*. Rijeka, Croatia, InTech, **2012**.
122. Yoshihiro Kuwahara; Seiichiro Uehara; Yoshikazu Aoki, Surface microtopography of lath-shaped hydrothermal illite by tapping-mode™ and contact-mode AFM. *Clays and Clay Minerals* **1998**, *46*, 574-582.
123. Woosuk Choi; Muhammad Arslan Shehzad; Sanghoon Park; Yongho Seo, Influence of removing PMMA residues on surface of CVD graphene using a contact-mode atomic force microscope. *RSC Advances* **2017**, *7*, 6943-6949.
124. Jiro Kumaki, Observation of polymer chain structures in two-dimensional films by atomic force microscopy. *Polymer Journal* **2016**, *48*, 3.



125. Franz J. Giessibl, Advances in atomic force microscopy. *Reviews of Modern Physics* **2003**, *75*, 949-983.
126. Franz J. Giessibl, Forces and frequency shifts in atomic-resolution dynamic-force microscopy. *Physical Review B* **1997**, *56*, 16010-16015.
127. Franz J. Giessibl; Hartmut Bielefeldt; Stefan Hembacher; Jochen Mannhart, Calculation of the optimal imaging parameters for frequency modulation atomic force microscopy. *Applied Surface Science* **1999**, *140*, 352-357.
128. Chih-Wen Yang; Ing-Shouh Hwang; Yen Fu Chen; Chia Seng Chang; Din Ping Tsai, Imaging of soft matter with tapping-mode atomic force microscopy and non-contact-mode atomic force microscopy. *Nanotechnology* **2007**, *18*, 084009.
129. Ricardo García; Rubén Pérez, Dynamic atomic force microscopy methods. *Surface Science Reports* **2002**, *47*, 197-301.
130. Julie V. Macpherson; Patrick R. Unwin, Noncontact electrochemical imaging with combined scanning electrochemical atomic force microscopy. *Analytical Chemistry* **2001**, *73*, 550-557.
131. Phillip S Dobson; John MR Weaver; Mark N Holder; Patrick R Unwin; Julie V Macpherson, Characterization of batch-microfabricated scanning electrochemical-atomic force microscopy probes. *Analytical Chemistry* **2005**, *77*, 424-434.
132. Raul D Rodriguez; Agnès Anne; Edmond Cambril; Christophe Demaille, Optimized hand fabricated AFM probes for simultaneous topographical and electrochemical tapping mode imaging. *Ultramicroscopy* **2011**, *111*, 973-981.
133. Angelika Kueng; Christine Kranz; Alois Lugstein; Emmerich Bertagnolli; Boris Mizaikoff, Integrated AFM–SECM in tapping mode: simultaneous topographical and electrochemical imaging of enzyme activity. *Angewandte Chemie International Edition* **2003**, *42*, 3238-3240.
134. A. Kueng; C. Kranz; B. Mizaikoff; A. Lugstein; E. Bertagnolli, Combined scanning electrochemical atomic force microscopy for tapping mode imaging. *Applied Physics Letters* **2003**, *82*, 1592-1594.
135. Xin Deng; XingRui Liu; HuiJuan Yan; Dong Wang; LiJun Wan, Morphology and modulus evolution of graphite anode in lithium ion battery: An in situ AFM investigation. *Science China Chemistry* **2014**, *57*, 178-183.
136. David J. Comstock; Jeffrey W. Elam; Michael J. Pellin; Mark C. Hersam, High aspect ratio nanoneedle probes with an integrated electrode at the tip apex. *Review of Scientific Instruments* **2012**, *83*, 113704.
137. Maurizio R Gullo; Patrick LTM Frederix; Terunobu Akiyama; Andreas Engel; Nico F deRoos; Urs Staufer, Characterization of microfabricated probes for

- combined atomic force and high-resolution scanning electrochemical microscopy. *Analytical Chemistry* **2006**, *78*, 5436-5442.
138. David P. Burt; Neil R. Wilson; John M. R. Weaver; Phillip S. Dobson; Julie V. Macpherson, Nanowire Probes for High Resolution Combined Scanning Electrochemical Microscopy – Atomic Force Microscopy. *Nano Letters* **2005**, *5*, 639-643.
  139. Sascha E. Pust; Marc Salomo; Egbert Oesterschulze; Gunther Wittstock, Influence of electrode size and geometry on electrochemical experiments with combined SECM–SFM probes. *Nanotechnology* **2010**, *21*, 105709.
  140. Christine Kranz; Gernot Friedbacher; Boris Mizaikoff; Alois Lugstein; Jürgen Smoliner; Emmerich Bertagnolli, Integrating an ultramicroelectrode in an AFM cantilever: combined technology for enhanced information. *Analytical chemistry* **2001**, *73*, 2491-2500.
  141. Maksymilian A Derylo; Kirstin C Morton; Lane A Baker, Parylene insulated probes for scanning electrochemical-atomic force microscopy. *Langmuir* **2011**, *27*, 13925-13930.
  142. Andrew J Wain; David Cox; Shengqi Zhou; Alan Turnbull, High-aspect ratio needle probes for combined scanning electrochemical microscopy—Atomic force microscopy. *Electrochemistry Communications* **2011**, *13*, 78-81.
  143. Alexander Eifert; Waldemar Smirnov; Stefan Frittmann; Christoph Nebel; Boris Mizaikoff; Christine Kranz, Atomic force microscopy probes with integrated boron doped diamond electrodes: Fabrication and application. *Electrochemistry Communications* **2012**, *25*, 30-34.
  144. Justyna Wiedemair; Nicola Menegazzo; Joel Pikarsky; Karl S Booksh; Boris Mizaikoff; Christine Kranz, Novel electrode materials based on ion beam induced deposition of platinum carbon composites. *Electrochimica Acta* **2010**, *55*, 5725-5732.
  145. Jeremy Abbou; Christophe Demaille; Michel Druet; Jacques Moiroux, Fabrication of submicrometer-sized gold electrodes of controlled geometry for scanning electrochemical-atomic force microscopy. *Analytical Chemistry* **2002**, *74*, 6355-6363.
  146. Jeyavel Velmurugan; Amit Agrawal; Sangmin An; Eric Choudhary; Veronika A Szalai, Fabrication of scanning electrochemical microscopy-atomic force microscopy probes to image surface topography and reactivity at the nanoscale. *Analytical Chemistry* **2017**, *89*, 2687-2691.
  147. Peter Knittel; Boris Mizaikoff; Christine Kranz, Simultaneous nanomechanical and electrochemical mapping: combining peak force tapping atomic force

- microscopy with scanning electrochemical microscopy. *Analytical Chemistry* **2016**, *88*, 6174-6178.
148. Alexander Eifert; Boris Mizaikoff; Christine Kranz, Advanced fabrication process for combined atomic force-scanning electrochemical microscopy (AFM-SECM) probes. *Micron* **2015**, *68*, 27-35.
  149. Phillip S. Dobson; John M. R. Weaver; Mark N. Holder; Patrick R. Unwin; Julie V. Macpherson, Characterization of batch-microfabricated scanning electrochemical-atomic force microscopy probes. *Analytical Chemistry* **2005**, *77*, 424-434.
  150. Kelly Leonhardt; Amra Avdic; Alois Lugstein; Ilya Pobelov; Thomas Wandlowski; Ming Wu; Bernhard Gollas; Guy Denuault, Atomic force microscopy-scanning electrochemical microscopy: influence of tip geometry and insulation defects on diffusion controlled currents at conical electrodes. *Analytical Chemistry* **2011**, *83*, 2971-2977.
  151. Q. Fulian; A. C. Fisher, Computational Electrochemistry: The boundary element method. *The Journal of Physical Chemistry B* **1998**, *102*, 9647-9652.
  152. Oleg Sklyar; Angelika Kueng; Christine Kranz; Boris Mizaikoff; Alois Lugstein; Emmerich Bertagnolli; Gunther Wittstock, Numerical simulation of scanning electrochemical microscopy experiments with frame-shaped integrated atomic force microscopy-secm probes using the boundary element method. *Analytical Chemistry* **2005**, *77*, 764-771.
  153. Phillip S Dobson; John MR Weaver; David P Burt; Mark N Holder; Neil R Wilson; Patrick R Unwin; Julie V Macpherson, Electron beam lithographically-defined scanning electrochemical-atomic force microscopy probes: fabrication method and application to high resolution imaging on heterogeneously active surfaces. *Physical Chemistry Chemical Physics* **2006**, *8*, 3909-3914.
  154. Justyna Wiedemair; Jong-Seok Moon; Felix Reinauer; Boris Mizaikoff; Christine Kranz, Ion beam induced deposition of platinum carbon composite electrodes for combined atomic force microscopy-scanning electrochemical microscopy. *Electrochemistry Communications* **2010**, *12*, 989-991.
  155. P Knittel; MJ Higgins; C Kranz, Nanoscopic polypyrrole AFM-SECM probes enabling force measurements under potential control. *Nanoscale* **2014**, *6*, 2255-2260.
  156. Eva LH Heintz; Christine Kranz; Boris Mizaikoff; H-S Noh; Peter Hesketh; Alois Lugstein; Emmerich Bertagnolli Characterization of parylene coated combined scanning probe tips for in-situ electrochemical and topographical imaging, *IEEE Conference on Nanotechnology*. 2001; pp 346-351.

157. Oleg Sklyar; Angelika Kueng; Christine Kranz; Boris Mizaikoff; Alois Lugstein; Emmerich Bertagnolli; Gunther Wittstock, Numerical simulation of scanning electrochemical microscopy experiments with frame-shaped integrated atomic force microscopy– secm probes using the boundary element method. *Analytical Chemistry* **2005**, *77*, 764-771.
158. Ali Davoodi; Jinshan Pan; Christofer Leygraf; Stefan Norgren, In situ investigation of localized corrosion of aluminum alloys in chloride solution using integrated EC-AFM/SECM techniques. *Electrochemical and Solid-State Letters* **2005**, *8*, B21-B24.
159. P Knittel; O Bibikova; C Kranz, Challenges in nanoelectrochemical and nanomechanical studies of individual anisotropic gold nanoparticles. *Faraday Discussions* **2016**, *193*, 353-369.
160. M Salomo; SE Pust; G Wittstock; E Oesterschulze, Integrated cantilever probes for SECM/AFM characterization of surfaces. *Microelectronic Engineering* **2010**, *87*, 1537-1539.
161. Waldemar Smirnov; Armin Kriele; René Hoffmann; Eugenio Sillero; Jakob Hees; Oliver A Williams; Nianjun Yang; Christine Kranz; Christoph E Nebel, Diamond-modified AFM probes: from diamond nanowires to atomic force microscopy-integrated boron-doped diamond electrodes. *Analytical Chemistry* **2011**, *83*, 4936-4941.
162. Heungjoo Shin; Peter J Hesketh; Boris Mizaikoff; Christine Kranz, Batch fabrication of atomic force microscopy probes with recessed integrated ring microelectrodes at a wafer level. *Analytical Chemistry* **2007**, *79*, 4769-4777.
163. Shin H; Hesketh PJ; Mizaikoff B; Kranz C, Development of wafer-level batch fabrication for combined atomic force–scanning electrochemical microscopy (AFM–SECM) probes. *Sensors and Actuators B: Chemical* **2008**, *134*, 488-495.
164. Kelly Leonhardt; Amra Avdic; Alois Lugstein; Ilya Pobelov; Thomas Wandlowski; Bernhard Gollas; Guy Denuault, Scanning electrochemical microscopy: Diffusion controlled approach curves for conical AFM-SECM tips. *Electrochemistry Communications* **2013**, *27*, 29-33.
165. Julie V Macpherson; Jean-Paul Gueneau de Mussy; Jean-Luc Delplancke, High-resolution electrochemical, electrical, and structural characterization of a dimensionally stable Ti/TiO<sub>2</sub>/Pt electrode. *Journal of The Electrochemical Society* **2002**, *149*, B306-B313.
166. Kai Huang; Agnes Anne; Mohamed Ali Bahri; Christophe Demaille, Probing Individual Redox PEGylated Gold Nanoparticles by Electrochemical–Atomic Force Microscopy. *ACS Nano* **2013**, *7*, 4151-4163.

167. Khalil Chennit; Jorge Trasobares; Agnès Anne; Edmond Cambril; Arnaud Chovin; Nicolas Clément; Christophe Demaille, Electrochemical imaging of dense molecular nanoarrays. *Analytical Chemistry* **2017**, *89*, 11061-11069.
168. Jeremy Abbou; Agnès Anne; Christophe Demaille, Probing the structure and dynamics of end-grafted flexible polymer chain layers by combined atomic force–electrochemical microscopy. cyclic voltammetry within nanometer-thick macromolecular poly (ethylene glycol) layers. *Journal of the American Chemical Society* **2004**, *126*, 10095-10108.
169. Jeremy Abbou; Agnès Anne; Christophe Demaille, Accessing the dynamics of end-grafted flexible polymer chains by atomic force-electrochemical microscopy. Theoretical modeling of the approach curves by the elastic bounded diffusion model and Monte Carlo simulations. Evidence for compression-induced lateral chain escape. *The Journal of Physical Chemistry B* **2006**, *110*, 22664-22675.
170. Agnes Anne; Edmond Cambril; Arnaud Chovin; Christophe Demaille, Touching surface-attached molecules with a microelectrode: mapping the distribution of redox-labeled macromolecules by electrochemical-atomic force microscopy. *Analytical Chemistry* **2010**, *82*, 6353-6362.
171. Agnès Anne; Mohamed Ali Bahri; Arnaud Chovin; Christophe Demaille; Cécilia Taofifenua, Probing the conformation and 2D-distribution of pyrene-terminated redox-labeled poly (ethylene glycol) chains end-adsorbed on HOPG using cyclic voltammetry and atomic force electrochemical microscopy. *Physical Chemistry Chemical Physics* **2014**, *16*, 4642-4652.
172. Achraf Ghorbal; Federico Grisotto; Julienne Charlier; Serge Palacin; Cédric Goyer; Christophe Demaille, Localized electrografting of vinylic monomers on a conducting substrate by means of an integrated electrochemical AFM probe. *ChemPhysChem* **2009**, *10*, 1053-1057.
173. Agnes Anne; Edmond Cambril; Arnaud Chovin; Christophe Demaille; Cédric Goyer, Electrochemical atomic force microscopy using a tip-attached redox mediator for topographic and functional imaging of nanosystems. *ACS Nano* **2009**, *3*, 2927-2940.
174. Agnes Anne; Christophe Demaille; Cédric Goyer, Electrochemical atomic-force microscopy using a tip-attached redox mediator. Proof-of-concept and perspectives for functional probing of nanosystems. *ACS Nano* **2009**, *3*, 819-827.
175. Jingjing Jiang; Zhuangqun Huang; Chengxiang Xiang; Rakesh Poddar; Hans-Joachim Lewerenz; Kimberly M Papadantonakis; Nathan S Lewis; Bruce S Brunnschwig, Nanoelectrical and nanoelectrochemical imaging of pt/p - si and pt/p+ - si electrodes. *ChemSus Chem* **2017**, *10*, 4657-4663.

176. Srikanth Kolagatla; Palaniappan Subramanian; Alex Schechter, Nanoscale mapping of catalytic hotspots on Fe, N-modified HOPG by scanning electrochemical microscopy-atomic force microscopy. *Nanoscale* **2018**, *10*, 6962-6970.
177. Srikanth Kolagatla; Palaniappan Subramanian; Alex Schechter, Catalytic current mapping of oxygen reduction on isolated pt particles by atomic force microscopy-scanning electrochemical microscopy. *Applied Catalysis B: Environmental* **2019**, 117843.
178. Srikanth Kolagatla; Palaniappan Subramanian; Alex Schechter, Simultaneous Mapping of Oxygen Reduction Activity and Hydrogen Peroxide Generation on Electrocatalytic Surfaces. *ChemSus Chem* **2019**.
179. Julie V Macpherson; Claire E Jones; Anna L Barker; Patrick R Unwin, Electrochemical imaging of diffusion through single nanoscale pores. *Analytical Chemistry* **2002**, *74*, 1841-1848.
180. Claire E Jones; Patrick R Unwin; Julie V Macpherson, In situ observation of the surface processes involved in dissolution from the cleavage surface of calcite in aqueous solution using combined scanning electrochemical–atomic force microscopy (SECM-AFM). *ChemPhys Chem* **2003**, *4*, 139-146.
181. Ali Davoodi; Jinshan Pan; Christofer Leygraf; Stefan Norgren, Multianalytical and in situ studies of localized corrosion of EN AW-3003 alloy—influence of intermetallic particles. *Journal of The Electrochemical Society* **2008**, *155*, C138-C146.
182. J Izquierdo; A Eifert; RM Souto; C Kranz, Simultaneous pit generation and visualization of pit topography using combined atomic force–scanning electrochemical microscopy. *Electrochemistry Communications* **2015**, *51*, 15-18.
183. Javier Izquierdo; Alexander Eifert; Christine Kranz; Ricardo M Souto, In situ monitoring of pit nucleation and growth at an iron passive oxide layer by using combined atomic force and scanning electrochemical microscopy. *ChemElectro Chem* **2015**, *2*, 1847-1856.
184. J Izquierdo; BM Fernández-Pérez; A Eifert; RM Souto; C Kranz, Simultaneous atomic force—scanning electrochemical microscopy (afm-secm) imaging of copper dissolution. *Electrochimica Acta* **2016**, *201*, 320-332.
185. Javier Izquierdo; Alexander Eifert; Christine Kranz; Ricardo M Souto, In situ investigation of copper corrosion in acidic chloride solution using atomic force—scanning electrochemical microscopy. *Electrochimica Acta* **2017**, *247*, 588-599.
186. Kranz, Christine, Angelika Kueng, Alois Lugstein, Emmerich Bertagnolli, and Boris Mizaikoff Boris Mizaikoff, Mapping of enzyme activity by detection of

- enzymatic products during AFM imaging with integrated SECM–AFM probes. *Ultramicroscopy* **2004**, *100*, 127-134.
187. Yoshiki Hirata; Soichi Yabuki; Fumio Mizutani, Application of integrated SECM ultra-micro-electrode and AFM force probe to biosensor surfaces. *Bioelectrochemistry* **2004**, *63*, 217-224.
188. Angelika Kueng; Christine Kranz; Alois Lugstein; Emmerich Bertagnolli; Boris Mizaikoff, AFM-tip - integrated amperometric microbiosensors: high - resolution imaging of membrane transport. *Angewandte Chemie International Edition* **2005**, *44*, 3419-3422.
189. Agnes Anne; Arnaud Chovin; Christophe Demaille; Manon Lafouresse, High-Resolution mapping of redox-immunomarked proteins using electrochemical–atomic force microscopy in molecule touching mode. *Analytical Chemistry* **2011**, *83*, 7924-7932.
190. Laurent Nault; Cecilia Taofifenua; Agnes Anne; Arnaud Chovin; Christophe Demaille; Jane Besong-Ndika; Daniela Cardinale; Noëlle Carette; Thierry Michon; Jocelyne Walter, Electrochemical atomic force microscopy imaging of redox-immunomarked proteins on native potyviruses: from subparticle to single-protein resolution. *ACS Nano* **2015**, *9*, 4911-4924.
191. Agnès Anne; Arnaud Chovin; Christophe Demaille; Thierry Michon, Redox-immunofunctionalized potyvirus nanoparticles for high-resolution imaging by afm-secm correlative microscopy. *Virus-Derived Nanoparticles for Advanced Technologies*, **2018**; pp 455-470.
192. Kang Wang; Cédric Goyer; Agnès Anne; Christophe Demaille, Exploring the motional dynamics of end-grafted DNA oligonucleotides by in situ electrochemical atomic force microscopy. *The Journal of Physical Chemistry B* **2007**, *111*, 6051-6058.
193. Kristian Torbensen; Anisha Patel; Agnes Anne; Arnaud Chovin; Christophe Demaille; Laure Bataille; Thierry Michon; Eric Grelet, Immuno-Based Molecular Scaffolding of Glucose Dehydrogenase and Ferrocene Mediator on fd Viral Particles Yields Enhanced Bioelectrocatalysis. *ACS Catalysis* **2019**.
194. Patrick LTM Frederix; Patrick D Bosshart; Terunobu Akiyama; Mohamed Chami; Maurizio R Gullo; Jason J Blackstock; Karin Dooleweerd; Nico F de Rooij; Urs Staufer; Andreas Engel, Conductive supports for combined AFM–SECM on biological membranes. *Nanotechnology* **2008**, *19*, 384004.
195. Soichiro Sekine; Hirokazu Kaji; Matsuhiko Nishizawa, Integration of an electrochemical-based biolithography technique into an AFM system. *Analytical and Bioanalytical Chemistry* **2008**, *391*, 2711-2716.

196. Soichiro Sekine; Hirokazu Kaji; Matsuhiko Nishizawa, Spatiotemporal sub-cellular biopatterning using an AFM-assisted electrochemical system. *Electrochemistry Communications* **2009**, *11*, 1781-1784.
197. P Knittel; Hao Zhang; Christine Kranz; Gordon G Wallace; Michael J Higgins, Probing the PEDOT: PSS/cell interface with conductive colloidal probe AFM-SECM. *Nanoscale* **2016**, *8*, 4475-4481.
198. Rebecca L. Wolfe; Ramjee Balasubramanian; Joseph B. Tracy; Royce W. Murray, Fully ferrocenated hexanethiolate monolayer-protected gold clusters. *Langmuir* **2007**, *23*, 2247-2254.
199. Shuang-Yan Lang; Yang Shi; Yu-Guo Guo; Dong Wang; Rui Wen; Li-Jun Wan, Insight into the interfacial process and mechanism in lithium-sulfur batteries: an in situ AFM study. *Angewandte Chemie International Edition* **2016**, *55*, 15835-15839.
200. Ivan Khalakhan; Mykhailo Vorokhta; Peter Kúš; Milan Dopita; Michal Václavů; Roman Fiala; Nataliya Tsud; Tomáš Skála; Vladimír Matolín, In situ probing of magnetron sputtered Pt-Ni alloy fuel cell catalysts during accelerated durability test using EC-AFM. *Electrochimica Acta* **2017**, *245*, 760-769.
201. Giorgia Zampardi; Stefan Klink; Volodymyr Kuznetsov; Thomas Erichsen; Artjom Maljusch; Fabio La Mantia; Wolfgang Schuhmann; Edgar Ventosa, Combined AFM/SECM investigation of the solid electrolyte interphase in li - ion batteries. *ChemElectro Chem* **2015**, *2*, 1607-1611.
202. Can Liu; Shen Ye, In situ atomic force microscopy (afm) study of oxygen reduction reaction on a gold electrode surface in a dimethyl sulfoxide (dms)-based electrolyte solution. *The Journal of Physical Chemistry C* **2016**, *120*, 25246-25255.
203. Xin-Cheng Hu; Yang Shi; Shuang-Yan Lang; Xing Zhang; Lin Gu; Yu-Guo Guo; Rui Wen; Li-Jun Wan, Direct insights into the electrochemical processes at anode/electrolyte interfaces in magnesium-sulfur batteries. *Nano Energy* **2018**, *49*, 453-459.
204. David T Pierce; Allen J Bard, Scanning electrochemical microscopy. 23. Retention localization of artificially patterned and tissue-bound enzymes. *Analytical Chemistry* **1993**, *65*, 3598-3604.
205. Andreas Hengstenberg; Andrea Blöchl; Irmgard D Dietzel; Wolfgang Schuhmann, Spatially resolved detection of neurotransmitter secretion from individual cells by means of scanning electrochemical microscopy. *Angewandte Chemie International Edition* **2001**, *40*, 905-908.



206. Kamonnaree Chotinantakul; Wipa Suginta; Albert Schulte, Advanced amperometric respiration assay for antimicrobial susceptibility testing. *Analytical Chemistry* **2014**, *86*, 10315-10322.
207. Aihua Liu; Qiaolin Lang; Bo Liang; Jianguo Shi, Sensitive detection of maltose and glucose based on dual enzyme-displayed bacteria electrochemical biosensor. *Biosensors and Bioelectronics* **2017**, *87*, 25-30.
208. Edgar D Goluch, Microbial identification using electrochemical detection of metabolites. *Trends in Biotechnology* **2017**, *35*, 1125-1128.
209. Yoram Selzer; Daniel Mandler, Scanning Electrochemical Microscopy. Theory of the feedback mode for hemispherical ultramicroelectrodes: steady-state and transient behavior. *Analytical Chemistry* **2000**, *72*, 2383-2390.
210. Thomas Nann; Jürgen Heinze, Simulation in electrochemistry using the finite element method part 2: scanning electrochemical microscopy. *Electrochimica Acta* **2003**, *48*, 3975-3980.
211. Q. Fulian; A. C. Fisher; G. Denuault, Applications of the boundary element method in electrochemistry: scanning electrochemical microscopy. *The Journal of Physical Chemistry B* **1999**, *103*, 4387-4392.
212. Ahmed Khaled Abdella Ahmed; Xiaonan Shi; Likun Hua; Leidy Manzueta; Weihua Qing; Taha Marhaba; Wen Zhang, Influences of air, oxygen, nitrogen, and carbon dioxide nanobubbles on seed germination and plant growth. *Journal of Agricultural and Food Chemistry* **2018**, *66*, 5117-5124.
213. Liming Hu; Zhiran Xia, Application of ozone micro-nano-bubbles to groundwater remediation. *Journal of Hazardous Materials* **2018**, *342*, 446-453.
214. Yu Xiong; Felicia Peng, Optimization of cavitation venturi tube design for pico and nano bubbles generation. *International Journal of Mining Science and Technology* **2015**, *25*, 523-529.
215. Yasuhito Nakatake; Takashi Watanabe; Toshihiko Eguchi, Experimental investigation on diesel engine performance using nano air-bubbles mixed into gas oil. *Journal of Energy and Power Engineering* **2013**, *7*, 827.
216. Ahmed Khaled Abdella Ahmed; Cuizhen Sun; Likun Hua; Zhibin Zhang; Yanhao Zhang; Wen Zhang; Taha Marhaba, Generation of nanobubbles by ceramic membrane filters: The dependence of bubble size and zeta potential on surface coating, pore size and injected gas pressure. *Chemosphere* **2018**, *203*, 327-335.
217. Coey JMD; Matthias Möbius; Alice J Gillen; Siddhartha Sen, Generation and stability of freestanding aqueous microbubbles. *Electrochemistry Communications* **2017**, *76*, 38-41.

218. Jie Zhu; Hongjie An; Muidh Alheshibri; Lvdan Liu; Paul MJ Terpstra; Guangming Liu; Vincent SJ Craig, Cleaning with bulk nanobubbles. *Langmuir* **2016**, *32*, 11203-11211.
219. Fernanda Yumi Ushikubo; Takuro Furukawa; Ryou Nakagawa; Masatoshi Enari; Yoshio Makino; Yoshinori Kawagoe; Takeo Shiina; Seiichi Oshita, Evidence of the existence and the stability of nano-bubbles in water. *Colloids and Surfaces A: Physicochemical and Engineering Aspects* **2010**, *361*, 31-37.
220. Hengli Yang; Wenbin Cai; Lei Xu; Xiuhua Lv; Youbei Qiao; Pan Li; Hong Wu; Yilin Yang; Li Zhang; Yunyou Duan, Nanobubble–Affibody: Novel ultrasound contrast agents for targeted molecular ultrasound imaging of tumor. *Biomaterials* **2015**, *37*, 279-288.
221. A Sobhy; D Tao, Nanobubble column flotation of fine coal particles and associated fundamentals. *International Journal of Mineral Processing* **2013**, *124*, 109-116.
222. Owen C Thomas; Richard E Cavicchi; Michael J Tarlov, Effect of surface wettability on fast transient microboiling behavior. *Langmuir* **2003**, *19*, 6168-6177.
223. Marek Žbik; Roger G Horn, Hydrophobic attraction may contribute to aqueous flocculation of clays. *Colloids and Surfaces A: Physicochemical and Engineering Aspects* **2003**, *222*, 323-328.
224. Arizbeth Pérez; Tatyana Poznyak; Isaac Chairez, Microorganism inactivation by ozone dissolved in aqueous solution: a kinetic study based on bacterial culture lipid unsaturation. *Ozone: Science and Engineering* **2015**, *37*, 119-126.
225. Jishuai Bing; Chun Hu; Lili Zhang, Enhanced mineralization of pharmaceuticals by surface oxidation over mesoporous  $\gamma$ -Ti-Al<sub>2</sub>O<sub>3</sub> suspension with ozone. *Applied Catalysis B: Environmental* **2017**, *202*, 118-126.
226. Vithu Prabha; Rahul Deb Barma; Ranjit Singh; Aditya Madan, Ozone technology in food processing: a review. *Trends in Biosciences* **2015**, *8*, 4031-4047.
227. R Pandiselvam; S Sunoj; MR Manikantan; Anjineyulu Kothakota; KB Hebbar, Application and kinetics of ozone in food preservation. *Ozone: Science and Engineering* **2017**, *39*, 115-126.
228. Jerónimo Tessier; Patricia N Rodriguez; Fima Lifshitz; Silvia M Friedman; Eduardo J Lanata, The use of ozone to lighten teeth: an experimental study. *Acta Odontológica Latinoamericana* **2010**, *23*, 84-89.
229. Paolo Barone, Oxygen-ozone therapy in a multidisciplinary day surgery: Design and applications. *Ozone Therapy* **2017**, *2*.

230. Shiva RG Manjunath; Deepak Singla; Akanksha Singh, Ozone revisited. *Journal of Advanced Oral Research* **2015**, 6.
231. Tatek Temesgen; Thi Thuy Bui; Mooyoung Han; Tschung-il Kim; Hyunju Park, Micro and nanobubble technologies as a new horizon for water-treatment techniques: a review. *Advances in Colloid and Interface Science* **2017**.
232. Kuo-Kang Chen, Bathing pool assembly with water full of nano-scale ozone bubbles for rehabilitation. *Google Patents*: **2009**.
233. M. Sumikura; M. Hidaka; H. Murakami; Y. Nobutomo; T. Murakami, Ozone micro-bubble disinfection method for wastewater reuse system. *Water Science and Technology* **2007**, 56, 53-61.
234. L. Mezule; S. Tsyfansky; V. Yakushevich; T. Juhna, A simple technique for water disinfection with hydrodynamic cavitation: effect on survival of Escherichia coli. *Desalination* **2009**, 248, 152-159.
235. Yurika Ikeda-Dantsuji; Loreto B. Feril; Katsuro Tachibana; Koichi Ogawa; Hitomi Endo; Yoshimi Harada; Ryo Suzuki; Kazuo Maruyama, Synergistic effect of ultrasound and antibiotics against Chlamydia trachomatis-infected human epithelial cells in vitro. *Ultrasonics Sonochemistry* **2011**, 18, 425-430.
236. Tianlong Zheng; Tao Zhang; Qunhui Wang; Yanli Tian; Zhining Shi; Nicholas Smale; Banghua Xu, Advanced treatment of acrylic fiber manufacturing wastewater with a combined microbubble-ozonation/ultraviolet irradiation process. *RSC Advances* **2015**, 5, 77601-77609.
237. Karol Ulatowski; Paweł Sobieszuk; Andrzej Mróz; Tomasz Ciach, Stability of nanobubbles generated in water using porous membrane system. *Chemical Engineering and Processing-Process Intensification* **2019**, 136, 62-71.
238. Seung Hoon Oh; Jung Guen Han; Jong-Min Kim, Long-term stability of hydrogen nanobubble fuel. *Fuel* **2015**, 158, 399-404.
239. Antonin Marchand; Joost H Weijs; Jacco H Snoeijer; Bruno Andreotti, Why is surface tension a force parallel to the interface? *American Journal of Physics* **2011**, 79, 999-1008.
240. Stig Ljunggren; Jan Christer Eriksson, The lifetime of a colloid-sized gas bubble in water and the cause of the hydrophobic attraction. *Colloids and Surfaces A: Physicochemical and Engineering Aspects* **1997**, 129, 151-155.
241. Paul S Epstein; Milton S Plesset, On the stability of gas bubbles in liquid-gas solutions. *The Journal of Chemical Physics* **1950**, 18, 1505-1509.
242. Nikolai F Bunkin; Alexey V Shkirin; Nikolay V Suyazov; Vladimir A Babenko; Andrey A Sychev; Nikita V Penkov; Konstantin N Belosludtsev; Sergey V

- Gudkov, Formation and dynamics of ion-stabilized gas nanobubble phase in the bulk of aqueous NaCl solutions. *The Journal of Physical Chemistry B* **2016**, *120*, 1291-1303.
243. Jean-Louis Demangeat, Gas nanobubbles and aqueous nanostructures: the crucial role of dynamization. *Homeopathy* **2015**, *104*, 101-115.
244. Neelkanth Nirmalkar; AW Pacek; Mostafa Barigou, Bulk nanobubbles from acoustically cavitated aqueous organic solvent mixtures. *Langmuir* **2019**, *35*, 2188-2195.
245. Changsheng Chen; Jing Li; Xianren Zhang, The existence and stability of bulk nanobubbles: a long-standing dispute on the experimentally observed mesoscopic inhomogeneities in aqueous solutions. *Communications in Theoretical Physics* **2020**, *72*, 037601.
246. Seung Hoon Oh; Jong-Min Kim, Generation and stability of bulk nanobubbles. *Langmuir* **2017**, *33*, 3818-3823.
247. Jeremiah C Millare; Blessie A Basilia, Nanobubbles from ethanol - water mixtures: generation and solute effects via solvent replacement method. *Chemistry Select* **2018**, *3*, 9268-9275.
248. Andreas A Kalmes; Supurna Ghosh; Richard L Watson, A saline-based therapeutic containing charge-stabilized nanostructures protects against cardiac ischemia/reperfusion injury. *Journal of the American College of Cardiology* **2013**, *61*, E106.
249. Xi Zhang; Xinjuan Liu; Yuan Zhong; Zhaofeng Zhou; Yongli Huang; Chang Q Sun, Nanobubble skin supersolidity. *Langmuir* **2016**, *32*, 11321-11327.
250. Joost H Weijjs; James RT Seddon; Detlef Lohse, Diffusive shielding stabilizes bulk nanobubble clusters. *ChemPhys Chem* **2012**, *13*, 2197-2204.
251. Tsu-Wei Huang; Shih-Yi Liu; Yun-Ju Chuang; Hsin-Yi Hsieh; Chun-Ying Tsai; Wei-Jung Wu; Cheng-Ting Tsai; Utkur Mirsaidov; Paul Matsudaira; Chia-Shen Chang, Dynamics of hydrogen nanobubbles in KLH protein solution studied with in situ wet-TEM. *Soft Matter* **2013**, *9*, 8856-8861.
252. Meng Zhang; Yu-song Tu; Hai-ping Fang, Concentration of nitrogen molecules needed by nitrogen nanobubbles existing in bulk water. *Applied Mathematics and Mechanics* **2013**, *34*, 1433-1438.
253. Ahmed Khaled Abdella Ahmed; Cuizhen Sun; Likun Hua; Zhibin Zhang; Yanhao Zhang; Taha Marhaba; Wen Zhang, Colloidal properties of air, oxygen, and nitrogen nanobubbles in water: effects of ionic strength, natural organic matters, and surfactants. *Environmental Engineering Science* **2017**.

254. Ayanavilli Srinivas; Pallab Ghosh, Coalescence of bubbles in aqueous alcohol solutions. *Industrial and Engineering Chemistry Research* **2011**, *51*, 795-806.
255. Shuo Ke; Wei Xiao; Nannan Quan; Yaming Dong; Lijuan Zhang; Jun Hu, Formation and Stability of Bulk Nanobubbles in Different Solutions. *Langmuir* **2019**, *35*, 5250-5256.
256. Lei Wu; Zhichao Dong; Fengyu Li; Yanlin Song, Designing laplace pressure pattern for microdroplet manipulation. *Langmuir* **2018**, *34*, 639-645.
257. Kazunari Ohgaki; Nguyen Quoc Khanh; Yasuhiro Joden; Atsushi Tsuji; Takaharu Nakagawa, Physicochemical approach to nanobubble solutions. *Chemical Engineering Science* **2010**, *65*, 1296-1300.
258. Phil Attard, The stability of nanobubbles. *The European Physical Journal Special Topics* **2013**, 1-22.
259. Michael P Brenner; Detlef Lohse, Dynamic equilibrium mechanism for surface nanobubble stabilization. *Physical review letters* **2008**, *101*, 214505.
260. Limin Zhou; Xingya Wang; Hyun-Joon Shin; Jian Wang; Renzhong Tai; Xuehua Zhang; Haiping Fang; Wei Xiao; Lei Wang; Chunlei Wang, Ultra-high density of gas molecules confined in surface nanobubbles in ambient water. *Journal of the American Chemical Society* **2020**.
261. Shuo Wang; Limin Zhou; Xingya Wang; Chunlei Wang; Yaming Dong; Yi Zhang; Yongxiang Gao; Lijuan Zhang; Jun Hu, Force spectroscopy revealed a high-gas-density state near the graphite substrate inside surface nanobubbles. *Langmuir* **2019**, *35*, 2498-2505.
262. Shuo Wang; Minghuan Liu; Yaming Dong, Understanding the stability of surface nanobubbles. *Journal of Physics: Condensed Matter* **2013**, *25*, 184007.
263. Qiaozhi Wang; Hui Zhao; Na Qi; Yan Qin; Xuejie Zhang; Ying Li, Generation and stability of size-adjustable bulk nanobubbles based on periodic pressure change. *Scientific Reports* **2019**, *9*, 1118.
264. Dongha Shin; Jong Bo Park; Yong-Jin Kim; Sang Jin Kim; Jin Hyoun Kang; Bora Lee; Sung-Pyo Cho; Byung Hee Hong; Konstantin S Novoselov, Growth dynamics and gas transport mechanism of nanobubbles in graphene liquid cells. *Nature Communications* **2015**, *6*, 6068.
265. Jong Bo Park; Dongha Shin; Sangmin Kang; Sung-Pyo Cho; Byung Hee Hong, Distortion in two-dimensional shapes of merging nanobubbles: Evidence for anisotropic gas flow mechanism. *Langmuir* **2016**, *32*, 11303-11308.

266. Shangjiong Yang; Stephan M Dammer; Nicolas Bremond; Harold JW Zandvliet; E Stefan Kooij; Detlef Lohse, Characterization of nanobubbles on hydrophobic surfaces in water. *Langmuir* **2007**, *23*, 7072-7077.
267. Nicole Hain; Daniel Wesner; Sergey I Druzhinin; Holger Schönherr, Surface nanobubbles studied by time-resolved fluorescence microscopy methods combined with AFM: the impact of surface treatment on nanobubble nucleation. *Langmuir* **2016**, *32*, 11155-11163.
268. Marziyeh Jannesari; Omid Akhavan; Hamid R Madaah Hosseini, Graphene oxide in generation of nanobubbles using controllable microvortices of jet flows. *Carbon* **2018**.
269. Qianjin Chen; Long Luo; Hamaseh Faraji; Stephen W Feldberg; Henry S White, Electrochemical measurements of single H<sub>2</sub> nanobubble nucleation and stability at Pt nanoelectrodes. *The Journal of Physical Chemistry Letters* **2014**, *5*, 3539-3544.
270. Stephanie B Velegol; Bruce E Logan, Contributions of bacterial surface polymers, electrostatics, and cell elasticity to the shape of AFM force curves. *Langmuir* **2002**, *18*, 5256-5262.
271. Anna Mularski; Jonathan J Wilksch; Huabin Wang; Mohammed Akhter Hossain; John D Wade; Frances Separovic; Richard A Strugnell; Michelle L Gee, Atomic force microscopy reveals the mechanobiology of lytic peptide action on bacteria. *Langmuir* **2015**, *31*, 6164-6171.
272. Binyu Zhao; Xingya Wang; Shuo Wang; Renzhong Tai; Lijuan Zhang; Jun Hu, In situ measurement of contact angles and surface tensions of interfacial nanobubbles in ethanol aqueous solutions. *Soft Matter* **2016**, *12*, 3303-3309.
273. Hongjie An; Beng Hau Tan; Claus-Dieter Ohl, Distinguishing nanobubbles from nanodroplets with AFM: the influence of vertical and lateral imaging forces. *Langmuir* **2016**, *32*, 12710-12715.
274. Kutzner B; Van der Spoel D; Lindahl E, Gromacs : Algorithms for highly efficient, load-balanced, and scalable molecular simulation hess. *Journal of Chem Theory Comput* **2008**, *4*, 435-447.
275. Ahmed Khaled Abdella Ahmed; Cuizhen Sun; Likun Hua; Zhibin Zhang; Yanhao Zhang; Taha Marhaba; Wen Zhang, Colloidal properties of air, oxygen, and nitrogen nanobubbles in water: effects of ionic strength, natural organic matters, and surfactants. *Environmental Engineering Science* **2018**, *35*, 720-727.
276. Ahmed Khaled Abdella Ahmed; Cuizhen Sun; Likun Hua; Zhibin Zhang; Yanhao Zhang; Wen Zhang; Taha Marhaba, Generation of nanobubbles by ceramic membrane filters: The dependence of bubble size and zeta potential on surface coating, pore size and injected gas pressure. *Chemosphere* **2018**.

277. Hans-Jürgen Butt; Karlheinz Graf; Michael Kappl, *Physics and chemistry of interfaces*. Weinheim, Germany, John Wiley & Sons: **2006**.
278. Hsien-Shun Liao; Chih-Wen Yang; Hsien-Chen Ko; En-Te Hwu; Shouh Hwang, Imaging initial formation processes of nanobubbles at the graphite–water interface through high-speed atomic force microscopy. *Applied Surface Science* **2018**, *434*, 913-917.
279. Wiktoria Walczyk; Peter M Schön; Holger Schönherr, The effect of PeakForce tapping mode AFM imaging on the apparent shape of surface nanobubbles. *Journal of Physics: Condensed Matter* **2013**, *25*, 184005.
280. Kuo-Kang Liu, Deformation behaviour of soft particles: a review. *Journal of Physics D: Applied Physics* **2006**, *39*, R189.
281. Yeh-Shiu Chu; Sylvie Dufour; Jean Paul Thiery; Eric Perez; Frederic Pincet, Johnson-Kendall-Roberts theory applied to living cells. *Physical Review Letters* **2005**, *94*, 028102.
282. Korayem MH; Rastegar Z; Taheri M, Sensitivity analysis of nano-contact mechanics models in manipulation of biological cell. *Nanoscience and Nanotechnology* **2012**, *2*, 49-56.
283. Korayem MH; Taheri M, Modeling of various contact theories for the manipulation of different biological micro/nanoparticles based on AFM. *Journal of Nanoparticle Research* **2014**, *16*, 2156.
284. Wen Zhang; Andrew G Stack; Yongsheng Chen, Interaction force measurement between E. coli cells and nanoparticles immobilized surfaces by using AFM. *Colloids and Surfaces B: Biointerfaces* **2011**, *82*, 316-324.
285. Raimondas Jasevičius; Romas Baronas; Harald Kruggel-Emden, Numerical modelling of the normal adhesive elastic–plastic interaction of a bacterium. *Advanced Powder Technology* **2015**, *26*, 742-752.
286. Touhami A; Othmane A; Ouerghi O; Ben Ouada H; Fretigny C; Jaffrezic-Renault N, Red blood cells imaging and antigen–antibody interaction measurement. *Biomolecular Engineering* **2002**, *19*, 189-193.
287. Fabien Gaboriaud; Yves F. Dufrene, Atomic force microscopy of microbial cells: Application to nanomechanical properties, surface forces and molecular recognition forces. *Colloids Surface B: Biointerfaces* **2007**, *54*, 10-19.
288. Muidh Alheshibri; Vincent SJ Craig, Generation of nanoparticles upon mixing ethanol and water; nanobubbles or not? *Journal of Colloid and Interface Science* **2019**, *542*, 136-143.

289. Ian D Wilson, *Encyclopedia of separation science*. San Diego, CA, Academic Press: **2000**.
290. Ponisseril Somasundaran, *Encyclopedia of surface and colloid science*. Boca Raton, FL, CRC press: **2006**.
291. Jiaqi Jin; Liem X Dang; Jan D Miller, Molecular dynamics simulations study of nano bubble attachment at hydrophobic surfaces. *Physicochemical Problems of Mineral Processing* **2018**, 54.
292. YouQuan Jia; BinYu Zhao; Abbasali Abouei Mehrizi; Chuan Wang; Yi Xu; LongQuan Chen, Identification of surface nanobubbles and resolving their size-dependent stiffness. *Science China Physics, Mechanics and Astronomy* **2020**, 63, 1-11.
293. A Azevedo; R Etchepare; S Calgaroto; J Rubio, Aqueous dispersions of nanobubbles: Generation, properties and features. *Minerals Engineering* **2016**, 94, 29-37.
294. Behzad Vaziri Hassas; Jiaqi Jin; Liem X Dang; Xuming Wang; Jan D Miller, Attachment, coalescence, and spreading of carbon dioxide nanobubbles at pyrite surfaces. *Langmuir* **2018**, 34, 14317-14327.
295. Xuming Wang; Xihui Yin; Jakub Nalaskowski; Hao Du; Jan D Miller, Molecular features of water films created with bubbles at silica surfaces. *Surface Innovations* **2015**, 3, 20-26.
296. Henri Lhuissier; Detlef Lohse; Xuehua Zhang, Spatial organization of surface nanobubbles and its implications in their formation process. *Soft Matter* **2014**, 10, 942-946.
297. Hideaki Teshima; Koji Takahashi; Yasuyuki Takata; Takashi Nishiyama, Wettability of AFM tip influences the profile of interfacial nanobubbles. *Journal of Applied Physics* **2018**, 123, 054303.
298. Wen Zhang; Ying Yao; Yongsheng Chen, Imaging and quantifying the morphology and nanoelectrical properties of quantum dot nanoparticles interacting with DNA. *The Journal of Physical Chemistry C* **2011**, 115, 599-606.
299. F Gołek; P Mazur; Z Ryszka; S Zuber, AFM image artifacts. *Applied Surface Science* **2014**, 304, 11-19.
300. James RT Seddon; Detlef Lohse; William A Ducker; Vincent SJ Craig, A deliberation on nanobubbles at surfaces and in bulk. *ChemPhys Chem* **2012**, 13, 2179-2187.



301. James RT Seddon; Detlef Lohse, Nanobubbles and micropancakes: gaseous domains on immersed substrates. *Journal of Physics: Condensed Matter* **2011**, *23*, 133001.
302. Vincent SJ Craig, Surface nanobubbles or knudsen bubbles? *Physics* **2011**, *4*, 70.
303. Xue Hua Zhang; Anthony Quinn; William A Ducker, Nanobubbles at the interface between water and a hydrophobic solid. *Langmuir* **2008**, *24*, 4756-4764.
304. Binyu Zhao; Yang Song; Shuo Wang; Bin Dai; Lijuan Zhang; Yaming Dong; Junhong Lü; Jun Hu, Mechanical mapping of nanobubbles by PeakForce atomic force microscopy. *Soft Matter* **2013**, *9*, 8837-8843.
305. Limin Zhou; Xingya Wang; Hyun-Joon Shin; Jian Wang; Renzhong Tai; Xuehua Zhang; Haiping Fang; Wei Xiao; Lei Wang; Chunlei Wang, Ultrahigh density of gas molecules confined in surface nanobubbles in ambient water. *Journal of the American Chemical Society* **2020**, *142*, 5583-5593.
306. Arsam Behkish; Romain Lemoine; Laurent Sehabiague; Rachid Oukaci; Badie I Morsi, Gas holdup and bubble size behavior in a large-scale slurry bubble column reactor operating with an organic liquid under elevated pressures and temperatures. *Chemical Engineering Journal* **2007**, *128*, 69-84.
307. Yanan Liu; Han Zhang; Jihui Sun; Jinxia Liu; Xue Shen; Jiaxun Zhan; Ai Zhang; Stéphanie Ognier; Simeon Cavadías; Pan Li, Degradation of aniline in aqueous solution using non-thermal plasma generated in microbubbles. *Chemical Engineering Journal* **2018**, *345*, 679-687.
308. Robin P Berkelaar; James RT Seddon; Harold JW Zandvliet; Detlef Lohse, Temperature dependence of surface nanobubbles. *ChemPhys Chem* **2012**, *13*, 2213-2217.
309. Xiaonan Shi; Weihua Qing; Taha Marhaba; Wen Zhang, Atomic force microscopy-scanning electrochemical microscopy (afm-secm) for nanoscale topographical and electrochemical characterization: principles, applications and perspectives. *Electrochimica Acta* **2019**, 135472.
310. Elham S Aazam; Mohamed M Ghoneim; Mona A El-Attar, Synthesis, characterization, electrochemical behavior, and biological activity of bisazomethine dye derived from 2, 3-diaminomaleonitrile and 2-hydroxy-1-naphthaldehyde and its zinc complex. *Journal of Coordination Chemistry* **2011**, *64*, 2506-2520.
311. Shukla AK; Sampath S; Vijayamohanan K, Electrochemical supercapacitors: Energy storage beyond batteries. *Current Science* **2000**, *79*, 1656-1661.
312. Kötz R; Carlen M, Principles and applications of electrochemical capacitors. *Electrochimica Acta* **2000**, *45*, 2483-2498.

313. Gerardine G Botte, Electrochemical manufacturing in the chemical industry. *The Electrochemical Society Interface* **2014**, *23*, 49-55.
314. N Kongsricharoern; C Polprasert, Electrochemical precipitation of chromium (Cr<sup>6+</sup>) from an electroplating wastewater. *Water Science and Technology* **1995**, *31*, 109-117.
315. M Datta; D Landolt, Fundamental aspects and applications of electrochemical microfabrication. *Electrochimica Acta* **2000**, *45*, 2535-2558.
316. Shihuai Wang; Keith George; Srdjan Nesic, High pressure CO<sub>2</sub> corrosion electrochemistry and the effect of acetic acid. *Corrosion* **2004**, 4375.
317. G-L Song, Corrosion electrochemistry of magnesium (Mg) and its alloys. *Corrosion of Magnesium Alloys*, 2011; pp 3-65.
318. Z. H. Cui; X. X. Guo; H. Li, Equilibrium voltage and overpotential variation of nonaqueous Li–O<sub>2</sub> batteries using the galvanostatic intermittent titration technique. *Energy and Environmental Science* **2015**, *8*, 182-187.
319. Anisha N Patel; Christine Kranz, (Multi) functional atomic force microscopy imaging. *Annual Review of Analytical Chemistry* **2018**, *11*, 329-350.
320. Joachim Ufheil; Christian Heß; Kai Borgwarth; Jürgen Heinze, Nanostructuring and nanoanalysis by scanning electrochemical microscopy (SECM). *Physical Chemistry Chemical Physics* **2005**, *7*, 3185-3190.
321. Stefan Bergner; Joachim Wegener; Frank-Michael Matysik, Simultaneous imaging and chemical attack of a single living cell within a confluent cell monolayer by means of scanning electrochemical microscopy. *Analytical Chemistry* **2011**, *83*, 169-174.
322. Keke Hu; Yang Gao; Yixian Wang; Yun Yu; Xin Zhao; Susan A Rotenberg; Ebru Gökmeşe; Michael V Mirkin; Gary Friedman; Yury Gogotsi, Platinized carbon nanoelectrodes as potentiometric and amperometric SECM probes. *Journal of Solid State Electrochemistry* **2013**, *17*, 2971-2977.
323. Christine Kranz, Recent advancements in nanoelectrodes and nanopipettes used in combined scanning electrochemical microscopy techniques. *Analyst* **2014**, *139*, 336-352.
324. Julie V Macpherson; Patrick R Unwin; Andrew C Hillier; Allen J Bard, In-situ imaging of ionic crystal dissolution using an integrated electrochemical/AFM probe. *Journal of the American Chemical Society* **1996**, *118*, 6445-6452.
325. Tsutomu Uchida; Seiichi Oshita; Masayuki Ohmori; Takuo Tsuno; Koichi Soejima; Satoshi Shinozaki; Yasuhisa Take; Koichi Mitsuda, Transmission

- electron microscopic observations of nanobubbles and their capture of impurities in wastewater. *Nanoscale Research Letters* **2011**, *6*, 1.
326. S Oshita; S Liu In Nanobubbles characteristics and its application to agriculture and foods, *International Symposium on Agri-Foods for Health and Wealth*, 2013; pp 5-8.
327. C Gabrielli; F Huet; M Keddad; P Rousseau; V Vivier, Scanning electrochemical microscopy for investigating gas bubble/liquid interfaces. *Electrochemical and Solid-State Letters* **2003**, *6*, E23-E26.
328. Noémie Elgrishi; Kelley J Rountree; Brian D McCarthy; Eric S Rountree; Thomas T Eisenhart; Jillian L Dempsey, A practical beginner's guide to cyclic voltammetry. *Journal of Chemical Education* **2017**, *95*, 197-206.
329. Jesús F Arteaga; Mercedes Ruiz-Montoya; Alberto Palma; Gema Alonso-Garrido; Sara Pintado; José M Rodríguez-Mellado, Comparison of the simple cyclic voltammetry (CV) and DPPH assays for the determination of antioxidant capacity of active principles. *Molecules* **2012**, *17*, 5126-5138.
330. Tsutomu Tasaki; Tsubasa Wada; Yoshinari Baba; Masato Kukizaki, Degradation of surfactants by an integrated nanobubbles/VUV irradiation technique. *Industrial and Engineering Chemistry Research* **2009**, *48*, 4237-4244.
331. Thomas J Roussel; Douglas J Jackson; Richard P Baldwin; Robert S Keynton, Amperometric techniques. *Encyclopedia of Microfluidics and Nanofluidics* **2015**, 55-64.
332. Dong-wei Yang; Qing-yuan Li; Feng-xia Shen; Qin Wang; Lu Li; Ning Song; Yong-nian Dai; Jin Shi, Electrochemical impedance studies of CO<sub>2</sub> reduction in ionic liquid/organic solvent electrolyte on Au electrode. *Electrochimica Acta* **2016**, *189*, 32-37.
333. V Lates; A Falch; A Jordaan; R Peach; RJ Kriek, An electrochemical study of carbon dioxide electroreduction on gold-based nanoparticle catalysts. *Electrochimica Acta* **2014**, *128*, 75-84.
334. Huiling Liu; Jinglong Han; Jili Yuan; Chengbin Liu; Dong Wang; Tian Liu; Meijun Liu; Jinming Luo; Aijie Wang; John C Crittenden, Deep dehalogenation of florfenicol using crystalline cop nanosheet arrays on a ti plate via direct cathodic reduction and atomic. *Environmental Science and Technology* **2019**, *53*, 11932-11940.
335. Shi-Tao Lou; Zhen-Qian Ouyang; Yi Zhang; Xiao-Jun Li; Jun Hu; Min-Qian Li; Fu-Jia Yang, Nanobubbles on solid surface imaged by atomic force microscopy. *Journal of Vacuum Science and Technology B: Microelectronics and Nanometer Structures Processing, Measurement, and Phenomena* **2000**, *18*, 2573-2575.

336. Bram M Borkent; Stephan M Dammer; Holger Schönherr; G Julius Vancso; Detlef Lohse, Superstability of surface nanobubbles. *Physical Review Letters* **2007**, *98*, 204502.
337. Majid Khayatnezhad; Roza Gholamin; SH Jamaatie-Somarin; R Zabihi-Mahmoodabad, Effects of peg stress on corn cultivars (*Zea mays* L.) at germination stage. *World Applied Science J* **2010**, *11*, 504-506.
338. Maarten Koornneef; Leónie Bentsink; Henk Hilhorst, Seed dormancy and germination. *Current Opinion in Plant Biology* **2002**, *5*, 33-36.
339. H. Ikeura; H. Takahashi; F. Kobayashi; M. Sato; M. Tamaki, Effects of microbubble generation methods and dissolved oxygen concentrations on growth of Japanese mustard spinach in hydroponic culture. *The Journal of Horticultural Science and Biotechnology* **2017**, 1-8.
340. Sarah P Yang; Ofek Bar-Ilan; Richard E Peterson; Warren Heideman; Robert J Hamers; Joel A Pedersen, Influence of humic acid on titanium dioxide nanoparticle toxicity to developing zebrafish. *Environmental Science and Technology* **2013**, *47*, 4718-4725.
341. Ken-ichi Ishibashi; Akira Fujishima; Toshiya Watanabe; Kazuhito Hashimoto, Detection of active oxidative species in TiO<sub>2</sub> photocatalysis using the fluorescence technique. *Electrochemistry Communications* **2000**, *2*, 207-210.
342. Qi Xiao; Zhichun Si; Jiang Zhang; Chong Xiao; Xiaoke Tan, Photoinduced hydroxyl radical and photocatalytic activity of samarium-doped TiO<sub>2</sub> nanocrystalline. *Journal of Hazardous Materials* **2008**, *150*, 62-67.
343. Jiali Tan; Congying Wang; Bin Xiang; Ruihong Han; Zhenfei Guo, Hydrogen peroxide and nitric oxide mediated cold-and dehydration-induced myo-inositol phosphate synthase that confers multiple resistances to abiotic stresses. *Plant, Cell and Environment* **2013**, *36*, 288-299.
344. Roman Gangl; Raimund Tenhaken, Raffinose family oligosaccharides act as galactose stores in seeds and are required for rapid germination of arabidopsis in the dark. *Frontiers in Plant Science* **2016**, *7*.
345. Nanae Masuda; Aya Maruyama; Toshihiko Eguchi; Tsutomu Hirakawa; Yoshinori Murakami, Influence of microbubbles on free radical generation by ultrasound in aqueous solution: dependence of ultrasound frequency. *The Journal of Physical Chemistry B* **2015**, *119*, 12887-12893.
346. Robert B Hamanaka; Navdeep S Chandel, Mitochondrial reactive oxygen species regulate cellular signaling and dictate biological outcomes. *Trends in Biochemical Sciences* **2010**, *35*, 505-513.

347. Dunyaporn Trachootham; Weiqin Lu; Marcia A Ogasawara; Nilsa Rivera-Del Valle; Peng Huang, Redox regulation of cell survival. *Antioxidants & Redox Signaling* **2008**, *10*, 1343-1374.
348. Edward Owusu-Ansah; Utpal Banerjee, Reactive oxygen species prime *Drosophila* haematopoietic progenitors for differentiation. *Nature* **2009**, *461*, 537-541.
349. Edward Owusu-Ansah; Amir Yavari; Sudip Mandal; Utpal Banerjee, Distinct mitochondrial retrograde signals control the G1-S cell cycle checkpoint. *Nature Genetics* **2008**, *40*, 356-361.
350. Christophe Bailly; Hayat El-Maarouf-Bouteau; Françoise Corbineau, From intracellular signaling networks to cell death: the dual role of reactive oxygen species in seed physiology. *Comptes Rendus Biologies* **2008**, *331*, 806-814.
351. Katharine Brieger; Stefania Schiavone; Francis J Miller Jr; Karl-Heinz Krause, Reactive oxygen species: from health to disease. *Swiss Medical Weekly* **2012**, *142*, w13659.
352. Toren Finkel, Signal transduction by reactive oxygen species. *The Journal of Cell Biology* **2011**, *194*, 7-15.
353. Silvia Tavarini; Cristina Sgherri; Anna Maria Ranieri; Luciana G. Angelini, Effect of nitrogen fertilization and harvest time on steviol glycosides, flavonoid composition, and antioxidant properties in stevia rebaudiana bertonii. *Journal of Agricultural and Food Chemistry* **2015**, *63*, 7041-7050.
354. Camille Bénard; Hélène Gautier; Frédéric Bourgaud; Dominique Grasselly; Brigitte Navez; Catherine Caris-Veyrat; Marie Weiss; Michel Génard, Effects of low nitrogen supply on tomato (*solanum lycopersicum*) fruit yield and quality with special emphasis on sugars, acids, ascorbate, carotenoids, and phenolic compounds. *Journal of Agricultural and Food Chemistry* **2009**, *57*, 4112-4123.
355. M. Ângelo Rodrigues; Laurindo Chambula Ladeira; Margarida Arrobas, Azotobacter-enriched organic manures to increase nitrogen fixation and crop productivity. *European Journal of Agronomy* **2018**, *93*, 88-94.
356. John L Havlin; James D Beaton; Samuel L Tisdale; Werner L Nelson, Soil fertility and fertilizers: an introduction to nutrient management. *Pearson Prentice Hall Upper Saddle River* 2005; Vol. 515.
357. Petra Marschner; Zed Rengel, Nutrient availability in soils. *Marschner's Mineral Nutrition of Higher Plants*: 2012; pp 315-330.
358. Zaigham Shahzad; Matthieu Canut; Colette Tournaire-Roux; Alexandre Martinière; Yann Boursiac; Olivier Loudet; Christophe Maurel, A potassium-

- dependent oxygen sensing pathway regulates plant root hydraulics. *Cell* **2016**, *167*, 87-98. e14.
359. Sal J Locascio, The Fertile Triangle. The interrelationship of air, water, and nutrients in maximizing soil productivity. *Hort Technology* **2000**, *10*, 232-232.
360. Y Shimada; M Yamaura; C Yamanaka, Long gap discharge guiding experiments using strongly and weakly ionized plasma channels for laser triggered lightning. *Plasma Science and Technology* **2007**, *9*, 740.
361. Neelkanth Nirmalkar; AW Pacek; Mostafa Barigou, On the existence and stability of bulk nanobubbles. *Langmuir* **2018**, *34*, 10964-10973.